Benchmarking Unsupervised Object Representations for Video Sequences

Marissa A. Weis[1,4]   MARISSA.WEIS@UNI-GOETTINGEN.DE

Kashyap Chitta[3,6]   KASHYAP.CHITTA@TUE.MPG.DE

Yash Sharma[4]   YASH.SHARMA@UNI-TUEBINGEN.DE

Wieland Brendel[4,5]   WIELAND.BRENDEL@UNI-TUEBINGEN.DE

Matthias Bethge[4,5]   MATTHIAS.BETHGE@UNI-TUEBINGEN.DE

Andreas Geiger[3,6]   A.GEIGER@UNI-TUEBINGEN.DE

Alexander S. Ecker[1,2,7]   ECKER@CS.UNI-GOETTINGEN.DE

[1]*Institute of Computer Science, University of Göttingen, Germany*
[2]*Campus Institute Data Science, Göttingen, Germany*
[3]*Department of Computer Science, University of Tübingen, Germany*
[4]*Institute for Theoretical Physics, University of Tübingen, Germany*
[5]*Bernstein Center for Computational Neuroscience, Tübingen, Germany*
[6]*Max Planck Institute for Intelligent Systems, Tübingen, Germany*
[7]*Max Planck Institute for Dynamics and Self-Organization, Göttingen, Germany*

Abstract

Perceiving the world in terms of objects and tracking them through time is a crucial prerequisite for reasoning and scene understanding. Recently, several methods have been proposed for unsupervised learning of object-centric representations. However, since these models were evaluated on different downstream tasks, it remains unclear how they compare in terms of basic perceptual abilities such as detection, figure-ground segmentation and tracking of objects. To close this gap, we design a benchmark with four data sets of varying complexity and seven additional test sets featuring challenging tracking scenarios relevant for natural videos. Using this benchmark, we compare the perceptual abilities of four object-centric approaches: ViMON, a video-extension of MONet, based on recurrent spatial attention, OP3, which exploits clustering via spatial mixture models, as well as TBA and SCALOR, which use explicit factorization via spatial transformers. Our results suggest that the architectures with unconstrained latent representations learn more powerful representations in terms of object detection, segmentation and tracking than the spatial transformer based architectures. We also observe that none of the methods are able to gracefully handle the most challenging tracking scenarios despite their synthetic nature, suggesting that our benchmark may provide fruitful guidance towards learning more robust object-centric video representations.

Keywords: Unsupervised learning, object-centric representations, benchmark, tracking, segmentation

1. Introduction

Humans understand the world in terms of objects (Marr, 1982; Spelke and Kinzler, 2007; Johnson, 2018). Being able to decompose our environment into independent objects that can interact with each other is an important prerequisite for reasoning and scene understanding (Spelke, 1988). Similarly, an artificial intelligence system would benefit from the ability to represent visual scenes in a structured way (Ullman et al., 2017; Lake et al., 2017; Greff et al., 2020) by both extracting objects and their interactions from video streams, and keeping track of them over time.

Recently, there has been an increased interest in *unsupervised* learning of *object-centric representations*. The key insight of these methods is that the compositionality of visual scenes can be used to both discover (Eslami et al., 2016; Greff et al., 2019; Burgess et al., 2019) and track objects in videos (Greff et al., 2017; van Steenkiste et al., 2018; Veerapaneni et al., 2020) without supervision. However, it is currently not well understood how the learned visual representations of different models compare to each other quantitatively, since the models have been developed with different downstream tasks in mind and have not been evaluated using a common protocol. Hence, in this work, we propose a benchmark based on procedurally generated video sequences to test basic perceptual abilities of object-centric video models under various challenging tracking scenarios.

An unsupervised object-based video representation should *(1)* effectively identify objects as they enter a scene, *(2)* accurately segment objects, as well as *(3)* maintain a consistent representation for each individual object in a scene over time. These perceptual abilities can be evaluated quantitatively in the established *multi-object tracking* framework (Bernardin and Stiefelhagen, 2008; Milan et al., 2016). We propose to utilize this protocol for analyzing the strengths and weaknesses of different object-centric representation learning methods, independent of any specific downstream task, in order to uncover the different inductive biases hidden in their choice of architecture and loss formulation. We therefore compiled a benchmark consisting of four procedurally generated video data sets of varying levels of visual complexity and two generalization tests. Using this benchmark, we quantitatively compared three classes of object-centric models, leading to the following insights:

- All of the models have shortcomings handling occlusion, albeit to different extents.
- OP3 (Veerapaneni et al., 2020) performs strongest in terms of quantitative metrics, but exhibits a surprisingly strong dependency on color to separate objects and accumulates false positives when fewer objects than slots are present.
- Spatial transformer models, TBA (He et al., 2019) and SCALOR (Jiang et al., 2020), train most efficiently and feature explicit depth reasoning in combination with amodal masks, but are nevertheless outperformed by the simpler model, ViMON, lacking a depth or interaction model, suggesting that the proposed mechanisms may not yet work as intended.

Our code, data, as well as a public leaderboard of results is available at `https://eckerlab.org/code/weis2021/`.

2. Related work

Several recent lines of work propose to learn object-centric representations from visual inputs for static and dynamic scenes without explicit supervision. Though their results are promising, methods are currently restricted to handling synthetic data sets and as of yet are unable to scale to complex natural scenes. Furthermore, a systematic quantitative comparison of methods is lacking.

Selecting and processing parts of an image via *spatial attention* has been one prominent approach for this task (Mnih et al., 2014; Eslami et al., 2016; Kosiorek et al., 2018; Burgess et al., 2019; Yuan et al., 2019; Crawford and Pineau, 2019). As an alternative, *spatial mixture* models decompose scenes by performing image-space clustering of pixels that belong to individual objects (Greff et al., 2016, 2017, 2019; van Steenkiste et al., 2018; Locatello et al., 2020). Xu et al. (2019) use optic flow to learn to segment objects or object parts in dynamic scenes. While some approaches aim at learning a suitable representation for downstream tasks (Watters et al., 2019a; Veerapaneni et al., 2020), others target scene generation (Engelcke et al., 2020; Kügelgen et al., 2020; Ehrhardt et al., 2020; Jiang and Ahn, 2020). We analyze three classes of models for processing videos, covering three models based on spatial attention and one based on spatial mixture modeling.

Spatial attention models with unconstrained latent representations use per-object variational autoencoders, as introduced by Burgess et al. (2019). Kügelgen et al. (2020) adapt this approach for scene generation. So far, such methods have been designed for static images, but not for videos. We therefore extend MONet (Burgess et al., 2019) to be able to accumulate evidence over time for tracking, enabling us to include this class of approaches in our evaluation. Recent concurrent work on AlignNet (Creswell et al., 2020) applies MONet frame-by-frame and tracks objects by subsequently ordering the extracted objects consistently.

Spatial attention models with factored latents use an explicit factorization of the latent representation into properties such as position, scale and appearance (Eslami et al., 2016; Crawford and Pineau, 2019). These methods use spatial transformer networks (Jaderberg et al., 2015) to render per-object reconstructions from the factored latents (Kosiorek et al., 2018; He et al., 2019; Jiang et al., 2020). SQAIR (Kosiorek et al., 2018) does not perform segmentation, identifying objects only at the bounding-box level. Henderson and Lampert (2020) explicitly reason about the underlying 3D scene structure. We select Tracking-by-Animation (TBA) (He et al., 2019) and SCALOR (Jiang et al., 2020) for analyzing spatial transformer methods in our experiments, which explicitly disentangle object shape and appearance, providing access to object masks.

Spatial mixture models cluster pixels using a deep neural network trained with expectation maximization (Greff et al., 2017; van Steenkiste et al., 2018). IODINE (Greff et al., 2019) extends these methods with an iterative amortised variational inference procedure (Marino et al., 2018), improving segmentation quality. SPACE (Lin et al., 2020) combines mixture models with spatial attention to improve scalability. To work with video sequences, OP3 (Veerapaneni et al., 2020) extends IODINE by modeling individual objects' dynamics as well as pairwise interactions. We therefore include OP3 in our analysis as a representative spatial mixture model.

	Objects						Background	
Data Set	Shape	Motion	Count Over Sequence	Size Variation	Orientation	Color	Motion	Color
SpMOT	4 Templates (2D)	Linear	Varies (0-3)	Minimal	Fixed	6 Colors	None	Black
VOR	2 Templates (3D)	Static	Varies (0-4)	Moderate	Random	6 Colors	Moving Camera	Random
VMDS	3 Templates (2D)	Non-Linear	Fixed (1-4)	Moderate	Random	256^3 Colors	None	256^3 Colors
texVMDS	3 Templates (2D)	Non-Linear	Fixed (1-4)	Moderate	Random	ImageNet textures	Linear	ImageNet crop

Table 1: Summary of data sets and example video sequences. See Appendix B for details.

3. Object-Centric Representation Benchmark

To compare the different object-centric representation learning models on their basic perceptual abilities, we use the well-established multi-object tracking (MOT) protocol (Bernardin and Stiefelhagen, 2008). In this section, we describe the data sets and metrics considered in our benchmark, followed by a brief description of the models evaluated.

3.1 Data Sets

Current object-centric models are not capable of modeling complex natural scenes (Burgess et al., 2019; Greff et al., 2019; Lin et al., 2020). Hence, we focus on synthetic data sets that resemble those which state-of-the-art models were designed for. Specifically, we evaluate on four synthetic data sets[1] (see Table 1), which cover multiple levels of visual and motion complexity. Synthetic stimuli enable us to precisely generate challenging scenarios in a controllable manner in order to disentangle sources of difficulty and glean insights on what models specifically struggle with. We design different scenarios that test complexities that would occur in natural videos such as partial or complete occlusion as well as similar object appearances and complex textures.

Sprites-MOT (**SpMOT**, Table 1 left), as proposed by He et al. (2019), features simple 2D sprites moving linearly on a black background with objects moving in and out of frame during the sequence. **Video-Multi-dSprites** (**VMDS**, Table 1 right) is a video data set we generated based on a colored, multi-object version of the dSprites data set (Matthey et al., 2017). Each video contains one to four sprites that move non-linearly and independently of each other with the possibility of partial or full occlusion. Besides the i.i.d. sampled training, validation and test sets of VMDS, we generate seven additional challenge sets that we use to study specific test situations we observed to be challenging, such as guaranteed occlusion, specific object properties, or out-of-distribution appearance variations. **Video Objects Room** (**VOR**, Table 1 middle) is a video data set we generated based on the static Objects Room data set (Burgess et al., 2019), which features static objects in a 3D room with a moving camera. **Textured Video-Multi-dSprites** (**texVMDS**, Table 3) is based on the generative model of VMDS regarding shapes, number and movement dynamics of the objects, but instead of being uniformly colored the objects feature random texture crops taken from ImageNet (Deng et al., 2009). Additionally, the background is a linearly moving ImageNet crop. For full details on the data sets and their generation, see Appendix B.

---

[1]Data sets are available at this URL.

3.2 Metrics

Our evaluation protocol follows the multi-object tracking (MOT) challenge, a standard and widely-used benchmark for supervised object tracking (Milan et al., 2016). The MOT challenge uses the CLEAR MOT metrics (Bernardin and Stiefelhagen, 2008), which quantitatively evaluate different performance aspects of object detection, tracking and segmentation. To compute these metrics, predictions have to be matched to ground truth. Unlike Bernardin and Stiefelhagen (2008) and Milan et al. (2016), we use binary segmentation masks for this matching instead of bounding boxes, which helps us better understand the models' segmentation capabilities. We consider an Intersection over Union (IoU) greater than 0.5 as a match (Voigtlaender et al., 2019). We include an ablation experiment to test how this threshold affects the results. The error metrics used are the fraction of **Misses (Miss)**, **ID switches (ID S.)** and **False Positives (FPs)** relative to the number of ground truth masks. In addition, we report the **Mean Squared Error (MSE)** of the reconstructed image outputs summed over image channels and pixels.

To quantify the overall number of failures, we use the **MOT Accuracy (MOTA)**, which measures the fraction of all failure cases compared to the total number of objects present in all frames. A model with 100% MOTA perfectly tracks all objects without any misses, ID switches or false positives. To quantify the segmentation quality, we define **MOT Precision (MOTP)** as the average IoU of segmentation masks of all matches. A model with 100% MOTP perfectly segments all tracked objects, but does not necessarily track all objects. Further, to quantify detection and tracking performance independent of false positives, we measure the **Mostly Detected (MD)** and **Mostly Tracked (MT)** metrics, the fraction of ground truth objects that have been detected and tracked for at least 80% of their lifespan, respectively. If an ID switch occurs, an object is considered detected but not tracked. For full details regarding the matching process and the evaluation metrics, refer to Appendix A.

3.3 Models

We consider one color-segmentation baseline and three classes of unsupervised object-centric representation learning models: *(1)* a spatial attention model with unconstrained latents, VI-MON, which is our video extension of MONET (Burgess et al., 2019); *(2)* spatial transformer-based attention models, TBA (He et al., 2019) and SCALOR (Jiang et al., 2020); *(3)* a scene mixture model, OP3 (Veerapaneni et al., 2020). At a high-level, these methods share a common structure which is illustrated in Fig. 1a. They decompose an image into a fixed number of *slots* (Burgess et al., 2019), each of which contains an embedding $\mathbf{z}_{t,k}$ and a mask $\mathbf{m}_{t,k}$ of (ideally) a single object. These slots are then combined in a decoding step to reconstruct the image. Below, we briefly describe each method. Appendix C provides a detailed explanation of the methods in a unified mathematical framework.

As a simple baseline, we evaluate the performance of **k-Means** clustering on the RGB pixel values on a per frame basis and tracking performance by frame-to-frame matching based on the IoU of the segmentation masks using Hungarian matching (Kuhn, 1955). For full details refer to Appendix D.1.

Video MONet (VIMON) is our video extension of MONET (Burgess et al., 2019). MONET recurrently decomposes a static scene into slots, using an attention network to sequentially extract attention masks $\mathbf{m}_k \in [0,1]^{H \times W}$ of individual objects k. A Variational

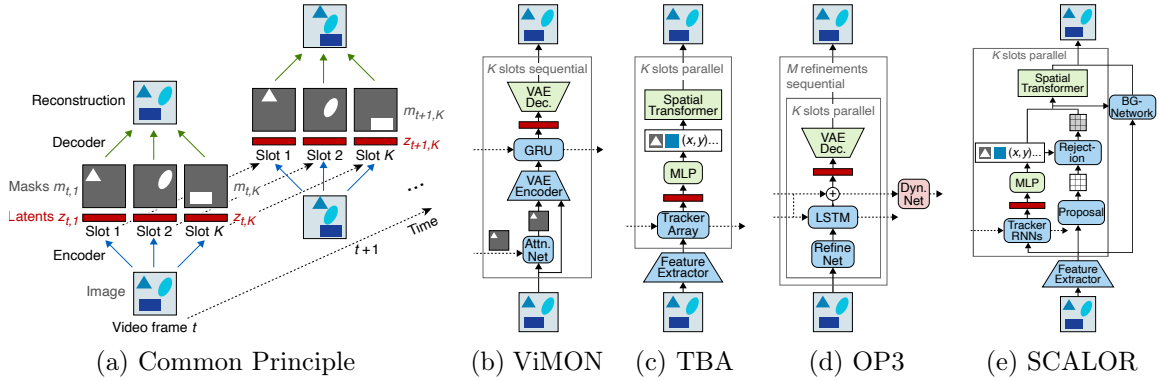(a) Common Principle (b) ViMON (c) TBA (d) OP3 (e) SCALOR

Figure 1: Common principles of all models: Decomposition of an image into a fixed number of slots, each of which contains an embedding $z_{t,k}$ and a mask $m_{t,k}$ of (ideally) a single object. Dotted lines: temporal connections. Solid lines: information flow within one frame.

Autoencoder (VAE) (Kingma and Welling, 2014) encodes each slot into a latent representation $\mathbf{z}_k \in \mathbb{R}^L$ of the corresponding object. We use MONet as a simple frame-by-frame baseline for detection and segmentation that does not employ temporal information. ViMON accumulates evidence about the objects over time to maintain a consistent object-slot assignment throughout the video. This is achieved by (1) seeding the attention network the predicted mask $\widehat{\mathbf{m}}_{t,k} \in [0,1]^{H \times W}$ from the previous time step and (2) introducing a gated recurrent unit (GRU) (Cho et al., 2014), which aggregates information over time for each slot separately, enabling it to encode motion information. For full details on MONet and ViMON, as well as information regarding hyperparameter tuning and ablations to provide context for the design decisions, refer to Appendix C.1, C.2 and E.3.

Tracking-by-Animation (TBA) (He et al., 2019) is a spatial transformer-based attention model. Frames are encoded by a convolutional feature extractor f before being passed to a recurrent block g called Reprioritized Attentive Tracking (RAT). RAT re-weights slot input features based on their cosine similarity with the slots from the previous time step and outputs latent representations for all K slots in parallel. Each slot latent is further decoded into a mid-level representation $\mathbf{y}_{t,k}$ consisting of pose and depth parameters, as well as object appearance and shape templates (see Fig. 1c). For rendering, a Spatial Transformer Network (STN) (Jaderberg et al., 2015) is used with an additional occlusion check based on the depth estimate. TBA is trained on frame reconstruction with an additional penalty for large object sizes to encourage compact bounding boxes. TBA can only process scenes with static backgrounds, as it preprocesses sequences using background subtraction (Bloisi and Iocchi, 2012). For full details on TBA as well as information regarding hyperparameter tuning, refer to Appendix C.3.

Object-centric Perception, Prediction, and Planning (OP3) (Veerapaneni et al., 2020) extends IODINE (Greff et al., 2019) to operate on videos. IODINE decomposes an image into objects and represents them independently by starting from an initial guess of the segmentation of the entire frame, and subsequently iteratively refines it using the refinement network f (Marino et al., 2018). In each refinement step m, the image is represented by K slots with latent representations $\mathbf{z}_{m,k}$. OP3 applies IODINE to each frame x_t to extract latent representations $\mathbf{z}_{t,m,k}$, which are subsequently processed by a dynamics network d (see

Model	MOTA ↑	MOTP ↑	MD ↑	MT ↑	Match ↑	Miss ↓	ID S. ↓	FPs ↓	MSE ↓
				SpMOT					
K-Means	36.2 ± 0.0	77.6 ± 0.0	76.8 ± 0.0	76.3 ± 0.0	80.5 ± 0.0	19.3 ± 0.0	**0.2** ± 0.0	44.3 ± 0.0	-
MONet	70.2 ± 0.8	89.6 ± 1.0	92.4 ± 0.6	50.4 ± 2.4	75.3 ± 1.3	4.4 ± 0.4	20.3 ± 1.6	5.1 ± 0.5	13.0 ± 2.0
ViMON	92.9 ± 0.2	**91.8** ± 0.2	87.7 ± 0.8	87.2 ± 0.8	95.0 ± 0.2	4.8 ± 0.2	**0.2** ± 0.0	2.1 ± 0.1	11.1 ± 0.6
TBA	79.7 ± 15.0	71.2 ± 0.3	83.4 ± 9.7	80.0 ± 13.6	87.8 ± 9.0	9.6 ± 6.0	2.6 ± 3.0	8.1 ± 6.0	11.9 ± 1.9
OP3	89.1 ± 5.1	78.4 ± 2.4	92.4 ± 4.0	91.8 ± 3.8	**95.9** ± 2.2	3.7 ± 2.2	0.4 ± 0.0	6.8 ± 2.9	13.3 ± 11.9
SCALOR	**94.9** ± 0.5	80.2 ± 0.1	**96.4** ± 0.1	**93.2** ± 0.7	95.9 ± 0.4	**2.4** ± 0.0	1.7 ± 0.4	**1.0** ± 0.1	**3.4** ± 0.1
				VOR					
K-Means	-38.0 ± 0.1	76.5 ± 0.0	69.9 ± 0.1	62.9 ± 0.1	72.7 ± 0.1	22.1 ± 0.0	5.2 ± 0.0	110.7 ± 0.1	-
MONet	37.0 ± 6.8	81.7 ± 0.5	76.9 ± 2.2	37.3 ± 7.8	64.4 ± 5.0	15.8 ± 1.6	19.8 ± 3.5	27.4 ± 2.3	12.2 ± 1.4
ViMON	**89.0** ± 0.0	**89.5** ± 0.5	**90.4** ± 0.5	**90.0** ± 0.4	**93.2** ± 0.4	6.5 ± 0.4	0.3 ± 0.0	4.2 ± 0.4	6.4 ± 0.6
OP3	65.4 ± 0.6	89.0 ± 0.6	88.0 ± 0.6	85.4 ± 0.5	90.7 ± 0.3	8.2 ± 0.4	1.1 ± 0.2	25.3 ± 0.6	**3.0** ± 0.1
SCALOR	74.6 ± 0.4	86.0 ± 0.2	76.0 ± 0.4	75.9 ± 0.4	77.9 ± 0.4	22.1 ± 0.4	**0.0** ± 0.0	**3.3** ± 0.2	6.4 ± 0.1
				VMDS					
K-Means	-3.3 ± 0.0	89.8 ± 0.0	**98.3** ± 0.0	93.3 ± 0.1	96.4 ± 0.0	**1.0** ± 0.0	2.6 ± 0.0	99.7 ± 0.0	-
MONet	49.4 ± 3.6	78.6 ± 1.8	74.2 ± 1.7	35.7 ± 0.8	66.7 ± 0.7	13.6 ± 1.0	19.7 ± 0.6	17.2 ± 3.1	22.2 ± 2.2
ViMON	86.8 ± 0.3	86.8 ± 0.0	86.2 ± 0.3	85.0 ± 0.3	92.3 ± 0.2	7.0 ± 0.2	0.7 ± 0.0	5.5 ± 0.1	10.7 ± 0.1
TBA	54.5 ± 12.1	75.0 ± 0.9	62.9 ± 5.9	58.3 ± 6.1	75.9 ± 4.3	21.0 ± 4.2	3.2 ± 0.3	21.4 ± 7.8	28.1 ± 2.0
OP3	**91.7** ± 1.7	**93.6** ± 0.4	96.8 ± 0.5	**96.3** ± 0.4	**97.8** ± 0.1	2.0 ± 0.1	**0.2** ± 0.0	6.1 ± 1.5	**4.3** ± 0.2
SCALOR	74.1 ± 1.2	87.6 ± 0.4	67.9 ± 1.1	66.7 ± 1.1	78.4 ± 1.0	20.7 ± 1.0	0.8 ± 0.0	**4.4** ± 0.4	14.0 ± 0.1

Table 2: Analysis of SOTA object-centric representation learning models for MOT. Results shown as mean ± standard deviation of three runs with different random training seeds.

Fig. 1d), which models both the individual dynamics of each slot k as well as the pairwise interaction between all combinations of slots, aggregating them into a prediction of the posterior parameters for the next time step $t+1$ for each slot k. For full details on IODINE and OP3, refer to Appendix C.4 and C.5, respectively.

SCALable Object-oriented Representation (SCALOR) (Jiang et al., 2020) is a spatial transformer-based model that factors scenes into background and multiple foreground objects, which are tracked throughout the sequence. Frames are encoded using a convolutional LSTM f. In the proposal-rejection phase, the current frame t is divided into $H \times W$ grid cells. For each grid cell a object latent variable $\mathbf{z}_{t,h,w}$ is proposed, that is factored into existence, pose, depth and appearance parameters. Subsequently, proposed objects that significantly overlap with a propagated object are rejected. In the propagation phase, per object GRUs are updated for all objects present in the scene. Additionally, SCALOR has a background module to encode the background and its dynamics. Frame reconstructions are rendered using a background decoder and foreground STNs for object masks and appearance. For full details on SCALOR as well as information regarding hyperparameter tuning, refer to Appendix C.6.

4. Results

We start with a summary of our overall results across the three data sets and four models (Table 2) before analyzing more specific challenging scenarios using variants of the VMDS data set.

A simple color segmentation algorithm is not sufficient to solve tracking even in simplistic data sets (Table 2), in which color is a good predictor for object identity. While k-Means does well at detecting objects, on VMDS even outperforming the other models, its overall tracking performance is significantly worse than the other models, mainly due to a high number of false positives and in SpMOT and VOR also due to a high number of misses, which occur in these two data sets due to multiple objects often having the same color, which a color segmentation algorithm is by definition not able to separate. In the following, we will therefore focus on analyzing the object-centric methods.

We first ask whether tracking could emerge automatically in an image-based model like MONet, which may produce consistent slot assignments through its learned object-slot assignment. This is not the case: MONet exhibits poor tracking performance (Table 2). While MONet correctly finds and segments objects, it does not assign them to consistent slots over time (Fig. E.4). In the following, we will thus focus on the video models: ViMON, TBA, OP3 and SCALOR.

SpMOT. All models perform tracking well on SpMOT with the exception of one training run of TBA with poor results leading to high standard deviation (cp. best TBA model: 89.8% MT; Table E.1). SCALOR outperforms the other models on the detection and tracking metrics MD and MT, while ViMON exhibits the highest MOTP, highlighting its better segmentation performance on SpMOT.

VOR. TBA is not applicable to VOR due to the dynamic background which cannot be resolved using background subtraction. ViMON and OP3 show similarly good performance on detection (MD) and segmentation (MOTP), while ViMON outperforms OP3 on the tracking metrics MOTA and MT. OP3 accumulates a high number of false positives leading to a low MOTA due to the splitting of objects into multiple masks as well as randomly segmenting small parts of the background (Fig. E.5). In contrast, SCALOR has almost no false positives or ID switches, but accumulates a high number of misses leading to a poor MOTA. It often segments two objects as one that are occluding each other in the first frame, which is common in VOR due to the geometry of its scenes (Fig. F.17, last row).

VMDS. OP3 outperforms the other models on VMDS, on which TBA performs poorly, followed by SCALOR, which again accumulates a high number of misses. We will analyze the models on VMDS qualitatively and quantitatively in more detail in the following.

4.1 Impact of IoU Threshold for Matching

To examine whether the IoU threshold used for matching object predictions to ground truth impacts the ordering of the models, we compute all metrics with regard to the IoU thresholds [0.1 .. 0.9] in steps of 0.1 on the VMDS test set. The ordering of the models with regard to their MOTA is consistent over all matching thresholds except for a threshold of 0.9, but the performance difference between the models increases with higher thresholds (Fig. 2a). Thus, we will perform all following experiments with an IoU threshold of 0.5. For all metrics, see Fig. E.6 in Appendix.

4.2 Accumulation of Evidence over Time

Recognition and tracking of objects should improve if models can exploit prior knowledge about the objects in the scene from previous video frames. To test whether the models
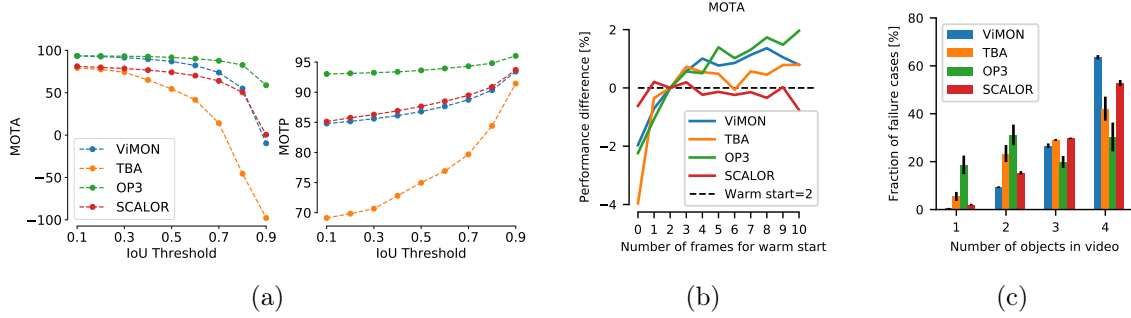
Figure 2: a) MOTA and MOTP performance of models shown for different IoU threshold used for matching model predictions to ground truth objects. Note that MOTA can become negative, since the number of FPs is unbounded. b) MOTA on frames 11–20 of the VMDS test set with warm starts of 1–10 frames (0 = no warm start). Difference to performance of warm start = 2 shown. c) Distribution of failure cases dependent on number of objects in VMDS videos. Mean of three training runs. Error bars: standard deviation.

exploit such knowledge, we evaluate their MOTA performance on VMDS after warm starting with up to 10 frames which are not included in evaluation (Fig. 2b). Note that the models were trained on sequences of length 10, but are run for 20 frames in the case of a warm start of 10 frames. The performance of ViMON improves with longer warm starts, showing that the GRU accumulates evidence over time. TBA, in contrast, does not use temporal information beyond 2–3 frames, while SCALOR's performance slightly drops after 3 frames. OP3 appears to most strongly rely on past information and is able to integrate information over longer time scales: its performance does not even saturate with a warm start of 10 frames. However, the effect for all models is rather small.

4.3 Challenging Scenarios for Different Models

The number of objects in the sequence matters for ViMON, TBA and SCALOR: more objects increase the number of failure cases (Fig. 2c). In contrast, OP3 does not exhibit this pattern: it accumulates a higher number of false positives (FPs) in videos with fewer (only one or two) objects (Fig. E.1), as it tends to split objects into multiple slots if fewer objects than slots are present.

Occlusion leads to failure cases for all models (Fig. 3a–b). Partial occlusion can lead to splitting of objects into multiple slots (Fig. 3a). Objects that reappear after full occlusion are often missed when only a small part of them is visible (Fig. 3a). In particular, SCALOR tends to segment two objects as one when they overlap while entering the scene, leading to a high number of misses.

Color of the object is important. TBA often misses dark objects (Fig. 3b). In contrast, ViMON, OP3 and SCALOR struggle with scenes that feature objects of similar colors as well as objects that have similar colors to the background (Fig. 3c,e).

False positives are more prevalent for OP3 and TBA than for ViMON and SCALOR (Table 2). FPs of OP3 are due to objects split in multiple masks (Fig. 3a) and random
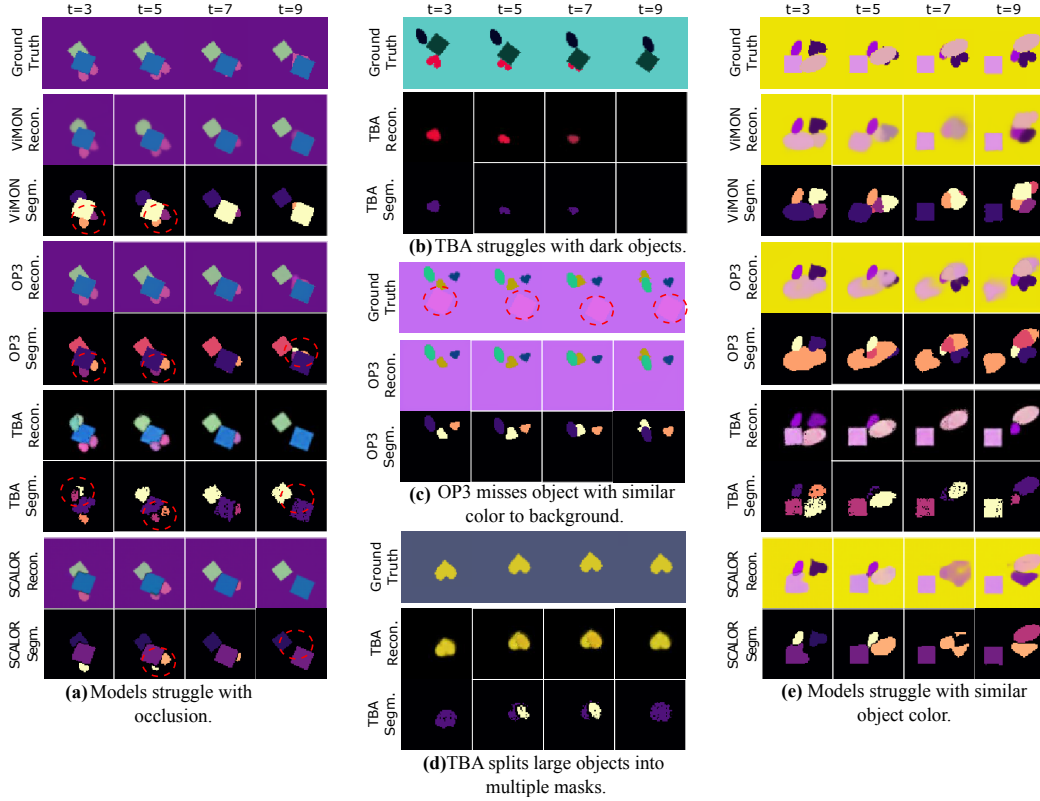
Figure 3: Example failure cases for all models on VMDS. Segmentation masks are binarized and color-coded to signify slot assignment.

small parts of the background being individually segmented (Fig. 3e), while TBA tends to compose larger objects using multiple smaller, simpler components (Fig. 3d).

4.4 Performance on Challenge Sets

Based on the challenging scenarios identified above, we design multiple 'challenge sets': videos featuring *(1)* heavy occlusion, *(2)* objects with same colors, *(3)* only small objects and *(4)* only large objects (Fig. 4a, top). For details, see Appendix B.1.1.

Occlusion reduces performance of all models compared with the i.i.d. sampled VMDS test set, albeit to different degrees (Fig. 4a; for absolute performance see Table E.3). OP3 is more robust to occlusion than the other models.

Tracking objects with the same color is challenging for all models (Fig. 4a). In particular, OP3 appears to rely on object color as a way to separate objects.

OP3, VıMON and SCALOR are not sensitive to object size (Fig. 4a). They exhibit only slightly decreased performance on the large objects test set, presumably because large objects cause more occlusion (Fig. 4a). TBA shows increased performance on small objects but performs poorly on the large objects set.
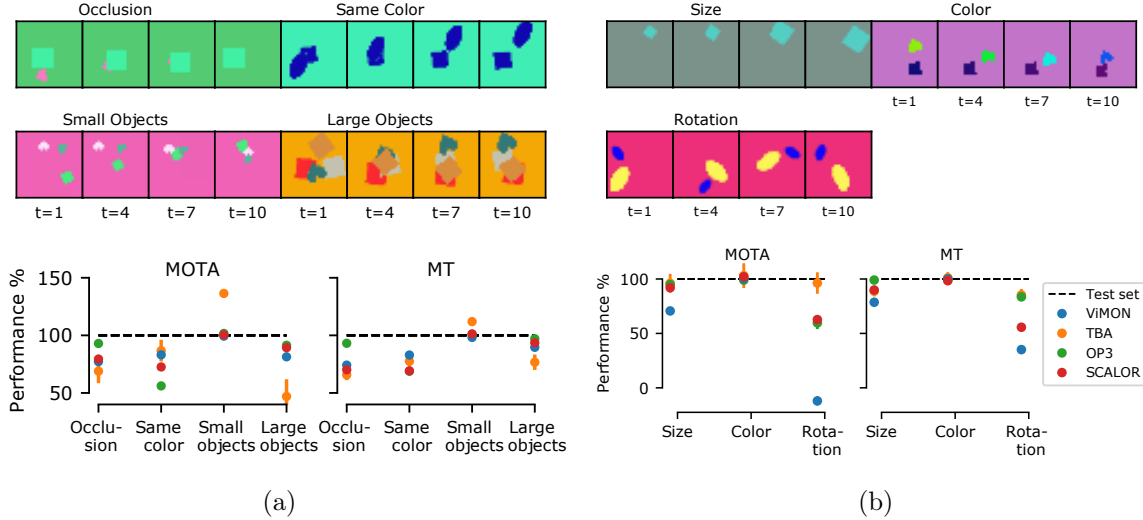
Figure 4: a) Performance on challenge sets relative to performance on VMDS test set (100%) and example video sequences. b) Performance on out-of-distribution sets relative to VMDS test set (100%) and example video sequences. Note that MOTA can become negative, since the number of FPs is unbounded.

4.5 Performance on Out-of-distribution Test Sets

Next, we assess generalization to out-of-distribution (o.o.d.) changes in object appearance that are not encountered during training. In the training set of VMDS, object color, size and orientation are constant throughout a video. To test o.o.d. generalization, we evaluate models trained on VMDS on three data sets that feature unseen object transformations (Fig. 4b and Table E.4): continuous changes in object **color** or **size** as well as continuous **rotation** around the object's centroid while moving. For details, see Appendix B.1.2.

Continuous changes in object size do not pose a serious problem to TBA, OP3 and SCALOR, while ViMON's performance drops (Fig. 4b). Surprisingly, continuous color changes of objects do not impact the performance of any model. Tracking performance of ViMON drops significantly for rotated objects, while OP3 and SCALOR are affected less. TBA's tracking performance is not as strongly influenced by object rotation (for absolute values, see Table E.4).

4.6 Stability of Training and Runtime

TBA and SCALOR train faster and require less memory than OP3 and ViMON (see Table E.5 for details). However, two training runs converged to suboptimal minima for TBA (note the high variance in Table 2 and see Table E.1 and Table E.2 for individual runs). Training OP3 is sensitive to the learning rate and unstable, eventually diverging in all experiments. Interestingly, it often reached its best performance directly prior to divergence. ViMON and TBA are less sensitive to hyperparameter settings in our experiments. For a more detailed analysis of the runtime, see Appendix E.2.

Model	MOTA ↑	MOTP ↑	MD ↑	MT ↑	Match ↑	Miss ↓	ID S. ↓	FPs ↓	MSE ↓
					texVMDS				
K-Means	-99.5 ± 0.0	**76.4** ± 0.0	**25.3** ± 0.0	**24.3** ± 0.1	30.3 ± 0.0	69.2 ± 0.0	0.5 ± 0.0	129.8 ± 0.0	-
MONet	**-73.3** ± 5.5	67.7 ± 1.1	16.0 ± 3.4	12.3 ± 3.1	24.7 ± 4.7	73.1 ± 5.1	2.2 ± 0.8	**98.0** ± 1.7	200.5 ± 5.7
ViMON	-85.5 ± 2.8	69.0 ± 0.6	24.2 ± 1.3	23.8 ± 1.4	**34.7** ± 1.7	**65.0** ± 1.7	0.3 ± 0.0	120.2 ± 2.5	171.4 ± 3.3
OP3	-110.4 ± 4.3	70.6 ± 0.6	16.5 ± 5.1	16.2 ± 5.0	22.9 ± 6.6	76.9 ± 6.7	**0.2** ± 0.1	133.4 ± 2.9	**132.8** ± 16.2
SCALOR	-99.2 ± 11.7	74.0 ± 0.5	6.5 ± 0.6	6.3 ± 0.6	12.3 ± 0.4	87.5 ± 0.4	**0.2** ± 0.0	111.5 ± 11.4	**133.7** ± 11.1

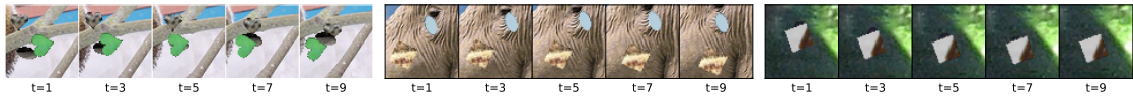t=1 t=3 t=5 t=7 t=9   t=1 t=3 t=5 t=7 t=9   t=1 t=3 t=5 t=7 t=9

Table 3: MOT performance on texVMDS and example video sequences. Results shown as mean ± standard deviation of three runs with different random training seeds. Note that MOTA can become negative, since the number of FPs is unbounded.

4.7 Towards natural data

Object-centric methods have mostly been shown to work on synthetic data sets and seem to rely to a certain extent on color segmentation. To quantify how these methods fare with more realistic images, we created a fourth data set that keeps the simple scene composition of VMDS (1–4 object and few shapes), but has a higher level of visual complexity. To this end, we generated moving object masks as in VMDS, but filled each object and the background with the content of a different image taken from ImageNet (Table 3, bottom). We refer to this data set as *texVMDS*. Humans can easily detect objects in these video through motion cues,[2] while the evaluated models fail at detecting and tracking objects in this data set (Table 3).

Most of the statistics of the objects in texVMDS are identical to those of VMDS (shape, size, velocity, number of objects); the main difference is the visual complexity of the object and background texture. We therefore tune the dimensionality of the latent space for MONet and SCALOR, to account for the higher visual complexity, while keeping all other hyperparameters identical to VMDS. OP3 already has a significantly larger latent dimensionality and uses that for synthetic as well as natural data in their publication. Therefore we keep these hyperparameters. For full details see Appendix D.

TBA is not applicable to texVMDS due to the dynamic background which cannot be resolved using background subtraction. All other models perform poorly. They fail to learn the object boundaries despite the fact that there are only four different object shapes and objects and background move independently, which makes them easy to tell apart for humans. Moreover, they generate large amounts of false positives, often using multiple slots for the background or an object, with the split between slots mostly following color changes (see Fig. F.8, Fig. F.14, Fig. F.18).

5. Discussion

Our experimental results provide insights into the inductive biases and failure cases of object-centric models that were not apparent from their original publications. Despite

---

[2]See `https://eckerlab.org/code/weis2021/` for example videos.

the positive results shown in each of the papers for the evaluated methods, a controlled, systematic analysis demonstrates that they do not convincingly succeed at tracking, which is fundamentally what object-centric video methods should enable.

TBA has a significantly lower MOTP than the other models on all datasets, suggesting that the simple rendering-based decoder using a fixed **template** might be less suitable to generate accurate segmentation masks (see also Fig. F.10 and Fig. F.9) compared to the VAE-based approaches of ViMON, OP3 and SCALOR.

Handling **occlusion** of objects during the video is a key property object-centric representations should be capable of. Qualitatively and quantitatively, OP3 is more robust to occlusion than the other models, suggesting that its dynamics network which models interactions between objects is currently most successful at modeling occluded objects. Surprisingly, TBA and SCALOR, which explicitly encode depth, do not handle occlusion more gracefully than ViMON, whose simpler architecture has no explicit way of dealing with depth. Moving forward, occlusion handling is a key component that object-centric video models need to master. It can be addressed by either equipping the model with a potent interaction module, that takes pairwise interaction between objects (including occlusion) into account, similar to OP3's dynamics model, or ensuring that the depth reasoning of the models works as intended, which may be preferable, as explained below.

All models struggle with detecting objects that have similar **color** as the background (for TBA: dark objects, since background is removed and set to black in a pre-processing step). Color is a reliable cue to identify objects in these datasets. However, the auto-encoding objective incurs little extra loss for missing objects with similar color as the background and, thus, the models appear to not to learn to properly reconstruct them. In order to scale to data with more visual complexity, one might want to replace the pixel-wise reconstruction with for instance a loss based in feature space in order to focus more on reconstructing semantic content rather than high-frequency texture, as is done when using perceptual loss functions (Gatys et al., 2015; Hou et al., 2017) or by using contrastive learning (Kipf et al., 2020). Furthermore, the models—particularly so OP3—struggle with separating objects of similar colors from each other. This result hints at a mismatch between the intuitions motivating these models and what the models actually learn: it should be more efficient in terms of the complexity of the latent representation to decompose two objects—even of similar colors—into two masks with simple shapes, rather than encoding the more complicated shape of two objects simultaneously in one slot. However, since none of the models handle occlusion with amodal segmentation masks (i.e. including the occluded portion of the object) successfully, they learn to encode overly complex (modal) mask shapes. As a consequence, they tend to merge similarly colored objects into one slot. This result suggests that resolving the issues surrounding the depth reasoning in combination with amodal segmentation masks would enable much more compact latents and could also resolve the merging of similarly colored objects.

A major difference between models is the **spatial transformer** based model formulation of TBA and SCALOR, compared to ViMON and OP3, which operate on image-sized masks. The parallel processing of objects and the processing of smaller bounding boxes renders training TBA and SCALOR to be significantly faster and more memory efficient, enabling them to scale to a larger number of objects. On the downside, the spatial transformer introduces its own complications. TBA depends strongly on its prior on object size and

performs well only when this prior fits the data well as well as when the data contains little variation in object sizes, as in SpMOT (Table 2). However, it is not able to handle VMDS and its larger variation in object sizes and shapes. SCALOR performs tracking well in scenes where objects are clearly separated, but struggles to separate objects that partially occlude each other when entering the scene. This difficulty is caused by its discovery mechanism which can propose at most one bounding box per grid cell, leading to a high number of misses on data sets which feature significant occlusion (VOR and VMDS). Unfortunately, simply increasing the number of proposals does not provide a simple solution, as SCALOR's performance is sensitive to properly tweaking the number of proposals.

Choosing a class of models is therefore dependent on the data set one wants to apply it to as well as the computational resources at one's disposal. Data sets that feature a high number of objects (>10) that are well separated from each other make a method like SCALOR, which can process objects in parallel, advisable. On data sets with a lower number of objects per scene which feature heavy occlusion, methods like OP3 and ViMON will likely achieve better results, but require a high computational budget for training.

In conclusion, our analysis shows that none of the models solve the basic challenges of tracking even for relatively simple synthetic data sets. Future work should focus on developing robust mechanisms for reliably handling depth and occlusion, additionally combining the transformer-based efficiency of TBA and SCALOR with the stable training of ViMON and the interaction model of OP3. The key open challenges for scaling these models to natural videos include their computational inefficiency, complex training dynamics, as well as over-dependence on simple appearance cues like color.

Acknowledgments

Appendices

In the appendix, we first discuss the metrics used (Section A) and describe the data generation process (Section B). We then describe the methods MONET, VIMON, TBA, IODINE, OP3 and SCALOR (Section C). Section D contains information regarding the implementation details and training protocols. Finally, we provide additional qualitative and quantitative experimental results in Section E.

Appendix A. Evaluation Protocol Details

We quantitatively evaluate all models on three data sets using the standard CLEAR MOT metrics (Bernardin and Stiefelhagen, 2008). Our evaluation protocol is adapted from the multi-object tracking (MOT) challenge (Milan et al., 2016), a standard computer vision benchmark for supervised object tracking. In particular, we focus on the metrics provided by the py-motmetrics package[3].

A.1 Mapping

In each frame, object predictions of each model in the form of binary segmentation masks are mapped to the ground truth object segmentation masks. We require that each pixel is uniquely assigned to at most one object in the ground truth and the predictions, respectively. Matching is based on the Intersection over Union (IoU) between the predictions and the ground truth masks (Voigtlaender et al., 2019). A valid correspondence between prediction and object has to exceed a threshold in IoU of 0.5. Predictions that are not mapped to any ground truth mask are classified as false positives (FPs). Ground truth objects that are not matched to any prediction are classified as misses. Following (Bernardin and Stiefelhagen, 2008), ground truth objects that are mapped to two different hypothesis IDs in subsequent frames are classified as ID switches for that frame.

A.2 MOT Metrics

MOT Accuracy (MOTA) measures the fraction of all failure cases, i.e. false positives (FPs), misses and ID switches compared to total number of objects present in all frames. **MOT Precision (MOTP)** measures the total accuracy in position for matched object hypothesis pairs, relative to total number of matches made. We use percentage Intersection over Union (IoU) of segmentation masks as the accuracy in position for each match. **Mostly Tracked (MT)** is the ratio of ground truth objects that have been tracked for at least 80% of their lifespan.(i.e. 80% of the frames in which they are visible). MT as implemented by py-motmetrics counts trajectories of objects as correctly tracked even if ID switches occur. We use a strictly more difficult definition of MT that counts trajectories with ID switches as correctly detected but not correctly tracked. Consequently, we add the **Mostly Detected (MD)** measure which does not penalize ID switches. **Match**, **Miss**, **ID Switches (ID S.)**

---

[3]`https://pypi.org/project/motmetrics/`

and **FPs** are reported as the fraction of the number of occurrences divided by the total number of object occurrences.

$$\text{MOTA} = 1 - \frac{\sum_{t=1}^{T} M_t + FP_t + IDS_t}{\sum_{t=1}^{T} O_t} \tag{1}$$

where M_t, FP_t, and IDS_t are the number of misses, false positives and ID switches, respectively, for time t, and O_t is the number of objects present in frame t. Note that MOTA can become negative, since the number of FPs is unbounded.

$$\text{MOTP} = \frac{\sum_{t=1}^{T} \sum_{i=1}^{I} d_t^i}{\sum_{t=1}^{T} c_t} \tag{2}$$

where d_t^i is the total accuracy in position for the ith matched object-hypothesis pair measured in IoU between the respective segmentation masks and c_t is the number of matches made in frame t.

Note that we exclude the background masks for ViMON and OP3 before evaluating tracking based on IoU. The Video Object Room (VOR) data set can contain up to three background segments, namely the floor and up to two wall segments. In order to exclude all background slots regardless of whether the model segments the background as one or as multiple masks, we remove all masks before the tracking evaluation that have an IoU of more than 0.2 with one of the ground truth background masks; we empirically tested that this heuristic is successful in removing background masks regardless of whether the models segments it as one or as three separate ones.

Appendix B. Data Set Generation Details

B.1 Video Multi-dSprites (VMDS)

The Multi-DSprites Video data set consists of 10-frame video sequences of 64×64 RGB images with multiple moving sprites per video. In order to test temporal aggregation properties of the models, the test set contains 20 frame-long sequences. Each video contains one to four sprites following the data set proposed in Burgess et al. (2019) that move independently of each other and might partially or fully occlude one another. The sprites are sampled uniformly from the dSprites data set (Matthey et al., 2017) and colored with a random RGB color. The background is uniformly colored with a random RGB color. Random trajectories are sampled per object by drawing x and y coordinates from a Gaussian process with squared exponential covariance kernel $\text{cov}[x_s, x_t] = \exp[-(x_s - x_t)^2/(2\tau^2)]$ and time constant $\tau = 10$ frames, and then shifted by an initial (x, y)-position of the sprite centroid, which is uniformly sampled from $[10, 54]$ to ensure that the object is within the image boundaries. Trajectories that leave these boundaries are rejected. In occlusion scenarios, larger objects are always in front of smaller objects to disambiguate prediction of occlusion. The training set consists of 10,000 examples whereas the validation set as well as the test set contain 1,000 examples each. Additionally, we generated four challenge sets and three out-of-distribution test sets for VMDS that contain specifically challenging scenarios. Each test set consists of 1,000 videos of length 10 frames, which we describe in the following.

B.1.1 VMDS Challenge Sets

Occlusion test set. In each video, one or more objects are heavily occluded and thus often are not visible at all for a few frames. This is ensured by sampling object trajectories that cross path, i.e. at least in one video frame, two objects are centered on the same pixel. The time step and spatial position of occlusion is sampled randomly. Object trajectories are sampled independently as described above and then shifted such that they are at the sampled position of occlusion at time t. Videos contain two to four sprites (Fig. E.3), since at least two objects are necessary for occlusion.

Small Objects. Videos contain one to four sprites with all sprites being of the smallest size present in the original dSprites (Matthey et al., 2017) data set (Fig. E.3). Other than that, it follows the generation process of the regular training and test set.

Large Objects. Videos contain one to four sprites with all sprites being of the largest size present in the original dSprites (Matthey et al., 2017) data set (Fig. E.3). Other than that, it follows the generation process of the regular training and test set.

Same Color. Videos contain two to four sprites which are identically colored with a randomly chosen color. Other than that, it follows the generation process of the regular training and test set (Fig. E.3).

B.1.2 VMDS Out-of-Distribution Test Sets

Rotation test set. Sprites rotate around their centroid while moving. The amount of rotation between two video frames is uniformly sampled between 5 and 40 degrees, and is constant for each object over the course of the video. Direction of rotation is chosen randomly. Rotation is not included as a transformation in the training set (Fig. E.4).

Color change test set. Sprites change their color gradually during the course of the video. The initial hue of the color is chosen randomly as well as the direction and amount of change between two frames, which stays the same for each object over the course of the video. Saturation and value of the color are kept constant. Color changes are not part of the training set (Fig. E.4).

Size change test set. Sprites change their size gradually during the course of the video. The original dSprites data set (Matthey et al., 2017) contains six different sizes per object. For each object, its size is sampled as either the smallest or largest in the first frame as well as a random point in time, at which it starts changing its size. At this point in time, it will either become larger or smaller, respectively, increasing or decreasing each frame to the next larger or smaller size present in the original dSprites data set, until the largest or smallest size is reached. Size changes are not part of the training set (Fig. E.4).

B.1.3 texVMDS

The Textured Multi-DSprites Video data set consists of 10-frame video sequences of 64×64 RGB images with 1–4 moving sprites per video. The background is a linearly moving crop from a uniformly sampled image (Deng et al., 2009) from the ImageNet Large Scale Visual Recognition Challenge dataset (ILSVRC2012) and the texture of each sprite is similarly cropped from a uniformly sampled ILSVRC2012 image (Deng et al., 2009). The direction of the moving background is uniformly sampled from one of 8 directions (up, down, left,

17

right, upper-right, upper-left, lower-right, lower-left). Other than that, texVMDS follows the generation process of the regular VDMS.

B.2 Sprites-MOT (SpMOT)

Sprites-MOT, originally introduced by He et al. (2019), consists of video sequences of length 20 frames. Each frame is a 128×128 RGB image. It features multiple sprites moving linearly on a black background. The sprite can have one of four shapes and one of six colors. For more information, refer to the original paper (He et al., 2019). We generate a training set consisting of 9600 examples, validation set of 384 samples and test set of 1,000 examples using the author-provided public codebase[4]. However, instead of using the default setting of 20 frames per sequence, we instead generate sequences of length 10, in order to facilitate comparison to the other data sets in our study which have only 10 frames per sequence.

Frames are downsampled to a resolution of 64×64 for training ViMON, OP3 and SCALOR.

B.3 Video Objects Room (VOR)

We generate a video data set based on the static 3D Objects Room data set (Burgess et al., 2019), with sequences of length 10 frames each at a resolution of 128×128. This data set is rendered with OpenGL using the gym-miniworld[5] reinforcement learning environment. It features a 3D room with up to four static objects placed in one quadrant of the room, and a camera initialized at the diagonally opposite quadrant. The objects are either static cubes or spheres, assigned one of 6 colors and a random orientation on the ground plane of the room. The camera then follows one of five trajectories moving towards the objects, consisting of a small fixed distance translation and optional small fixed angle of rotation each time step. The wall colors and room lighting are randomized, but held constant throughout a sequence. The training set consists of 10,000 sequences whereas the validation set and the test set contain 1,000 sequences each.

Frames are downsampled to a resolution of 64×64 for training ViMON, OP3 and SCALOR.

Appendix C. Methods

In this section we describe the various methods in a common mathematical framework. For details about implementation and training, please refer to Section D.

C.1 MONet

Multi-Object-Network (MONet) (Burgess et al., 2019) is an object-centric representation model designed for static images. It consists of a recurrent attention network that sequentially extracts attention masks of individual objects and a variational autoencoder (VAE) (Kingma and Welling, 2014) that reconstructs the image region given by the attention mask in each processing step.

---

[4] https://github.com/zhen-he/tracking-by-animation
[5] https://github.com/maximecb/gym-miniworld

Attention Network: The attention network is a U-Net (Ronneberger et al., 2015) parameterized by ψ. At each processing step k, the attention network receives the full image $\mathbf{x} \in [0, 1]^{H \times W \times 3}$ as input together with the scope variable $\mathbf{s}_k \in [0, 1]^{H \times W}$. The scope $\mathbf{s}_k$ keeps track of the regions of the image that haven't been attended to in the previous processing steps and thus remain to be explained. The attention network outputs a soft attention mask $\mathbf{m}_k \in [0, 1]^{H \times W}$ and the updated scope with the current mask subtracted:

$$\mathbf{m}_k = \mathbf{s}_{k-1} \alpha_\psi(\mathbf{x}, s_{k-1}), \tag{3}$$

$$\mathbf{s}_{k+1} = \mathbf{s}_k(1 - \alpha_\psi(\mathbf{x}, \mathbf{s}_k)), \tag{4}$$

where $\alpha_\psi(\mathbf{x}, \mathbf{s}_k) \in [0, 1]^{H \times W}$ is the output of the U-net and $s_0 = \mathbf{1}$. The attention mask for the last slot is given by $\mathbf{m}_K = \mathbf{s}_{K-1}$ to ensure that the image is fully explained, i.e. $\sum_{k=1}^{K} \mathbf{m}_k = \mathbf{1}$.

VAE: The VAE consists of an encoder $g : [0, 1]^{H \times W \times 3} \times [0, 1]^{H \times W} \to \mathbb{R}^{L \times 2}$ and a decoder $h : \mathbb{R}^L \to [0, 1]^{H \times W \times 3} \times [0, 1]^{H \times W}$ which are two neural networks parameterized by ϕ and θ, respectively. The VAE encoder receives as input the full image $\mathbf{x}$ and the attention mask $\mathbf{m}_k$ and computes $(\boldsymbol{\mu}_k, \log \boldsymbol{\sigma}_k)$, which parameterize the Gaussian latent posterior distribution $q_\phi(\mathbf{z}_k|\mathbf{x}, \mathbf{m}_k) = \mathcal{N}(\boldsymbol{\mu}_k, \boldsymbol{\sigma}_k I)$. Using the reparametrization trick (Kingma and Welling, 2014), $\mathbf{z}_k \in \mathbb{R}^L$ is sampled from the latent posterior distribution. $\mathbf{z}_k$ is decoded by the VAE decoder into a reconstruction of the image component $\widehat{\mathbf{x}}_k \in [0, 1]^{H \times W \times 3}$ and mask logits, which are used to compute the reconstruction of the mask $\widehat{\mathbf{m}}_k \in [0, 1]^{H \times W}$ via a pixelwise softmax across slots. The reconstruction of the whole image is composed by summing over the K masked reconstructions of the VAE: $\widehat{\mathbf{x}} = \sum_{k=1}^{K} \widehat{\mathbf{m}}_k \odot \widehat{\mathbf{x}}_k$.

Loss: MONET is trained end-to-end with the following loss function:

$$
\begin{aligned}
L(\phi; \theta; \psi; \mathbf{x}) = &-\log \sum_{k=1}^{K} \mathbf{m}_k p_\theta(\mathbf{x}|\mathbf{z}_k) + \beta D_{\text{KL}}(\prod_{k=1}^{K} q_\phi(\mathbf{z}_k|\mathbf{x}, \mathbf{m}_k) \| p(\mathbf{z})) \\
&+ \gamma \sum_{k=1}^{K} D_{\text{KL}}(q_\psi(\mathbf{m}_k|\mathbf{x}) \| p_\theta(\mathbf{m}_k|\mathbf{z}_k)),
\end{aligned}
\tag{5}
$$

where $p_\theta(\mathbf{x}|\mathbf{z}_k)$ is the Gaussian likelihood of the VAE decoder and $\mathbf{z}_k \in \mathbb{R}^L$ is the latent representation of slot k.

The first two loss terms are derived from the standard VAE objective, the Evidence Lower BOund (ELBO) (Kingma and Welling, 2014), i.e. the negative log-likelihood of the decoder and the Kullback–Leibler divergence between the unit Gaussian prior $p(\mathbf{z}) = \mathcal{N}(\mathbf{0}, I)$ and the latent posterior distribution $q_\phi(\mathbf{z}_k|\mathbf{x}, \mathbf{m}_k)$ factorized across slots. Notably, the decoder log-likelihood term $p_\theta(\mathbf{x}|\mathbf{z}_k)$ constrains only the reconstruction within the mask, since it is weighted by the mask $\mathbf{m}_k$. Additionally, as a third term, the Kullback–Leibler divergence of the attention mask distribution $q_\psi(\mathbf{m}_k|\mathbf{x})$ with the VAE mask distribution $p_\theta(\widehat{\mathbf{m}}_k|\mathbf{z}_k)$ is minimized, to encourage the VAE to learn a good reconstruction of the masks.

C.2 Video MONet

We propose an extension of MONET (Burgess et al., 2019), called Video MONet (VIMON), which accumulates evidence over time about the objects in the scene (Fig. C.1).

VIMON processes a video recurrently by reconstructing one frame at a time and predicting the next frame of the video. The processing of each frame follows a logic similar to MONET with some notable differences. In the following, we use t to indicate the time step in the video and k to indicate the processing step within one video frame.

Attention Network: The attention network of VIMON outputs an attention mask $\mathbf{m}_{t,k} \in [0,1]^{H \times W}$ in each step k conditioned on the full frame $\mathbf{x}_t \in [0,1]^{H \times W \times 3}$, the scope $\mathbf{s}_{t,k} \in [0,1]^{H \times W}$ and additionally the mask $\widehat{\mathbf{m}}_{t,k} \in [0,1]^{H \times W}$ that was predicted by the VAE in the previous time step, in order to provide it with information about which object it should attend to in this specific slot k:

$$\mathbf{m}_{t,k} = \mathbf{s}_{t,k-1}\alpha_\psi(\mathbf{x}_t, \mathbf{s}_{t,k-1}, \widehat{\mathbf{m}}_{t,k}). \tag{6}$$

VAE: The VAE of VIMON consists of an encoder $g(\mathbf{x}_t, \mathbf{m}_{t,k}; \phi)$ and a decoder $h(\mathbf{z}_{t,k}; \theta)$. In contrast to MONET, the encoder in VIMON is followed by a gated recurrent unit (GRU) (Cho et al., 2014) with a separate hidden state $h_{t,k}$ per slot k. Thus, the GRU aggregates information over time for each object separately. The GRU outputs $(\boldsymbol{\mu}_{t,k}, \log \boldsymbol{\sigma}_{t,k})$ which parameterize the Gaussian latent posterior distribution $q_\phi(\mathbf{z}_{t,k}|\mathbf{x}_t, \mathbf{m}_{t,k})$ where $\mathbf{z}_{t,k} \in \mathbb{R}^L$ is the latent representation for slot k at time t:

Figure C.1: **VIMON**. Attention network followed by VAE encoder and GRU computes latent $\mathbf{z}_{t,k}$.

$$\mathbf{z}'_{t,k} = g(\mathbf{x}_t, \mathbf{m}_{t,k}; \phi), \tag{7}$$

$$(\boldsymbol{\mu}_{t,k}, \log \boldsymbol{\sigma}_{t,k}), \mathbf{h}_{t,k} = f(GRU(\mathbf{z}'_{t,k}, \mathbf{h}_{t-1,k}))), \tag{8}$$

$$q_\phi(\mathbf{z}_{t,k}|\mathbf{x}_t, \mathbf{m}_{t,k}) = \mathcal{N}(\boldsymbol{\mu}_{t,k}, \boldsymbol{\sigma}_{t,k}I) \qquad \forall t, k, \tag{9}$$

where g is the VAE encoder and f is a linear layer. The latent representation $\mathbf{z}_{t,k}$ is sampled from the latent posterior distribution using the reparametrization trick (Kingma and Welling, 2014). Subsequently, $\mathbf{z}_{t,k}$ is linearly transformed into $\widehat{\mathbf{z}}_{t+1,k}$ via a learned transformation $\mathbf{A} \in \mathbb{R}^{L \times L}$: $\widehat{\mathbf{z}}_{t+1,k} = \mathbf{A}\mathbf{z}_{t,k}$ with $\widehat{\mathbf{z}}_{t+1,k}$ being the predicted latent code for the next time step $t+1$. Both $\mathbf{z}_{t,k}$ and $\widehat{\mathbf{z}}_{t+1,k}$ are decoded by the shared VAE decoder h_θ into a reconstruction of the image $\widehat{\mathbf{x}}_{t,k} \in [0,1]^{H \times W \times 3}$ and a reconstruction of the mask $\widehat{\mathbf{m}}_{t,k} \in [0,1]^{H \times W}$ as well as $\widehat{\mathbf{x}}_{t+1,k}$ and $\widehat{\mathbf{m}}_{t+1,k}$, respectively.

Loss: VIMON is trained in an unsupervised fashion with the following objective adapted from the MONET loss (Eq. (5)) for videos. To encourage the model to learn about object motion, we include a prediction objective in the form of a second decoder likelihood on the next-step prediction $p_\theta(\mathbf{x}_{t+1}|\widehat{\mathbf{z}}_{t+1,k})$ and an additional mask loss term, which encourages the predicted VAE mask distribution $p_\theta(\widehat{\mathbf{m}}_{t+1,k}|\widehat{\mathbf{z}}_{t+1,k})$ to be close to the attention mask distribution $q_\psi(\mathbf{m}_{t+1,k}|\mathbf{x}_{t+1})$ of the next time step for each slot k:
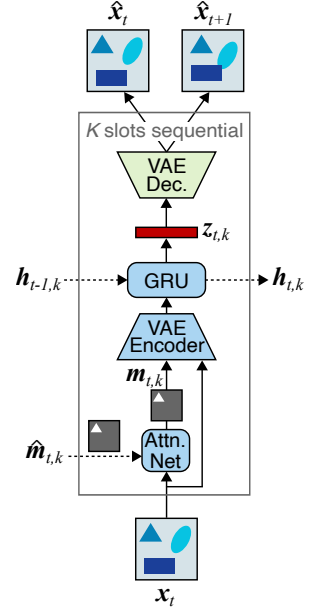
$$L(\phi; \theta; \psi; \mathbf{x}) = \sum_{t=1}^{T} L_{\text{negLL}} + \beta L_{\text{prior}} + \gamma L_{\text{mask}}$$

$$L_{\text{negLL}} = -(\log \sum_{k=1}^{K} \mathbf{m}_{t,k} p_{\theta}(\mathbf{x}_t|\mathbf{z}_{t,k}) + \log \sum_{k=1}^{K} \mathbf{m}_{t+1,k} p_{\theta}(\mathbf{x}_{t+1}|\widehat{\mathbf{z}}_{t+1,k}))$$

$$L_{\text{prior}} = D_{\text{KL}}(\prod_{k=1}^{K} q_{\phi}(\mathbf{z}_{t,k}|\mathbf{x}_t, \mathbf{m}_{t,k})\|p(\mathbf{z}))$$

$$L_{\text{mask}} = \sum_{k=1}^{K} D_{\text{KL}}(q_{\psi}(\mathbf{m}_{t,k}|\mathbf{x}_t)\|p_{\theta}(\mathbf{m}_{t,k}|\mathbf{z}_{t,k})) + D_{\text{KL}}(q_{\psi}(\mathbf{m}_{t+1,k}|\mathbf{x}_{t+1})\|p_{\theta}(\mathbf{m}_{t+1,k}|\widehat{\mathbf{z}}_{t+1,k}))$$

C.3 Tracking-by-Animation

Tracking-by-Animation (TBA) (He et al., 2019) is a spatial transformer-based attention model which uses a simple 2D rendering pipeline as the decoder. Objects are assigned tracking templates and pose parameters by a tracker array, such that they can be reconstructed in parallel using a renderer based on affine spatial transformation (Fig. C.2). In contrast to ViMON, TBA uses explicit parameters to encode the position, size, aspect ratio and occlusion properties for each slot. Importantly, TBA is designed for scenes with static backgrounds, and pre-processes sequences using background subtraction (Bloisi and Iocchi, 2012) before they are input to the tracker array.

Tracker Array: TBA uses a tracker array to output a latent representation $\mathbf{z}_t \in \mathbb{R}^{L \times K}$ at time t using a feature extractor $f(\mathbf{x}_t; \psi)$ and a recurrent 'state update', where $\mathbf{c}_t \in \mathbb{R}^{M \times N \times C}$ is a convolutional feature representation. The convolutional feature and latent representation have far fewer elements than $\mathbf{x}_t$, acting as a bottleneck:

$$\mathbf{c}_t = f(\mathbf{x}_t; \psi), \tag{10}$$

$$\mathbf{h}_{t,k} = RAT(\mathbf{h}_{t-1,k}, \mathbf{c}_t; \pi), \tag{11}$$

$$\mathbf{z}_t = g(\mathbf{h}_t; \phi). \tag{12}$$

Though the state update could be implemented as any generic recurrent neural network block, such as an LSTM (Hochreiter and Schmidhuber, 1997) or GRU (Cho et al., 2014), TBA introduces a Reprioritized Attentive Tracking (RAT) block that uses attention to achieve explicit association of slots with similar features over time. Firstly, the previous tracker state $\mathbf{h}_{t-1,k}$ is used to generate key variables $\mathbf{k}_{t,k}$ and $\beta_{t,k}$:
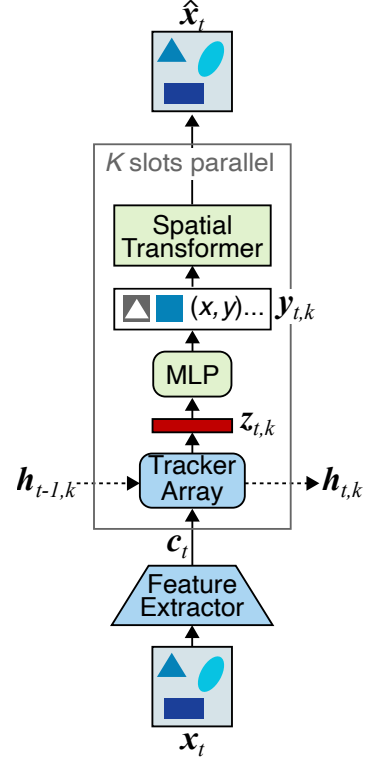

Figure C.2: **TBA**. Feature extractor CNN f and tracker array g to get latent $\mathbf{z}_{t,k}$. MLP h outputs mid-level representation $\mathbf{y}_{t,k}$, and Spatial Transformer renders reconstruction.

$$\{\mathbf{k}_{t,k}, \widehat{\beta}_{t,k}\} = \mathbf{T}\mathbf{h}_{t-1,k}, \tag{13}$$

$$\beta_{t,k} = 1 + \ln(1 + \exp(\widehat{\beta}_{t,k})), \tag{14}$$

where $\mathbf{T}$ is a learned linear transformation, $\mathbf{k}_{t,k} \in \mathbb{R}^S$ is the addressing key, and $\widehat{\beta}_{t,k} \in \mathbb{R}$ is an un-normalized version of a key strength variable $\beta_{t,k} \in (1, +\infty)$. This key strength acts like a temperature parameter to modulate the feature re-weighting, which is described in the following. Each feature vector in $\mathbf{c}_t$, denoted by $\mathbf{c}_{t,m,n} \in \mathbb{R}^S$, where $m \in \{1, 2, \ldots, M\}$ and $n \in \{1, 2, \ldots, N\}$ are the convolutional feature dimensions, is first used to get attention weights:

$$W_{t,k,m,n} = \frac{\exp(\beta_{t,k} Sim(\mathbf{k}_{t,k}, \mathbf{c}_{t,m,n}))}{\sum_{m',n'} \exp(\beta_{t,k} Sim(\mathbf{k}_{t,k}, \mathbf{c}_{t,m',n'}))}. \tag{15}$$

Here, Sim is the cosine similarity defined as $Sim(\mathbf{p}, \mathbf{q}) = \mathbf{p}\mathbf{q}^{\mathsf{T}}/(\|\mathbf{p}\|\|\mathbf{q}\|)$, and $W_{t,k,m,n}$ is an element of the attention weight $\mathbf{W}_{t,k} \in [0, 1]^{M \times N}$, satisfying $\sum_{m,n} W_{t,k,m,n} = 1$. Next, a read operation is defined as a weighted combination of all feature vectors of $\mathbf{c}_t$:

$$\mathbf{r}_{t,k} = \sum_{m,n} W_{t,k,m,n} \, \mathbf{c}_{t,m,n}, \tag{16}$$

where $\mathbf{r}_{t,k} \in \mathbb{R}^S$ is the read vector, representing the associated input feature for slot k. Intuitively, for slots in which objects are present in the previous frame, the model can suppress the features in $\mathbf{r}_{t,k}$ that are not similar to the features of that object, helping achieve better object-slot consistency. On the other hand, if there are slots which so far do not contain any object, the key strength parameter allows $\mathbf{r}_{t,k}$ to remain similar to $\mathbf{c}_t$, facilitating the discovery of new objects.

The tracker state $\mathbf{h}_{t,k}$ of the RAT block is updated with an RNN parameterized by π, taking $\mathbf{r}_{t,k}$ instead of $\mathbf{c}_t$ as its input feature:

$$\mathbf{h}_{t,k} = RNN(\mathbf{h}_{t-1,k}, \mathbf{r}_{t,k}; \pi). \tag{17}$$

The RAT block additionally allows for sequential prioritization of trackers, which in turn allows only a subset of trackers to update their state at a given time step, improving efficiency. For full details on the reprioritization and adaptive computation time elements of the RAT block, please refer to the original paper (He et al., 2019).

Mid-Level Representation: The key feature of TBA is that each latent vector $\mathbf{z}_{t,k}$ is further decoded into a mid-level representation $\mathbf{y}_{t,k} = \{y_{t,k}^c, \mathbf{y}_{t,k}^l, \mathbf{y}_{t,k}^p, \mathbf{Y}_{t,k}^s, \mathbf{Y}_{t,k}^a\}$ corresponding to interpretable, explicit object properties, via a fully-connected neural network $h(\mathbf{z}_{t,k}; \theta)$ as follows:

$$\mathbf{y}_{t,k} = h(\mathbf{z}_{t,k}; \theta). \tag{18}$$

h_θ is shared by all slots, improving parameter efficiency. The different components of the mid-level representation are:

- Confidence $y_{t,k}^c \in [0,1]$: Probability of existence of an object in that slot.

- Layer $\mathbf{y}_{t,k}^l \in \{0,1\}^O$: One-hot encoding of the discretized pseudo-depth of the object relative to other objects in the frame. Each image is considered to be composed of O object layers, where higher layer objects occlude lower layer objects and the background is the zeroth (lowest) layer. E.g., when $O=4$, $\mathbf{y}_{t,k}^l = [0,0,1,0]$ denotes the third layer. For simplicity and without loss of generality, we can also denote the same layer with its integer representation $y_{t,k}^l = 3$.

- Pose $\mathbf{y}_{t,k}^p = [\widehat{s}_{t,k}^x, \widehat{s}_{t,k}^y, \widehat{t}_{t,k}^x, \widehat{t}_{t,k}^y] \in [-1,1]^4$: Normalized object pose for calculating the scale $[s_{t,k}^x, s_{t,k}^y] = [1 + \eta^x \widehat{s}_{t,k}^x, 1 + \eta^y \widehat{s}_{t,k}^y]$ and the translation $[t_{t,k}^x, t_{t,k}^y] = [\frac{W}{2}\widehat{t}_{t,k}^x, \frac{H}{2}\widehat{t}_{t,k}^y]$, where $\eta^x, \eta^y > 0$ are constants.

- Shape $\mathbf{Y}_{t,k}^s \in \{0,1\}^{U \times V}$ and Appearance $\mathbf{Y}_{t,k}^a \in [0,1]^{U \times V \times 3}$: Object template, with hyperparameters U and V typically set much smaller than the image dimensions H and W. Note that the shape is discrete (for details, see below) whereas the appearance is continuous.

In the output layer of h_θ, $y_{t,k}^c$ and $\mathbf{Y}_{t,k}^a$ are generated by the sigmoid function, $\mathbf{y}_{t,k}^p$ is generated by the tanh function, and $\mathbf{y}_{t,k}^l$ as well as $\mathbf{Y}_{t,k}^s$ are sampled from the Categorical and Bernoulli distributions, respectively. As sampling is non-differentiable, the Straight-Through Gumbel-Softmax estimator (Jang et al., 2017) is used to reparameterize both distributions so that backpropagation can still be applied.

Renderer: To obtain a frame reconstruction, the renderer scales and shifts $\mathbf{Y}_{t,k}^s$ and $\mathbf{Y}_{t,k}^a$ according to $\mathbf{y}_{t,k}^p$ via a Spatial Transformer Network (STN) (Jaderberg et al., 2015):

$$\mathbf{m}_{t,k} = STN(\mathbf{Y}_{t,k}^s, \mathbf{y}_{t,k}^p), \tag{19}$$

$$\widehat{\mathbf{x}}_{t,k} = STN(\mathbf{Y}_{t,k}^a, \mathbf{y}_{t,k}^p). \tag{20}$$

where $\mathbf{m}_{t,k} \in \{0,1\}^D$ and $\widehat{\mathbf{x}}_{t,k} \in [0,1]^{D \times 3}$ are the spatially transformed shape and appearance respectively. To obtain the final object masks $\widehat{\mathbf{m}}_{t,k}$, an occlusion check is performed by initializing $\widehat{\mathbf{m}}_{t,k} = y_{t,k}^c \mathbf{m}_{t,k}$, then removing the elements of $\widehat{\mathbf{m}}_{t,k}$ for which there exists an object in a higher layer. That is, for $k=1,2,\ldots,K$ and $\forall j \neq k$ where $y_{t,j}^l > y_{t,k}^l$:

$$\widehat{\mathbf{m}}_{t,k} = (\mathbf{1} - \mathbf{m}_{t,j}) \odot \widehat{\mathbf{m}}_{t,k}. \tag{21}$$

In practice, the occlusion check is sped up by creating intermediate 'layer masks', partially parallelizing the operation. Please see the original paper for more details (He et al., 2019). The final reconstruction is obtained by summing over the K slots, $\widehat{\mathbf{x}}_t = \sum_{k=1}^K \widehat{\mathbf{m}}_{t,k} \odot \widehat{\mathbf{x}}_{t,k}$.

Loss: Learning is driven by a pixel-level reconstruction objective, defined as:

$$L(\phi; \psi; \pi; \theta; \mathbf{x}) = \sum_{t=1}^T \left(MSE(\widehat{\mathbf{x}}_t, \mathbf{x}_t) + \lambda \cdot \frac{1}{K} \sum_{k=1}^K s_{t,k}^x\, s_{t,k}^y \right), \tag{22}$$

where MSE refers to the mean squared error and the second term penalizes large scales $[s_{t,k}^x, s_{t,k}^y]$ in order to make object bounding boxes more compact.

C.4 IODINE

The Iterative Object Decomposition Inference NEtwork (IODINE) (Greff et al., 2019), similar to MONET (Burgess et al., 2019), learns to decompose a static scene into a multi-slot representation, in which each slot represents an object in the scene and the slots share the underlying format of the independent representations. In contrast to MONET, it does not recurrently segment the image using spatial attention, rather it starts from an initial guess of the segmentation of the whole image and iteratively refines it. Thus, the inference component of both models differ, while the generative component is the same.

Iterative Inference: As with MONET, IODINE models the latent posterior $q(\mathbf{z}_k|\mathbf{x})$ per slot k as a Gaussian parameterized by $(\boldsymbol{\mu}_{m,k}, \boldsymbol{\sigma}_{m,k}) \in \mathbb{R}^{L \times 2}$. To obtain latent representations for independent regions of the input image, IODINE starts from initial learned posterior parameters $(\boldsymbol{\mu}_{1,k}, \boldsymbol{\sigma}_{1,k})$ and iteratively refines them using the refinement

Figure C.3: **OP3**. Refinement network f followed by LSTM and dynamics network d compute latent $\mathbf{z}_{t,k}$.

network f_ϕ for a fixed number of refinement steps M. f_ϕ consists of a convolutional neural network (CNN) in combination with an LSTM cell (Hochreiter and Schmidhuber, 1997) parameterized by ϕ. In each processing step, f_ϕ receives as input the image $\mathbf{x} \in [0,1]^{H \times W \times 3}$, a sample from the current posterior estimate $\mathbf{z}_{m,k} \in \mathbb{R}^L$ and various auxiliary inputs $\mathbf{a}_k$, which are listed in the original paper (Greff et al., 2019). The posterior parameters are concatenated with the output of the convolutional part of the refinement network and together form the input to the refinement LSTM. The posterior parameters are additively updated in each step m in parallel for all K slots:

$$(\boldsymbol{\mu}_{m+1,k}, \boldsymbol{\sigma}_{m+1,k}) = (\boldsymbol{\mu}_{m,k}, \boldsymbol{\sigma}_{m,k}) + f_\phi(\mathbf{z}_{m,k}, \mathbf{x}, \mathbf{a}_k). \tag{23}$$

Decoder: In each refinement step m, the image is represented by K latent representations $\mathbf{z}_{m,k}$. Similar to MONET, each $\mathbf{z}_{m,k}$ is independently decoded into a reconstruction of the image $\widehat{\mathbf{x}}_{m,k} \in [0,1]^{H \times W \times 3}$ and mask logits $\widetilde{\mathbf{m}}_{m,k}$, which are subsequently normalized by applying the softmax across slots to obtain the masks $\mathbf{m}_{m,k} \in [0,1]^{H \times W}$. The reconstruction of the whole image at each refinement step m is composed by summing over the K masked reconstructions of the decoder: $\widehat{\mathbf{x}} = \sum_{k=1}^{K} \mathbf{m}_{m,k} \odot \widehat{\mathbf{x}}_{m,k}$.
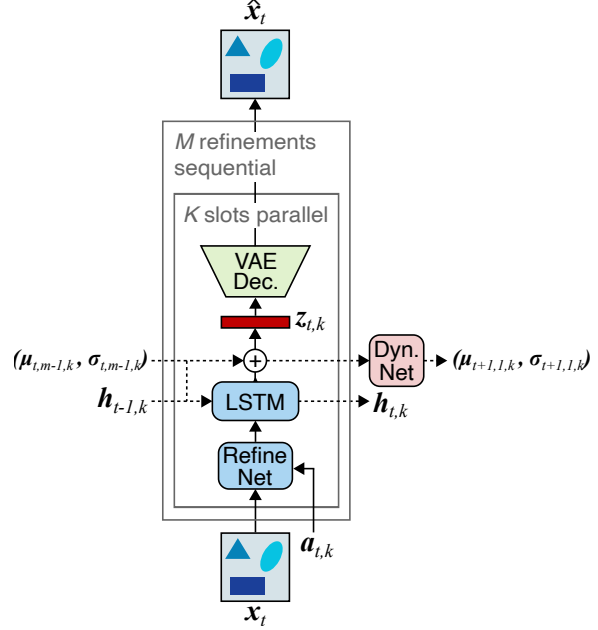
24

Training: IODINE is trained by minimizing the following loss function that consists of the Evidence Lower BOund (ELBO) (Kingma and Welling, 2014) unrolled through N iterations:

$$L(\theta, \phi, (\boldsymbol{\mu}_{1,k}, \boldsymbol{\sigma}_{1,k}); \mathbf{x}) = \sum_{m=1}^{M} \frac{m}{M} \left[-\log \sum_{k=1}^{K} \mathbf{m}_{m,k} p_\theta(\mathbf{x}|\mathbf{z}_{m,k}) + D_{\mathrm{KL}} \left(\prod_{k=1}^{K} q_\phi(\mathbf{z}_{m,k}|\mathbf{x}) \| p(\mathbf{z}) \right) \right],$$
(24)

where $p_\theta(\mathbf{x}|\mathbf{z}_{m,k})$ is the decoder log-likelihood weighted by the mask $\mathbf{m}_k$ and D_{KL} is the Kullback-Leibler divergence between the unit Gaussian prior $p(\mathbf{z}) = \mathcal{N}(\mathbf{0}, I)$ and the latent posterior distribution $q(\mathbf{z}_{m,k}|\mathbf{x})$ factorized across slots.

C.5 Object-centric Perception, Prediction, and Planning (OP3)

Object-centric Perception, Prediction, and Planning (OP3) (Veerapaneni et al., 2020) extends IODINE to work on videos and in a reinforcement learning (RL) setting. It uses the above described IODINE as an observation model to decompose visual observations into objects and represent them independently. These representations are subsequently processed by a dynamics model that models the individual dynamics of the objects, the pairwise interaction between the objects, as well as the action's effect on the object's dynamics, predicting the next frame in latent space (Fig. C.3). By modeling the action's influence on individual objects, OP3 can be applied to RL tasks.

OP3 performs M refinement steps after each dynamics step.

Refinement network: The refinement steps proceed as in the description for IODINE in Section C.4. The input image $\mathbf{x}_t \in [0, 1]^{H \times W \times 3}$, which is the frame from a video at time t, is processed by the refinement network f_ϕ conditioned on a sample from the current posterior estimate $\mathbf{z}_{t,m,k} \in \mathbb{R}^L$. The refinement network outputs an update of the posterior parameters $(\boldsymbol{\mu}_{t,m,k}, \boldsymbol{\sigma}_{t,m,k})$ (see Eq. (23)). The posterior parameters $(\mu_{1,1,k}, \sigma_{1,1,k})$ are randomly initialized.

Dynamics model: After refinement, samples from the current posterior estimate $\mathbf{z}_{t,M,k}$ for each slot k are used as input to the dynamics network. The dynamics model d_ψ consists of a series of linear layers and nonlinearities parameterized by ψ. It models the individual dynamics of the objects per slot k, the pairwise interaction between all combinations of objects, aggregating them into a prediction of the posterior parameters for the next time step $t+1$ for each object k. The full dynamics model additionally contains an action component that models the influence of a given action on each object, which we do not use in our tracking setting. The predicted posterior parameters are then used in the next time step as initial parameters for the refinement network.

$$(\boldsymbol{\mu}_{t,1,k}, \boldsymbol{\sigma}_{t,1,k}) = d_\psi(\mathbf{z}_{t-1,M,k}, \mathbf{z}_{t-1,M,[\neq k]}).$$
(25)

Training. OP3 is trained end-to-end with the ELBO used at every refinement and dynamics step, with the loss $L(\theta, \phi; \mathbf{x})$ given by:

$$\sum_{t=1}^{T} \frac{1}{T} \sum_{m=1}^{M+1} \frac{\min(m, M)}{M} \left(-\log \sum_{k=1}^{K} \mathbf{m}_{t,m,k} p_\theta(\mathbf{x}_t | \mathbf{z}_{t,m,k}) + D_{\mathrm{KL}}(\prod_{k=1}^{K} q_\phi(\mathbf{z}_{t,m,k} | \mathbf{x}_t) \| q(\mathbf{z}_{t,1,k} | \mathbf{x}_t)) \right),$$
(26)

where for time step 1, $q(\mathbf{z}_{1,1,k} | \mathbf{x}_1) = \mathcal{N}(\mathbf{0}, I)$.

C.6 SCALable Object-oriented Representation (SCALOR)

SCALable Object-oriented Representation (SCALOR) (Jiang et al., 2020) is a spatial transformer-based model that extends SQAIR (Kosiorek et al., 2018) to scale to cluttered scenes. Similar to TBA, it factors the latent representations in pose, depth and appearance per object and uses spatial transformers (Jaderberg et al., 2015) to render objects in parallel. In contrast to TBA, it can handle dynamic backgrounds by integrating a background RNN that models background transitions.

Proposal-Rejection Module: SCALOR uses a proposal-rejection module g to discover new objects. All frames up to the current time step $x_{1:t}$ are first encoded using a convolutional LSTM f. The resulting features are then aggregated with an encoding of propagated object masks and divided into $H \times W$ grid cells.

$$\mathbf{c}_t^{img} = f(\mathbf{x}_{1:t}; \psi),$$
(27)

$$\mathbf{c}_t^{mask} = MaskEncoder(M_t^P),$$
(28)

$$\mathbf{c}_t^{agg} = Concat([\mathbf{c}_t^{img}, \mathbf{c}_t^{mask}].$$
(29)

Per grid cell a latent variable $\mathbf{z}_{t,h,w}$ is proposed. Proposal generation is done in parallel. Each $\mathbf{z}_{t,h,w}$ consists of existence, pose, depth and appearance parameters $(\mathbf{z}_{t,h,w}^{pres}, \mathbf{z}_{t,h,w}^{pose}, \mathbf{z}_{t,h,w}^{depth}, \mathbf{z}_{t,h,w}^{what})$.

$$\mathbf{z}_{t,h,w}^{pres} \sim Bern(\cdot | g_1(\mathbf{c}_t^{agg})),$$
(30)

$$\mathbf{z}_{t,h,w}^{depth} \sim \mathcal{N}(\cdot | g_2(\mathbf{c}_t^{agg})),$$
(31)

$$\mathbf{z}_{t,h,w}^{pose} \sim \mathcal{N}(\cdot | g_3(\mathbf{c}_t^{agg})),$$
(32)

where g_1, g_2 and g_3 are convolutional layers.

The appearance parameters $\mathbf{z}_{t,h,w}^{what}$ are obtained by first taking a glimpse from frame x_t of the area specified by $\mathbf{z}_{t,h,w}^{pose}$ via a Spatial Transformer Network (STN) (Jaderberg et al., 2015) and subsequently extracting features from it via a convolutional neural network:

$$\mathbf{c}_{t,h,w}^{att} = STN(x_t, \mathbf{z}_{t,h,w}^{pose}),$$
(33)

$$\mathbf{z}_{t,h,w}^{what} \sim \mathcal{N}(\cdot | GlimpseEnc(\mathbf{c}_{t,h,w}^{att})),$$
(34)

$$\mathbf{o}_{t,h,w}, \mathbf{m}_{t,h,w} = STN^{-1}(GlimpseDec(\mathbf{z}_{t,h,w}^{what}), \mathbf{z}_{t,h,w}^{pose}),$$
(35)

where $\mathbf{o}_{t,h,w}$ is the object RGB glimpse and $\mathbf{m}_{t,h,w}$ is the object mask glimpse.

In the rejection phase, objects that overlap more than a threshold τ in pixel space with a propagated object from the previous time step are rejected.

Propagation Module: During propagation, for each object k from the previous time step $t-1$ a feature attention map $\mathbf{a}_{t,k}$ from the encoded frame features $\mathbf{c}_t^{img}$ is extracted centered on the position of the object in the previous time step and used to update the hidden state $\mathbf{h}_{t,k}$ of the tracker RNN for object k.

$$\mathbf{a}_{t,k} = att(STN(\mathbf{c}_t^{img}, \mathbf{z}_{t-1,k}^{pose}), \tag{36}$$

$$\mathbf{h}_{t,k} = GRU([\mathbf{a}_{t,k}, \mathbf{z}_{t-1,k}], \mathbf{h}_{t-1,k}), \tag{37}$$

$$\mathbf{z}_{t,k} = update(\mathbf{a}_{t,k}, \mathbf{h}_{t,k}, \mathbf{z}_{t-1,k}), \tag{38}$$

where STN is a spatial transformer module (Jaderberg et al., 2015). If $\mathbf{z}_{t,k}^{pres} = 1$ the latent representation $\mathbf{z}_{t,k}$ of the respective object k will be propagated to the next time step.

Background: The background of each frame x_t is encoded using a convolutional neural network conditioned on the masks M_t of the objects present at time step t and decoded using a convolutional neural network.

$$(\boldsymbol{\mu}^{bg}, \boldsymbol{\sigma}^{bg}) = BgEncoder(x_t, (1-M_t)), \tag{39}$$

$$\mathbf{z}_t^{bg} \sim \mathcal{N}(\boldsymbol{\mu}^{bg}, \boldsymbol{\sigma}^{bg}), \tag{40}$$

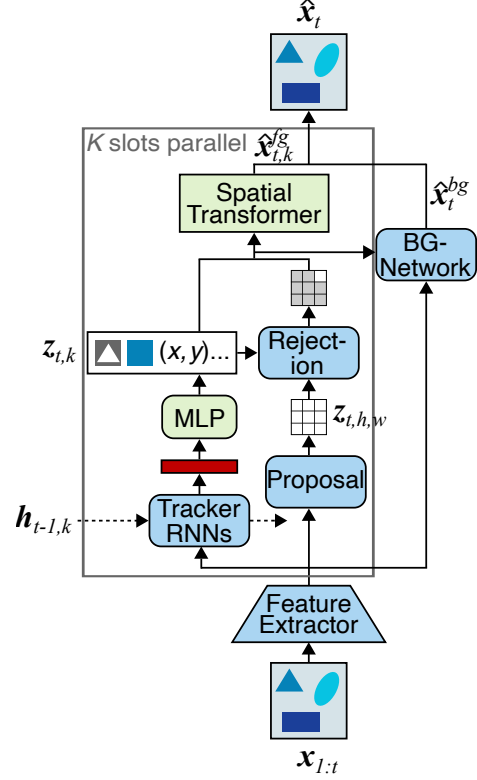$$\widehat{\mathbf{x}}_t^{bg} = BgDecoder(\mathbf{z}_t^{bg}). \tag{41}$$

Figure C.4: **SCALOR** Feature extractor CNN f followed by tracker RNNs or proposal-rejection module to compute latent $\mathbf{z}_{t,k}$. Spatial Transformer in addition to background module renders reconstruction.

Rendering: To obtain frame reconstructions $\widehat{\mathbf{x}}_t$ foreground object appearances and masks are scaled and shifted using via a Spatial Transformer Network (STN):

$$\widehat{\mathbf{x}}_{t,k}^{fg} = STN^{-1}(\mathbf{o}_{t,k}, \mathbf{z}_{t,k}^{pose}), \tag{42}$$

$$\boldsymbol{\gamma}_{t,k} = STN^{-1}(\mathbf{m}_{t,k} \cdot \mathbf{z}_{t,k}^{pres} \sigma(-\mathbf{z}_{t,k}^{depth}), \mathbf{z}_{t,k}^{pose}), \tag{43}$$

$$\widehat{\mathbf{x}}_t^{fg} = \sum_K \widehat{\mathbf{x}}_{t,k}^{fg} \boldsymbol{\gamma}_{t,k}. \tag{44}$$

Subsequently, foreground objects and background reconstruction are combined as follows to obtain the final reconstruction:

$$\widehat{\mathbf{x}}_t = \widehat{\mathbf{x}}_t^{fg} + (1-M_t) \odot \widehat{\mathbf{x}}_t^{bg}. \tag{45}$$

Training: SCALOR is trained on frame reconstruction using the evidence lower bound (ELBO):

$$\sum_{t=1}^{T} -\log p_\theta(\mathbf{x}_t|\mathbf{z}_t) + D_{\mathrm{KL}}(q_\phi(\mathbf{z}_t|\mathbf{z}_{<t}, \mathbf{x}_{\leq t})\|q(\mathbf{z}_t|\mathbf{z}_{<t})). \tag{46}$$

Appendix D. Model Implementation Details

D.1 Baseline: k-Means

As a baseline, we implement a simple color segmentation algorithm to evaluate if this is sufficient to solve the benchmark data sets. To this end, we cluster the videos using the k-Means algorithm as implemented by sklearn (Pedregosa et al., 2011). The number of clusters are chosen equal to the number of slots in the other models, i.e. $K = 5$ for SpMOT, $K = 6$ for VMDS and $K = 8$ for VOR. We run the clustering three times per video with different random seeds. Each pixel is treated as one sample with 3 features (RGB values). k-Means clustering is performed for each frame in the video separately. To obtain the tracking performance, we match objects in consecutive frames using IoU of the extracted segmentation masks with the Hungarian matching algorithm (Kuhn, 1955).

D.2 MONET and Video MONET

VAE: Following Burgess et al. (2019), the VAE encoder is a CNN with 3x3 kernels, stride 2, and ReLU activations (Table D.1). It receives the input image and mask from the attention network as input and outputs (μ, $\log \sigma$) of a 16-dimensional Gaussian latent posterior. The GRU has 128 latent dimensions and one hidden state per slot followed by a linear layer with 32 output dimensions. The VAE decoder is a Broadcast decoder as published by Watters et al. (2019b) with no padding, 3x3 kernels, stride 1 and ReLU activations (Table D.2). The output distribution is an independent pixel-wise Gaussian with a fixed scale of $\sigma = 0.09$ for the background slot and $\sigma = 0.11$ for the foreground slots.

Attention Network: The attention network is a U-Net (Ronneberger et al., 2015) and follows the architecture proposed by Burgess et al. (2019). The down- and up-sampling components consist each of five blocks with 3x3 kernels, 32 channels, instance normalization, ReLU activations and down- or up-sampling by a factor of two. The convolutional layers are bias-free and use stride 1 and padding 1. A three-layer MLP with hidden layers of size 128 connect the down- and the up-sampling part of the U-Net.

Training: MONET and VIMON are implemented in PyTorch (Paszke et al., 2019) and trained with the Adam optimizer (Kingma and Ba, 2015) with a batch size of 64 for MONET and 32 for VIMON, using an initial learning rate of 0.0001. Reconstruction performance is evaluated after each epoch on the validation set and the learning rate is decreased by a factor of 3 after the validation loss has not improved in 25 consecutive epochs for MONET and 100 epochs for VIMON, respectively. MONET and VIMON are trained for 600 and 1000 epochs, respectively. The checkpoint with the lowest reconstruction error is selected for the final MOT evaluation. MONET is trained with $\beta = 0.5$ and $\gamma = 1$ and VIMON is trained with $\beta = 1$ and $\gamma = 2$. $K = 5$ for SpMOT, $K = 6$ for VMDS and $K = 8$ for VOR. Due to the increased slot number for VOR, batch size for VIMON had to be decreased to

Type	Size/Ch.	Act. Func.	Comment
Input	4		RGB + Mask
Conv 3x3	32	ReLU	
Conv 3x3	32	ReLU	
Conv 3x3	64	ReLU	
Conv 3x3	64	ReLU	
MLP	256	ReLU	
MLP	32	Linear	

Table D.1: Architecture of VIMON **VAE Encoder**.

Type	Size/Ch.	Act. Func.	Comment
Input	16		
Broadcast	18		+ coordinates
Conv 3x3	32	ReLU	
Conv 3x3	32	ReLU	
Conv 3x3	32	ReLU	
Conv 3x3	32	ReLU	
Conv 1x1	4	Linear	RGB + Mask

Table D.2: Architecture of VIMON **VAE Decoder**.

24 to fit into the GPU memory. Respectively, the initial learning rate is set to 0.000075 for VIMON on VOR. We initialize the attention network and the VAE in VIMON with the pre-trained weights from MONET to facilitate learning and speed up the training. Note that for all evaluations, the reconstructed masks $\widehat{\mathbf{m}}$ from the VAE were used.

Sprites-MOT Initialization: When training MONET and Video MONET on Sprites-MOT from scratch, MONET struggles to learn the extreme color values of the objects that Sprites-MOT features. Instead it completely focuses on learning the shapes. To circumvent that, we initialized the weights of the models with MONET weights that were trained for 100 epochs on Multi-dSprites.

Hyperparameter tuning: Hyperparameters for MONET and VIMON were selected using the best MSE on the validation set of VMDS. Hyperparameter tuning for MONET included β from $\{0.5, 1.0\}$ and γ from $\{0.5, 1.0, 2.0\}$ and initial learning rate from $\{1e\text{-}05, 1e\text{-}04\}$.

Hyperparameter tuning for VIMON included β from $\{0.5, 1.0\}$ and γ from $\{1.0, 2.0, 5.0, 10.0, 50.0\}$ and initial learning rate from $\{1e\text{-}05, 1e\text{-}04, 1e\text{-}03\}$.

Hyperparameters for **texVMDS** were kept fixed to the best selected hyperparameters for VMDS, except for the VAE latent dimension, which is tuned to account for the higher visual complexity. The VAE latent dimension 16 is selected from $\{16, 32, 64, 128\}$ as the one with the best MOTA for MONET on texVMDS validation set — analogous to the SCALOR hyperparameter tuning paradigm — and subsequently also used for training of VIMON on texVMDS.

D.3 Tracking by Animation

Preprocessing: TBA expects its input frames to contain only foreground objects. In He et al. (2019), the authors use Independent Multimodal Background Subtraction (IMBS) (Bloisi and Iocchi, 2012) to remove the background from data sets consisting of natural videos with static backgrounds. Background subtraction algorithms maintain a spatio-temporal window around each pixel in the sequence, and remove the dominant mode based on a histogram of color values. Since the default implementation of IMBS has several hand-tuned thresholds corresponding to natural videos (e.g., for shadow suppression), it cannot be directly applied to synthetic data sets like VMDS without significant hyperparameter tuning. We instead re-generate all of the VMDS data sets with identical objects and motion but a black background for our experiments with TBA, to mimic a well-tuned background subtraction algorithm.

Architecture: For SpMOT, we follow the same architecture as in (He et al., 2019), while we increase the number of slots from $K = 4$ to $K = 5$ and number of layers from $O = 3$ to $O = 4$ for VMDS. Since TBA does not model the background, this makes the number of foreground slots equal to the other models in our study.

Hyperparameter tuning: Further, we increase the size prior parameters $U \times V$ used for the shape and appearance templates from 21×21 which is used for SpMOT, to 64×64 for VMDS, which we empirically found gave the best validation loss among 48×48, 56×56, 64×64 and 72×72. All other architectural choices are kept fixed for both data sets, and follow He et al. (2019). Note that due to this, we trained the TBA models at its default resolution of 128×128 unlike the 64×64 resolution used by MONet and OP3.

Training and Evaluation: We train for 1000 epochs using the same training schedule as He et al. (2019). The checkpoint with the lowest validation loss is selected for the final MOT evaluation. Further, we observed that the discrete nature of the shape code used in TBA's mid-level representation leads to salt-and-pepper noise in the reconstructed masks. We therefore use a 2×2 minimum pooling operation on the final output masks to remove isolated, single pixel foreground predictions and generate 64×64 resolution outputs, similar to MONet and OP3 before evaluation.

Deviation of SpMOT results compared to original publication: Our results were generated with 100k training frames, while the original TBA paper (He et al., 2019) uses 2M training frames for the simple SpMOT task. Further, we report the mean of three training runs, while the original paper reports one run (presumably the best). Our best run achieves MOTA of 90.5 (Table E.1). Third, we evaluate using intersection over union (IoU) of segmentation masks instead of bounding boxes.

D.4 OP3

Training: The OP3 loss is a weighted sum over all refinement and dynamics steps (Eq. (26)). For our evaluation on multi-object tracking, we weight all time steps equally. In contrast to the original training loss, in which the weight value is linearly increased indiscriminately, thus weighting later predictions more highly, we perform the linear increase only for the refinement steps between dynamics steps, thus weighting all predictions equally.

OP3, as published by Veerapaneni et al. (2020), uses curriculum learning. For the first 100 epochs, M refinement steps are taken, followed by a single dynamics step, with a final

refinement step afterwards. Starting after 100 epochs, the number of dynamics steps is incremented by 1 every 10 epochs, until five dynamics steps are reached. Thus, only 5 frames of the sequence are used during training at maximum.

We chose to use an alternating schedule for training, where after each dynamics step, $M = 2$ refinement steps are taken, and this is continued for the entire sequence. Thus, the entire available sequence is used, and error is not propagated needlessly, since the model is enabled to refine previous predictions on the reconstruction before predicting again. Note that this is the schedule OP3 uses by default at test-time, when it is used for model predictive control. Note that we still use 4 refinement steps on the initial observation to update the randomly initialized posterior parameters, as in the released implementation. We split all 10-step sequences into 5-step sequences to avoid premature divergence.

Hyperparameter tuning: Note that OP3 by default uses a batch size of 80 with the default learning rate of 0.0003. As we found training OP3 to be very unstable, leading to eventual divergence in almost all experiments that have been performed for this study, we tested batch sizes [64, 32, 16, 8] and found reducing the batch size significantly, to 16, improved performance. We found the default learning rate to be too large for SpMOT in particular, as the model diverged significantly earlier than on VMDS and VOR. We tested learning rates [0.0002, 0.0001, 0.00006, 0.00003], and found decreasing the learning rate to 0.0001 rectified the observed premature divergence.

The checkpoint prior to divergence with the lowest KL loss is selected for the final MOT evaluation, as the KL loss enforces consistency in the latents over the sequence. Interestingly, the checkpoint almost always corresponded to the epochs right before divergence.

D.5 SCALOR

Architecture: We follow the same architecture as in Jiang et al. (2020). We use a grid of 4×4 for object discovery with a maximum number of objects of 10. The standard deviation of the image distribution is set to 0.1. Size anchor and variance are set to 0.2 and 0.1, respectively.

For SpMOT, background modeling is disabled and the dimensionality of the latent object appearance is set to 8.

For VMDS, the dimensionality of background is set to 3 and the dimensionality of the latent object appearance is set to 16. For object discovery, a grid of 3×3 cells with a maximum number of objects of 8 is used.

For VOR, the dimensionality of background is set to 8 and the dimensionality of the latent object appearance is set to 16.

For texVMDS, the dimensionality of background is set to 32 and the dimensionality of the latent object appearance is set to 16. For object discovery, a grid of 3×3 cells with a maximum number of objects of 8 is used.

Best model checkpoint according to the validation loss was chosen for MOT evaluation.

Hyperparameter tuning: For VMDS, we run hyperparameter search over number of grid cells $\{3 \times 3, 4 \times 4\}$, background dimension $\{1, 3, 5\}$, maximum number of objects $\{5, 8, 10\}$ (dependent on number of grid cells), size anchor $\{0.2, 0.25, 0.3, 0.4\}$, z^{what} dimensionality $\{8, 16, 24\}$ and end value of τ $\{0.3, 0.5\}$.

For SpMOT, we run hyperparameter search over maximum number of objects {4, 10}, size anchor {0.1, 0.2, 0.3}, z^{what} dimensionality {8, 16} and whether to model background (with background dimensionality 1) or not.

For VOR, we run hyperparameter search over size anchor {0.2, 0.3} and background dimensionality {8, 12}.

For texVMDS, we keep hyperparameters fixed as for VMDS and only tune background dimension {3, 8, 16, 32, 64, 128} and z^{what} dimensionality {16, 32, 64, 128} to account for the higher visual complexity of the data set.

We picked best hyperparameters according to the validation loss with the exception of the data set texVMDS, for which the best validation loss was given by the model using a latent dimensionality of 128 for both background and object. This led to the model using only the background slot to reconstruct the whole frame without using the object slots (object matches ~3%). As a sanity check, we picked the model which had the best MOTA on the validation set (shown in Table 3), but it also did not perform well on the more complex texVMDS data set.

We additionally tested if down-weighing the log-likelihood during training by a factor of 10, while keeping the high latent dimensionality (128 for both z^{what} and background) would help, by decreasing the focus on reconstructing the high frequency textures, but it still relied on the background to reconstruct the image without using object slots.

Training: We train SCALOR with a batch size of 16 for 300 epochs using a learning rate of 0.0001 for SpMOT and VOR and for 400 epochs for VMDS. For the final MOT evaluation, the checkpoint with the lowest loss on the validation set is chosen.

Appendix E. Additional Results

Table E.1 lists the individual results for the three training runs with different random seeds per model and data set. The results of VIMON and SCALOR are coherent between the three runs with different random seed, while TBA has one run on SpMOT with significantly lower performance than the other two and shows variation in the three training runs on VMDS. OP3 exhibits one training run on SpMOT with lower performance than the other two.

Fig. E.2 shows the fraction of failure cases dependent on the number of objects over all types of failures (misses, ID. switches and FPs). Fig. E.1 shows the fraction of failure cases dependent on the number of objects present in the video for the three different failure cases separately; ID switches, FPs and misses. For VIMON, TBA and SCALOR, the number of failures increase with the number of objects present regardless of the type of failure. In contrast, OP3 shows this pattern for ID switches and misses, while it accumulates a higher number of false positives (FPs) in videos with fewer (only one or two) objects.

Fig. E.4 shows a comparison between MONET and VIMON on VMDS. MONET correctly finds and segments objects, but it does not assign them to consistent slots over time, while VIMON maintains a consistent slot assignment throughout the video.

Fig. E.5 shows failures cases of OP3 on VOR.

Table E.3 and Table E.4 list the results for the four models, VIMON, TBA, OP3 and SCALOR, on the VMDS challenge sets and out-of-distribution (o.o.d.) sets respectively.

Model	Run	MOTA ↑	MOTP ↑	MD ↑	MT ↑	Match ↑	Miss ↓	ID S. ↓	FPs ↓	MSE ↓
					SpMOT					
K-MEANS	1	36.2	77.6	76.8	76.3	80.5	19.2	0.2	44.3	-
	2	36.2	77.6	76.8	76.3	80.5	19.2	0.2	44.3	-
	3	36.3	77.6	76.8	76.2	80.5	19.3	0.2	44.2	-
MONET	1	70.0	90.6	92.8	49.4	74.7	4.1	21.2	4.7	10.4
	2	69.4	90.0	92.7	48.1	74.2	4.1	21.6	4.8	13.4
	3	71.3	88.1	91.6	53.8	77.1	4.9	18.0	5.8	15.2
VIMON	1	92.7	92.0	87.5	87.0	94.9	4.9	0.2	2.2	10.5
	2	92.8	92.0	86.9	86.3	94.8	5.0	0.2	2.0	11.8
	3	93.2	91.6	88.8	88.3	95.2	4.6	0.2	2.0	10.9
TBA	1	90.5	71.4	90.2	89.8	94.4	5.3	0.3	3.9	10.3
	2	58.4	70.7	69.6	60.8	75.0	18.1	6.9	16.6	14.6
	3	90.1	71.5	90.3	89.4	94.0	5.5	0.5	3.9	10.9
OP3	1	92.4	80.0	94.5	93.7	97.3	2.4	0.4	4.8	4.3
	2	81.9	74.9	86.9	86.5	92.8	6.8	0.3	10.9	30.1
	3	92.9	80.1	95.9	95.2	97.6	2.0	0.4	4.7	5.6
SCALOR	1	94.4	80.1	96.5	92.3	95.4	2.4	2.2	1.0	3.3
	2	94.7	80.2	96.4	93.1	95.8	2.4	1.8	1.1	3.4
	3	95.5	80.2	96.3	94.0	96.4	2.4	1.2	0.9	3.6
					VOR					
K-MEANS	1	-38.0	76.5	69.8	62.8	72.6	22.1	5.3	110.7	-
	2	-38.1	76.5	69.8	63.0	72.7	22.1	5.2	110.8	-
	3	-37.9	76.5	70.0	62.9	72.8	22.0	5.2	110.7	-
MONET	1	28.0	81.3	73.8	26.7	57.4	18.0	24.6	29.4	14.1
	2	44.5	82.4	78.2	45.4	68.7	15.0	16.3	24.2	11.8
	3	38.5	81.6	78.7	39.8	67.0	14.4	18.5	28.5	10.8
VIMON	1	89.0	88.9	90.2	89.8	92.9	6.8	0.3	3.9	7.1
	2	89.0	89.8	89.9	89.6	93.0	6.8	0.2	4.0	6.2
	3	89.0	89.9	91.0	90.6	93.8	6.0	0.2	4.8	5.9
OP3	1	64.8	89.5	87.2	85.1	90.3	8.8	0.9	25.5	3.1
	2	66.2	88.1	88.6	85.1	90.7	7.9	1.4	24.5	2.9
	3	65.3	89.3	88.2	86.1	91.1	8.0	0.9	25.8	3.0
SCALOR	1	74.1	85.8	75.6	75.5	77.4	22.6	0.0	3.3	6.4
	2	74.6	86.0	75.9	75.9	78.1	21.9	0.1	3.5	6.4
	3	75.1	86.1	76.5	76.4	78.2	21.7	0.0	3.1	6.3

Table E.1: Analysis of SOTA object-centric representation learning models for MOT. Results for three runs with different random training seeds.

Model	Run	MOTA ↑	MOTP ↑	MD ↑	MT ↑	Match ↑	Miss ↓	ID S. ↓	FPs ↓	MSE ↓
					VMDS					
K-MEANS	1	-3.3	89.8	98.3	93.4	96.4	1.0	2.6	99.7	-
	2	-3.3	89.8	98.2	93.2	96.4	1.1	2.6	99.7	-
	3	-3.2	89.8	98.2	93.4	96.4	1.0	2.6	99.6	-
MONET	1	51.7	79.6	75.1	36.7	67.6	12.9	19.5	15.9	20.8
	2	44.3	76.1	71.8	34.8	65.9	15.0	19.1	21.5	25.3
	3	52.2	80.2	75.6	35.5	66.5	13.0	20.5	14.2	20.4
VIMON	1	87.0	86.8	86.7	85.4	92.4	6.8	0.7	5.5	10.6
	2	87.1	86.8	86.1	85.1	92.3	7.1	0.6	5.3	10.8
	3	86.5	86.7	86.0	84.6	92.1	7.2	0.7	5.6	10.6
TBA	1	68.5	76.1	69.3	65.3	80.7	16.5	2.8	12.2	26.0
	2	38.9	73.8	55.1	50.5	70.2	26.6	3.2	31.3	30.8
	3	56.0	75.0	64.3	59.2	76.7	19.8	3.5	20.8	27.5
OP3	1	93.1	94.2	97.2	96.7	98.0	1.9	0.2	4.9	4.0
	2	92.7	93.4	96.9	96.3	97.8	2.0	0.2	5.1	4.3
	3	89.4	93.3	96.2	95.8	97.6	2.2	0.2	8.3	4.6
SCALOR	1	75.7	88.1	69.4	68.3	79.8	19.4	0.8	4.0	13.9
	2	72.7	87.2	66.7	65.6	77.6	21.6	0.8	4.9	14.2
	3	73.7	87.6	67.5	66.2	77.9	21.2	0.9	4.2	14.0
					texVMDS					
K-MEANS	1	-99.5	76.4	25.4	24.3	30.3	69.2	0.5	129.8	-
	2	-99.5	76.4	25.3	24.4	30.4	69.2	0.5	129.9	-
	3	-99.5	76.4	25.3	24.3	30.3	69.2	0.5	129.8	-
MONET	1	-70.8	67.1	15.5	13.4	24.9	73.9	1.2	95.7	203.0
	2	-68.1	69.2	20.4	15.4	30.4	66.5	3.1	98.6	192.5
	3	-80.9	66.7	12.1	8.1	18.9	78.9	2.2	99.8	205.9
VIMON	1	-88.2	68.3	24.2	23.8	35.5	64.2	0.3	123.7	174.6
	2	-86.6	69.0	22.6	22.0	32.4	67.4	0.3	119.0	172.7
	3	-81.6	69.8	25.8	25.4	36.3	63.4	0.3	117.9	166.9
OP3	1	-105.6	71.5	20.6	20.4	28.3	71.6	0.2	133.9	113.6
	2	-116.0	70.1	9.4	9.2	13.6	86.3	0.1	129.6	153.2
	3	-109.7	70.3	19.5	19.0	26.9	72.8	0.3	136.6	131.8
SCALOR	1	-84.8	73.3	6.4	6.3	12.5	87.3	0.2	97.3	149.5
	2	-99.5	74.4	7.3	7.0	12.7	87.1	0.3	112.1	125.0
	3	-113.4	74.4	5.8	5.6	11.8	88.0	0.3	125.2	126.7

Table E.2: Analysis of SOTA object-centric representation learning models for MOT. Results for three runs with different random training seeds.
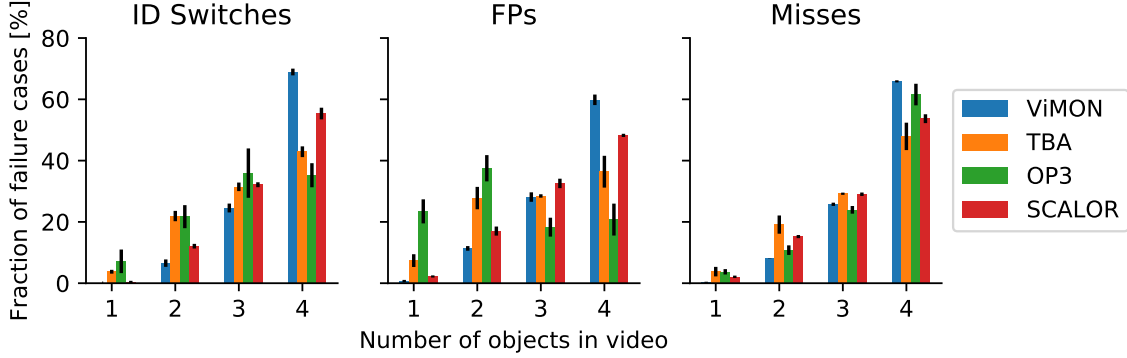
Figure E.1: Distribution of failure cases dependent on number of objects in VMDS videos split by failure class. Mean of three training runs. Error bars: SD.
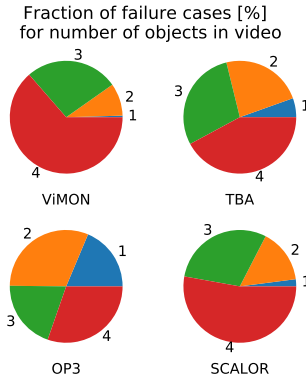

Figure E.2: Distribution of failure cases dependent on number of objects in VMDS videos for each model. Mean of three training runs.

Results are shown as the mean and standard deviation of three training runs with different random seed per model.

E.1 Out-of-distribution test sets

To test whether the models can in principle learn additional object transformations as featured in the VMDS o.o.d. sets, we additionally train the models on a new training set that includes size and color changes as well as rotation of objects.

ViMON, OP3 and SCALOR are able to learn additional property changes of the objects when they are part of the training data while TBA fails to learn tracking on this more challenging data set (Fig. E.3; for absolute values Table E.4).

E.2 Stability of training and runtime

To assess runtime in a fair way despite the models being trained on different hardware, we report the training progress of all models after one hour of training on a single GPU
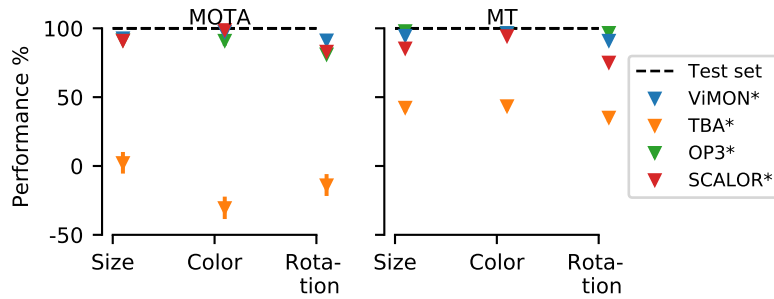
Figure E.3: Performance on out-of-distribution sets relative to VMDS test set (100%). * indicates that models were trained on a data set that included color, size and orientation changes of objects.
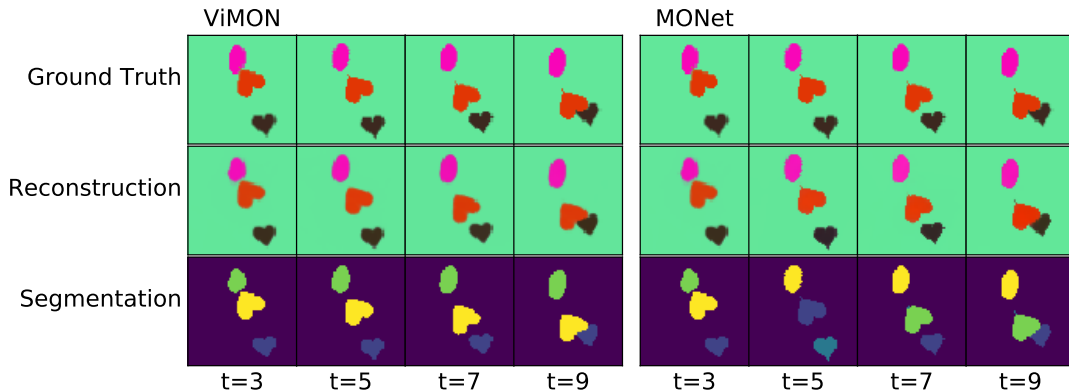
Figure E.4: Comparison of MONet and ViMON on VMDS. Example sequence of data set shown with corresponding outputs of the model. Reconstruction shows sum of components from all slots, weighted by the attention masks. Color-coded segmentation maps in third row signify slot-assignment. Note how the object-slot assignment changes for consecutive frames (3rd row) for MONet, while ViMON maintains a consistent slot assignment throughout the video.

(Table E.5). In addition, we quantify inference time on the full VMDS test set using a batch size of one.

E.3 ViMON Ablations

Removing the GRU or the mask conditioning of the attention network reduces tracking performance (MOTA on VMDS from 86.8% to 70.6% and 81.4%, respectively; Table E.6)

E.4 Impact of IoU Threshold for Matching

To examine whether the IoU threshold used for matching object predictions to ground truth impacts the ordering of the models, we compute all metrics with regard to the thresholds [0.1 .. 0.9] in steps of 0.1 on the VMDS test set. The ordering of the models with regard

	Occlusion			Same Color			Small Objects			Large Objects		
Model	MOTA	MOTP	MT	MOTA	MOTP	MT	MOTA	MOTP	MT	MOTA	MOTP	MT
VɪMON	67.1 ± 0.4	82.5 ± 0.0	63.0 ± 0.1	72.2 ± 0.1	83.6 ± 0.1	70.4 ± 0.3	86.3 ± 0.2	83.3 ± 0.2	83.4 ± 0.4	70.7 ± 0.5	85.1 ± 0.1	76.1 ± 0.7
TBA	37.5 ± 10.4	72.8 ± 0.8	38.3 ± 4.6	47.2 ± 9.4	73.0 ± 0.7	45.2 ± 3.9	74.3 ± 0.7	71.9 ± 0.4	65.3 ± 1.6	25.6 ± 15.0	73.4 ± 0.9	44.7 ± 6.7
OP3	85.3 ± 1.0	91.6 ± 0.4	89.6 ± 0.9	51.5 ± 1.3	86.5 ± 0.3	66.3 ± 1.3	93.3 ± 1.6	93.0 ± 0.4	97.0 ± 0.2	83.8 ± 2.0	92.2 ± 0.4	93.5 ± 0.4
SCALOR	58.8 ± 1.0	86.6 ± 0.4	46.8 ± 1.2	53.7 ± 1.1	83.4 ± 0.3	46.2 ± 1.1	74.4 ± 0.7	86.1 ± 0.4	67.6 ± 1.3	66.1 ± 1.9	86.6 ± 0.5	62.4 ± 1.4

Table E.3: Performance on **VMDS challenge sets**. Results shown as mean ± standard deviation for three runs with different random training seeds. Examples sequences for each challenge set shown below.

	Size				Color				Rotation			
Model	MOTA	MOTP	MD	MT	MOTA	MOTP	MD	MT	MOTA	MOTP	MD	MT
VɪMON	61.4 ± 2.5	78.0 ± 0.3	71.3 ± 2.1	66.8 ± 1.9	87.4 ± 0.4	86.2 ± 0.2	86.4 ± 0.1	85.0 ± 0.2	-10.4 ± 4.0	70.5 ± 0.4	39.5 ± 2.6	29.8 ± 1.0
VɪMON*	80.3 ± 0.9	82.1 ± 0.5	82.5 ± 0.4	79.8 ± 0.5	84.5 ± 0.6	84.6 ± 0.5	83.4 ± 0.5	81.8 ± 0.3	78.7 ± 1.6	82.0 ± 0.6	79.2 ± 0.4	76.4 ± 0.6
TBA	52.3 ± 8.7	73.3 ± 0.7	59.8 ± 4.9	51.8 ± 4.9	56.1 ± 11.4	75.1 ± 0.9	63.7 ± 5.4	59.0 ± 5.2	52.4 ± 9.9	73.6 ± 0.8	59.3 ± 6.2	49.8 ± 5.5
TBA*	1.3 ± 7.8	68.4 ± 1.9	30.6 ± 4.5	24.8 ± 3.4	-16.5 ± 8.1	69.6 ± 1.5	29.1 ± 3.8	25.4 ± 3.3	-7.5 ± 7.9	69.4 ± 1.4	26.6 ± 4.0	20.6 ± 3.4
OP3	87.0 ± 1.9	90.8 ± 0.4	96.4 ± 0.1	95.3 ± 0.1	90.8 ± 1.2	93.5 ± 0.5	97.3 ± 0.1	95.8 ± 0.1	54.7 ± 5.7	84.2 ± 0.7	87.1 ± 1.7	80.5 ± 2.5
OP3*	84.0 ± 2.8	91.2 ± 1.0	95.9 ± 0.8	94.5 ± 1.2	83.6 ± 3.7	91.6 ± 1.3	95.5 ± 0.5	92.9 ± 1.6	74.5 ± 2.2	89.8 ± 0.7	94.8 ± 0.6	93.3 ± 0.8
SCALOR	68.1 ± 1.7	84.9 ± 0.4	63.3 ± 1.7	60.0 ± 2.0	75.5 ± 1.1	89.9 ± 0.5	67.0 ± 1.4	65.7 ± 1.6	46.5 ± 1.8	82.1 ± 0.5	41.9 ± 1.7	37.1 ± 1.3
SCALOR*	67.5 ± 1.2	85.2 ± 0.6	61.2 ± 1.2	57.1 ± 0.7	73.3 ± 0.7	89.8 ± 0.5	64.8 ± 1.1	63.0 ± 0.9	61.6 ± 1.4	83.5 ± 0.4	53.4 ± 1.5	50.2 ± 1.1

* Models trained on a data set that featured color, size and orientation changes of objects during the sequence.

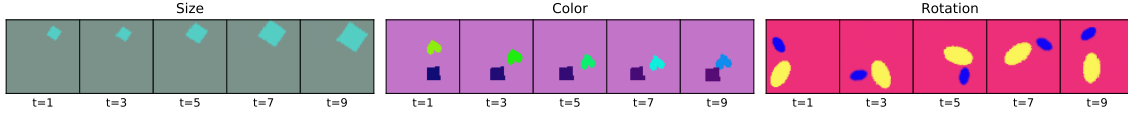Table E.4: Performance on **VMDS OOD test sets**. Results shown as mean ± standard deviation for three runs with different random training seeds. Examples sequences for each o.o.d. set shown below.

to their MOTA is consistent over all matching thresholds, but the performance difference between the models increases with higher thresholds (Fig. E.6). For low thresholds (0.1 – 0.3) TBA outperforms SCALOR in MD, MT, Matches and Misses but has a significantly lower segmentation performance as measured by MOTP.
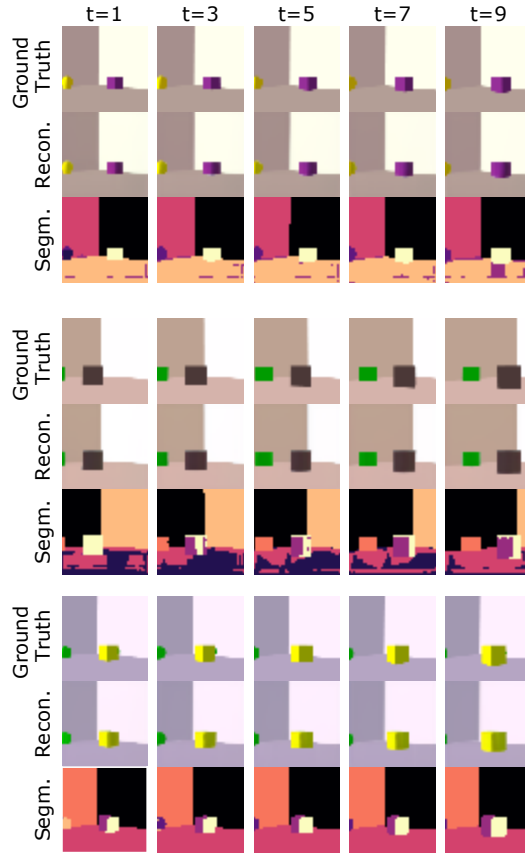
Figure E.5: Failure cases of OP3 on VOR. Example sequences of VOR test set shown with corresponding outputs of the model after final refinement step. Binarized color-coded segmentation maps in third row signify slot-assignment.
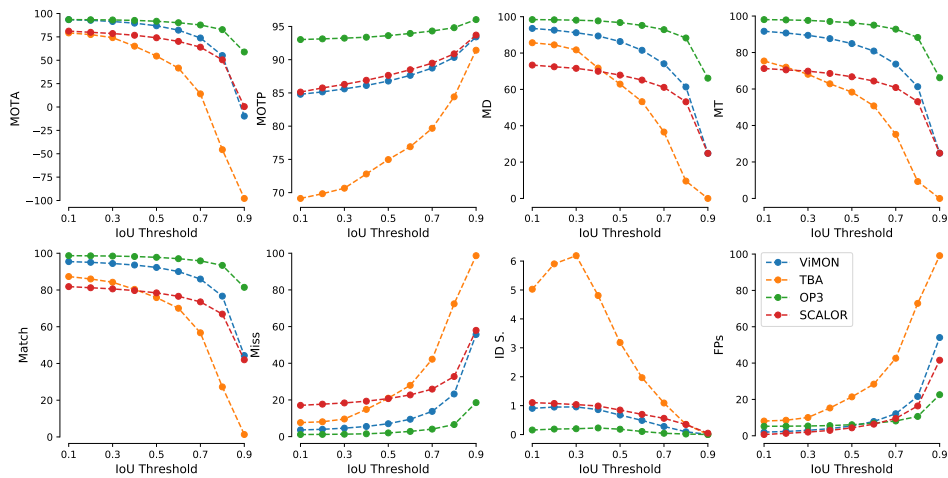

Figure E.6: Results of VIMON, TBA, OP3 and SCALOR on the VMDS test set using different IoU thresholds for matching ground truth objects to model predictions.

Model	Resolution	No. Param.	Training					Inference		
			Batch Size	Memory [MiB]	No. Iters	Epochs		Memory [MiB]	Avg. runtime / batch	Total runtime
ViMON	64×64	714,900	18	10,860	3687	6.63		910	0.28 s/it	4min 39s
TBA	128×128	3,884,644*	64	10,564	4421	28.29		972	0.24 s/it	4min 05s
OP3	64×64	876,305	10	10,874	2204	2.20		4092	0.54 s/it	9min 04s
SCALOR	64×64	2,763,526	48	10,942	2547	12.23		930	0.29 s/it	4min 48s

* The TBA parameter count scales with the feature resolution, which is kept fixed using adaptive pooling. This makes the parameter count independent of input resolution.

Table E.5: Runtime analysis (using a single RTX 2080 Ti GPU). Training: models trained on VMDS for one hour. Inference: models evaluated on VMDS test set with batch size=1 (10 frames).

Model	MOTA ↑	MOTP ↑	MD ↑	MT ↑	Match ↑	Miss ↓	ID S. ↓	FPs ↓	MSE ↓
ViMON w/o Mask conditioning	70.6	87.8	75.7	66.0	81.4	13.4	5.2	10.8	16.9
ViMON w/o GRU	81.4	86.9	79.8	77.3	88.2	10.3	1.4	6.8	18.9

Table E.6: Ablation experiments for ViMON on VMDS.

Appendix F. Supplementary Figures

See figures F.5 – F.13 for additional, randomly picked examples of reconstruction and segmentation for k-Means, ViMON, TBA, OP3 and SCALOR on the four data sets (VMDS, SpMOT, VOR and texVMDS).
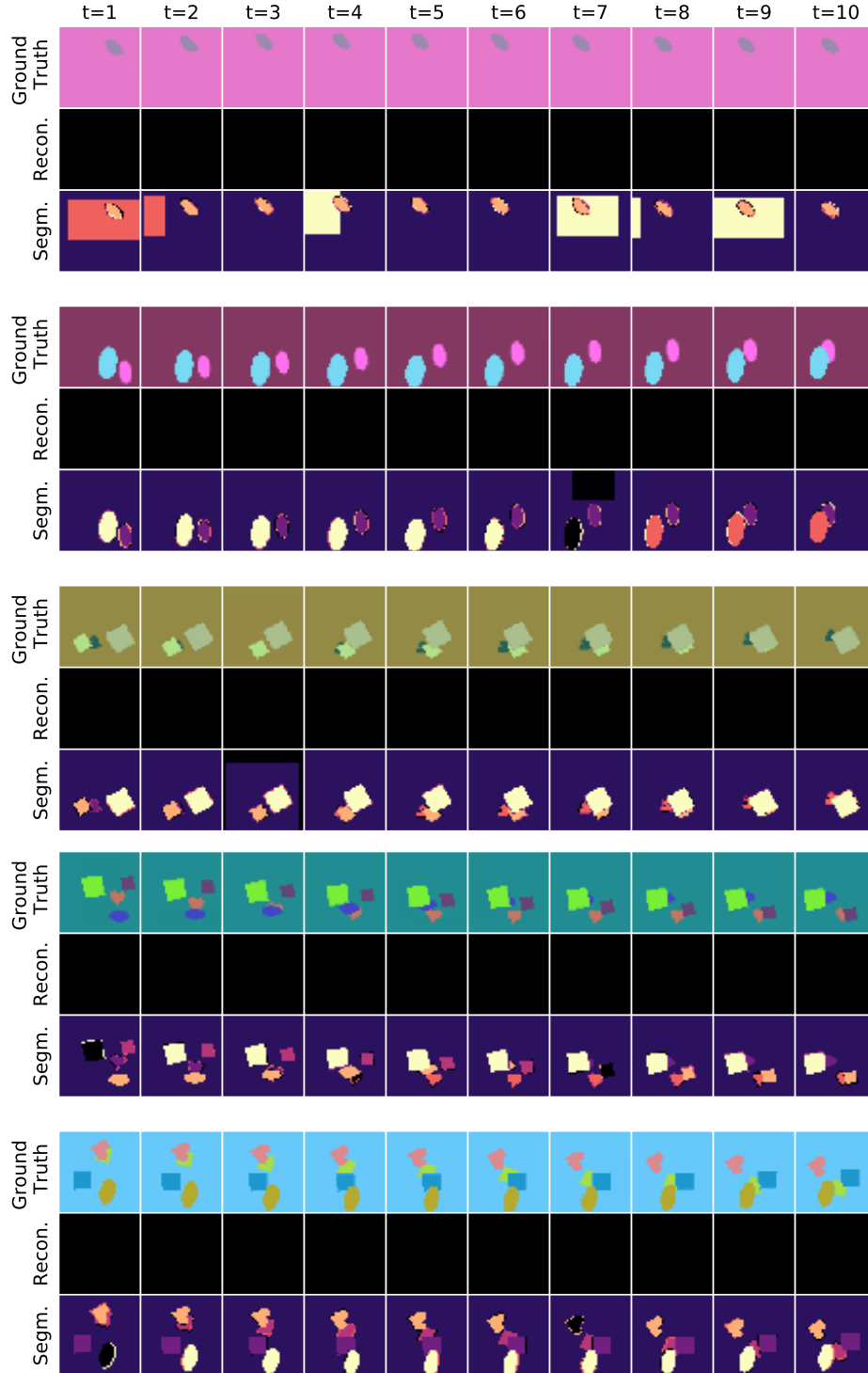
Figure F.1: Results of k-Means on VMDS. Random example sequences of VMDS test set shown with corresponding outputs of the model. Note that k-Means does not give a reconstruction of the input.
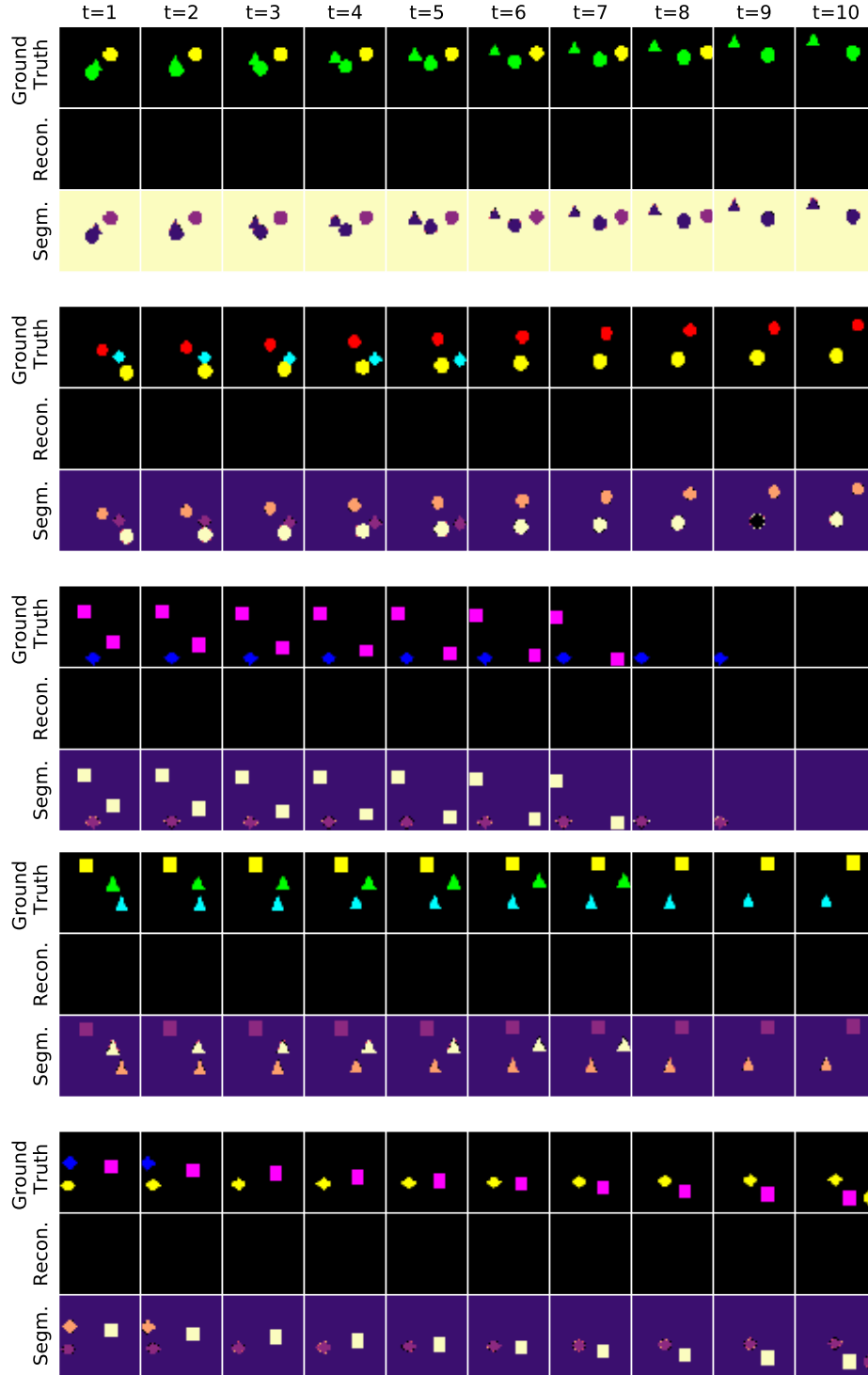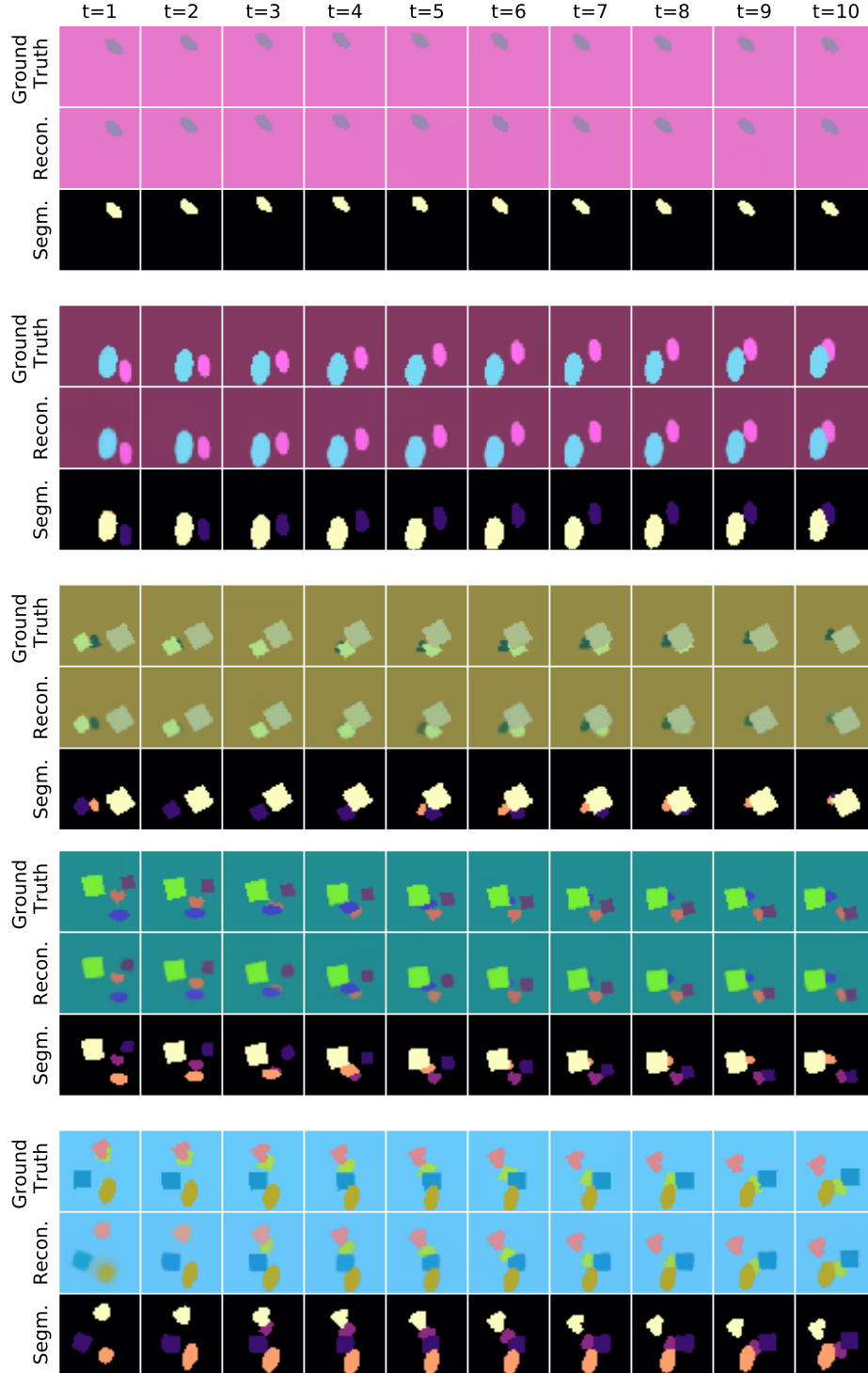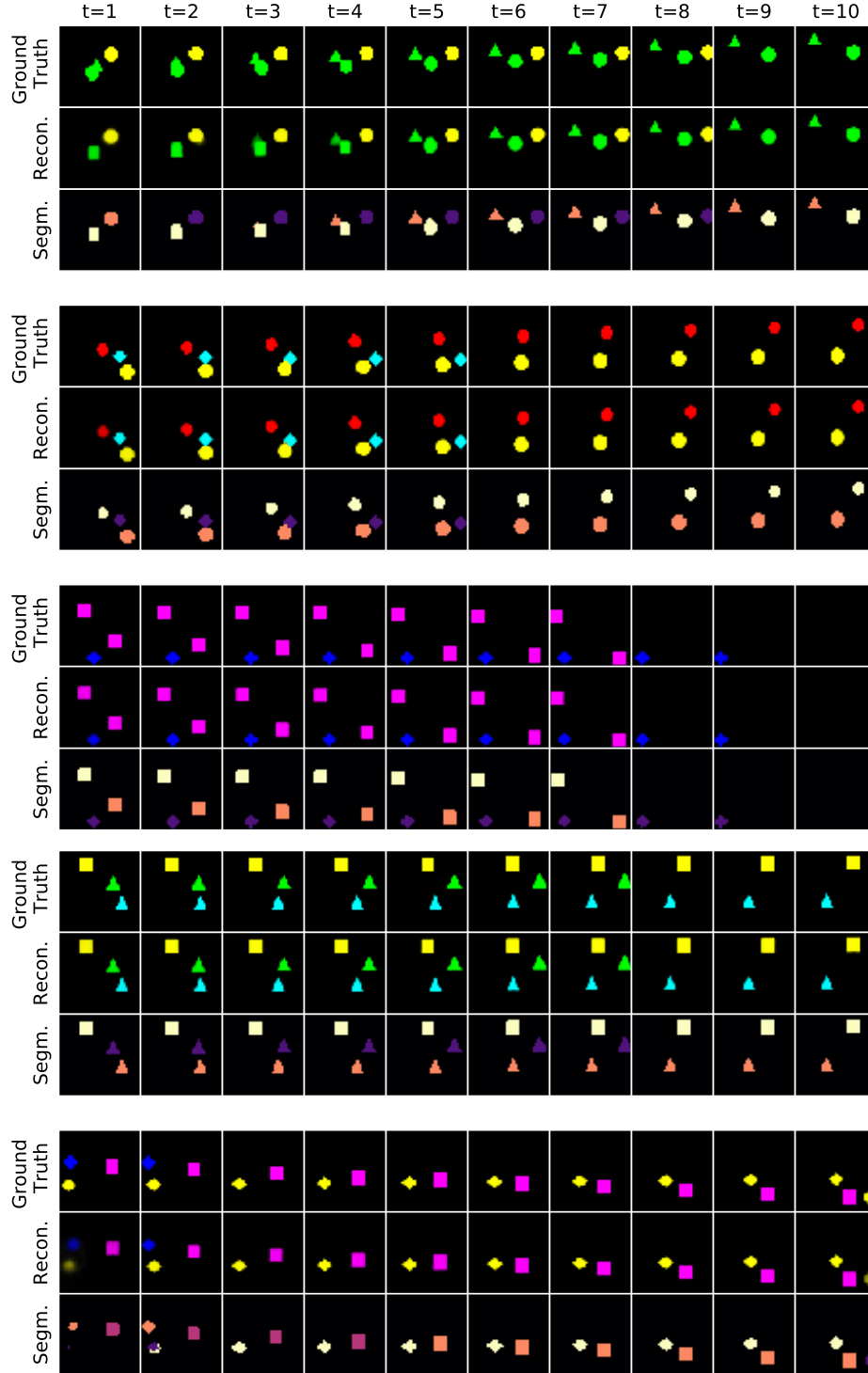
Figure F.2: Results of K-MEANS on SpMOT. Random example sequences of SpMOT test set shown with corresponding outputs of the model. Note that k-Means does not give a reconstruction of the input.
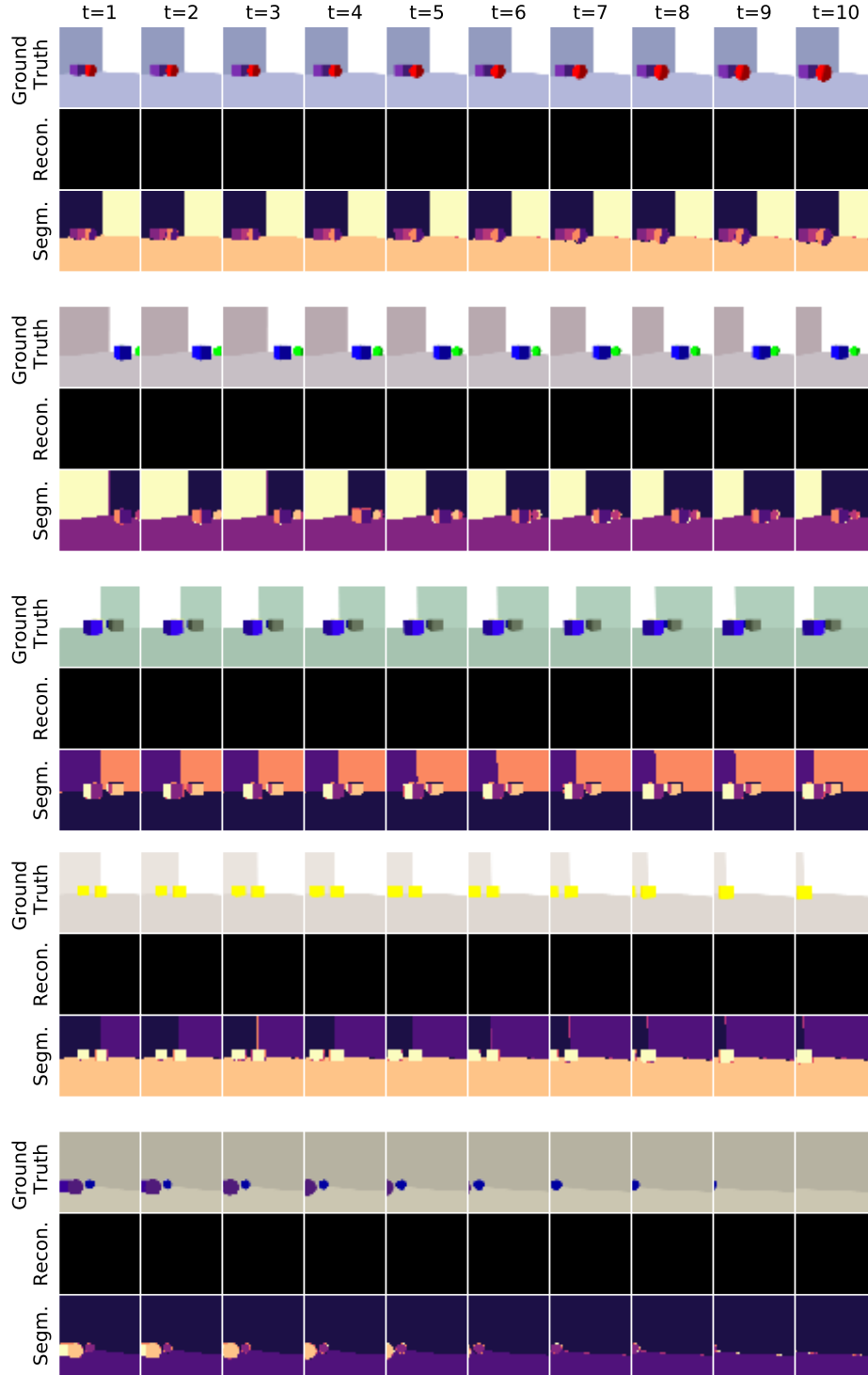
Figure F.3: Results of k-Means on VOR. Random example sequences of VOR test set shown with corresponding outputs of the model. Note that k-Means does not give a reconstruction of the input.
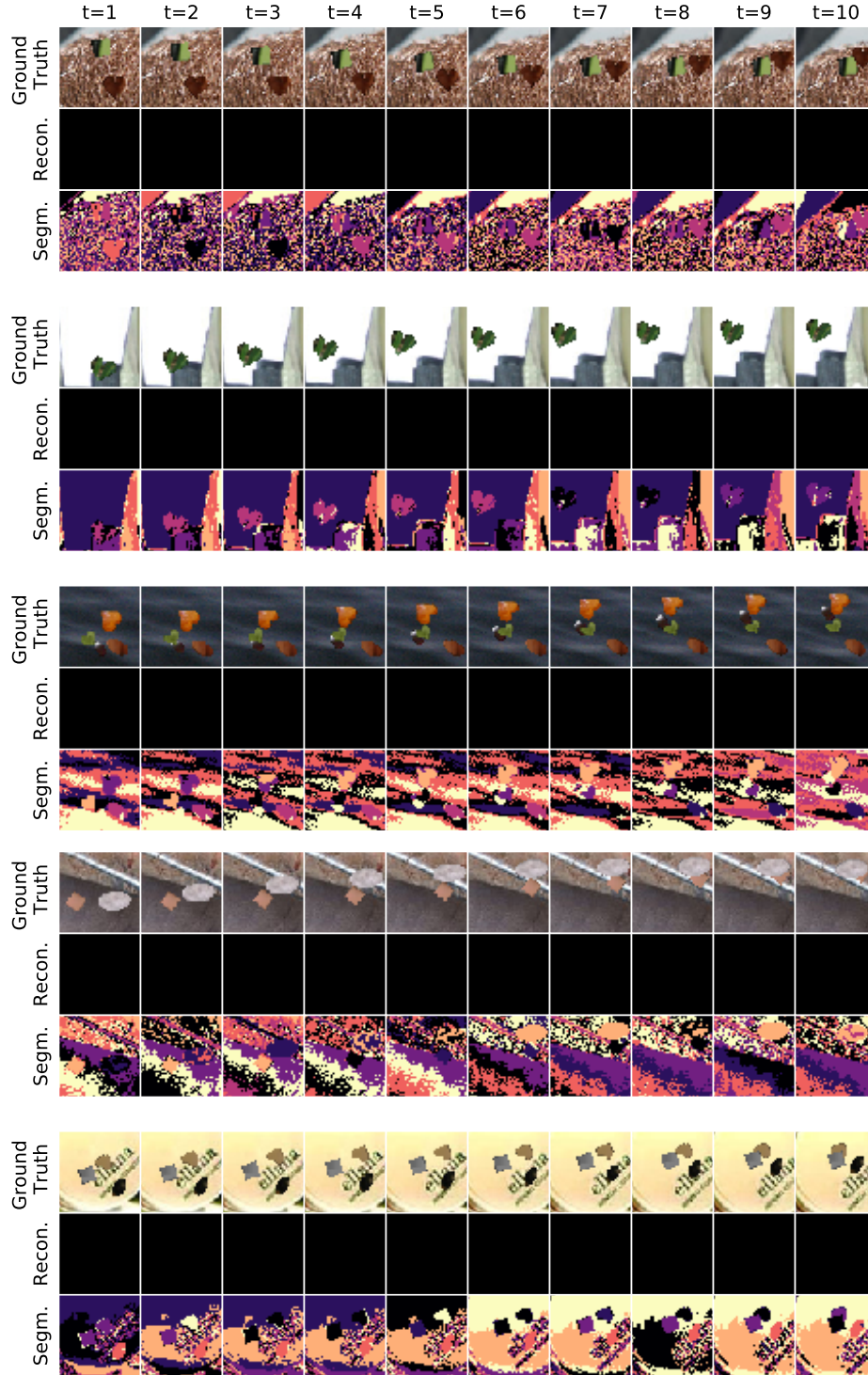
Figure F.4: Results of κ-Means on texVMDS. Random example sequences of texVMDS test set shown with corresponding outputs of the model. Note that k-Means does not give a reconstruction of the input.

Figure F.5: Results of ViMON on VMDS. Random example sequences of VMDS test set shown with corresponding outputs of the model. Reconstruction shows sum of components from all slots, weighted by the reconstructed masks from the VAE. Binarized color-coded segmentation maps in third row signify slot-assignment.
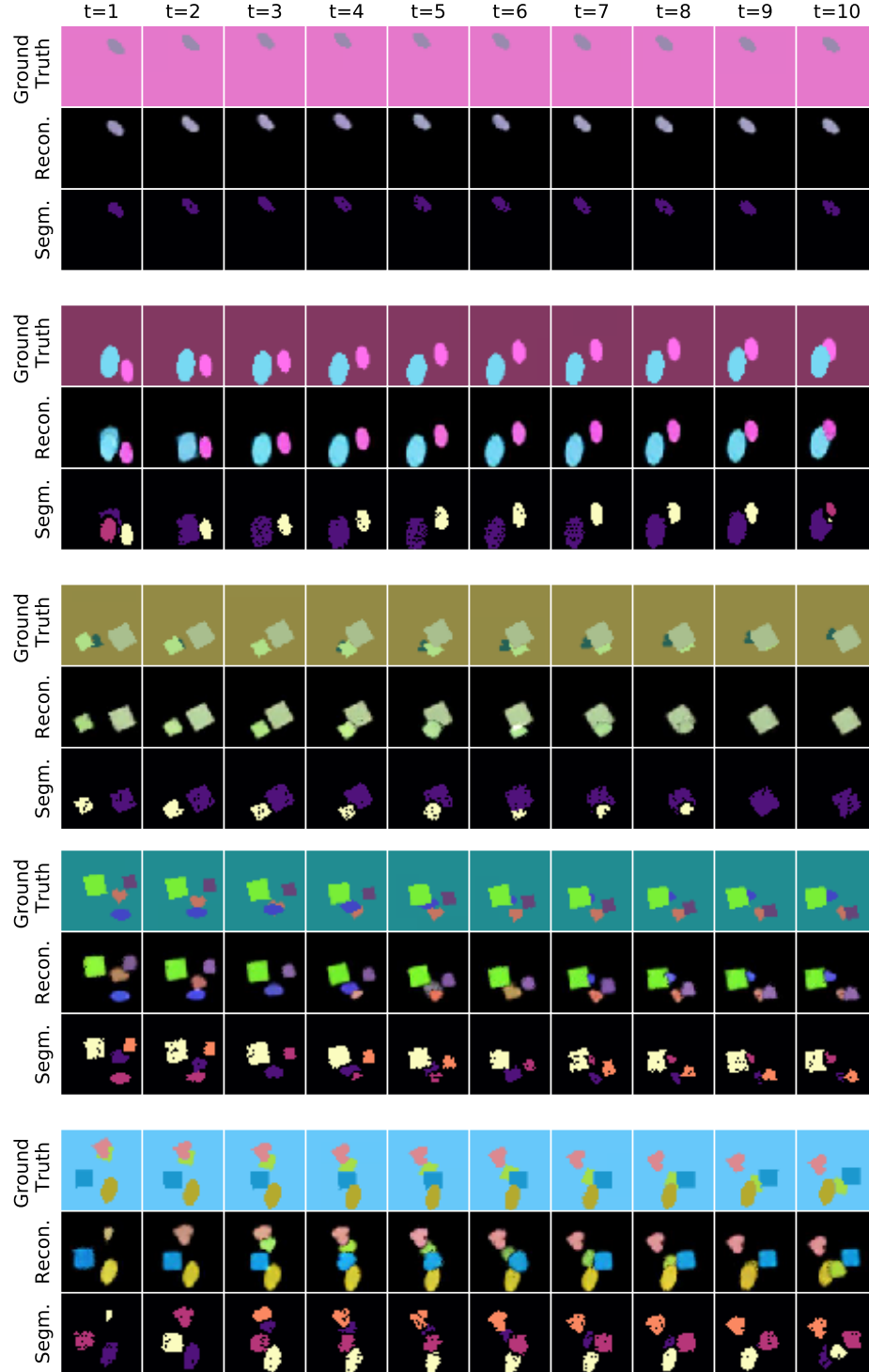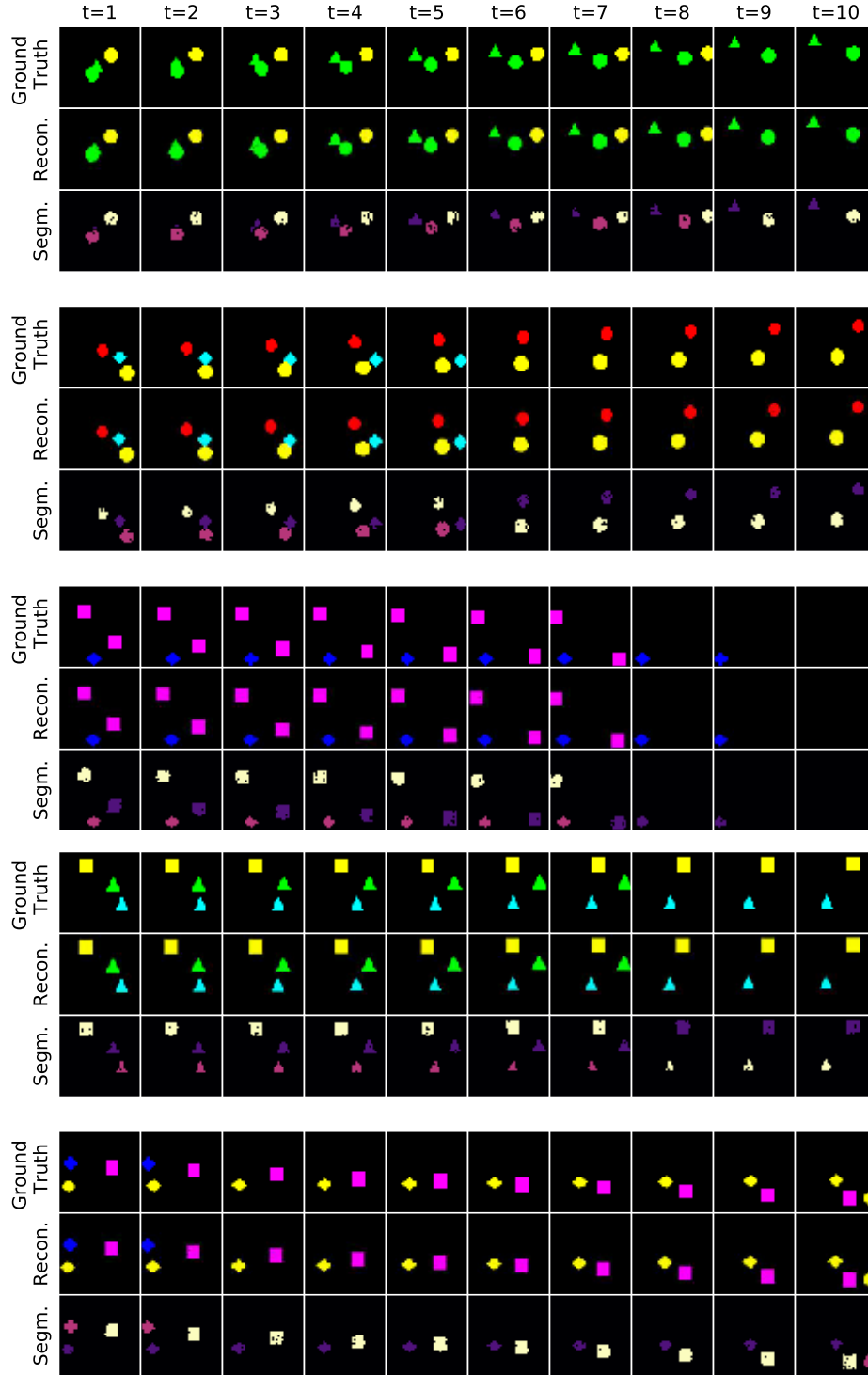
Figure F.6: Results of ViMON on SpMOT. Random example sequences of SpMOT test set shown with corresponding outputs of the model. Reconstruction shows sum of components from all slots, weighted by the reconstructed masks from the VAE. Binarized color-coded segmentation maps in third row signify slot-assignment.
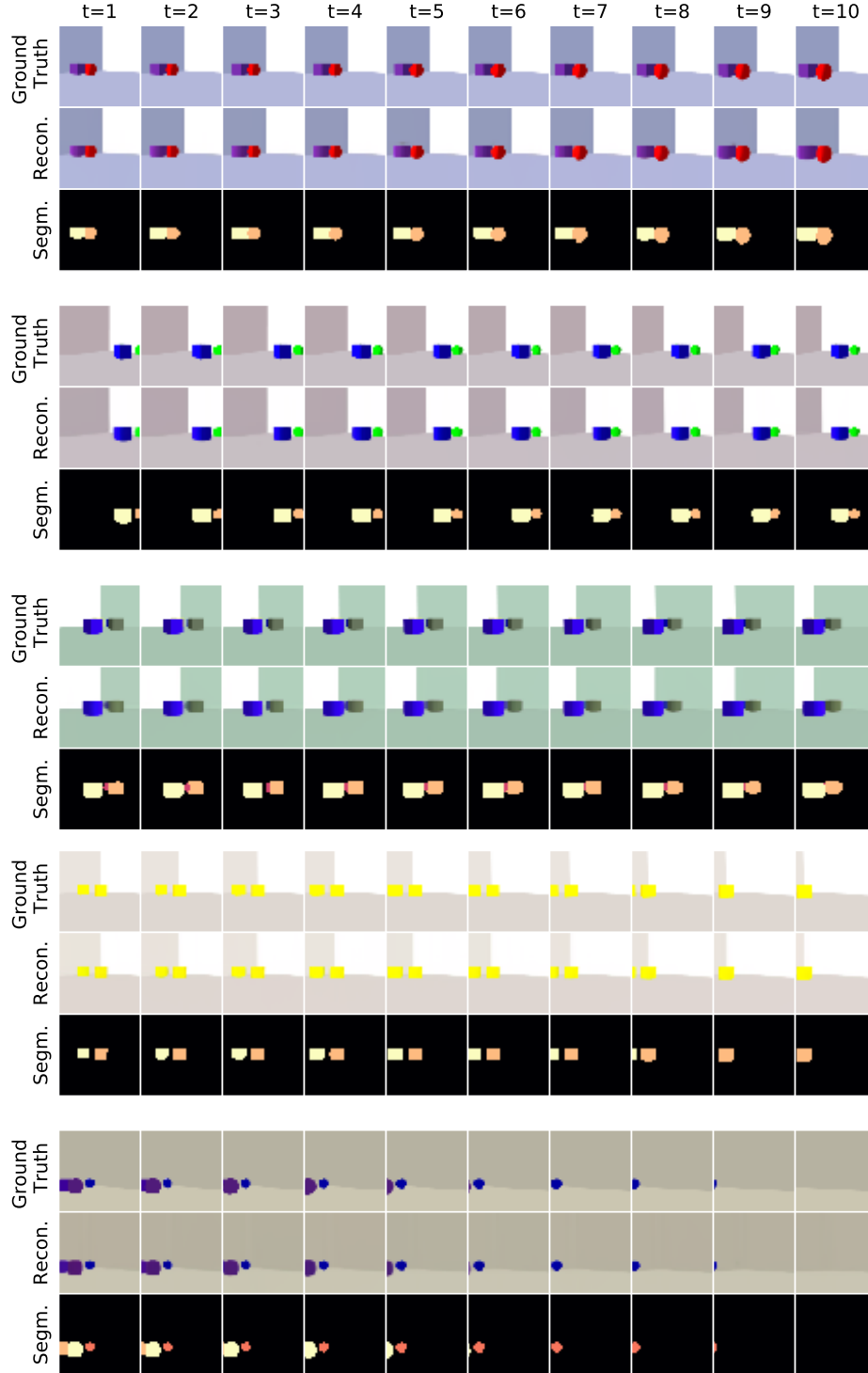
Figure F.7: Results of ViMON on VOR. Random example sequences of VOR test set shown with corresponding outputs of the model. Reconstruction shows sum of components from all slots, weighted by the reconstructed masks from the VAE. Binarized color-coded segmentation maps in third row signify slot-assignment.
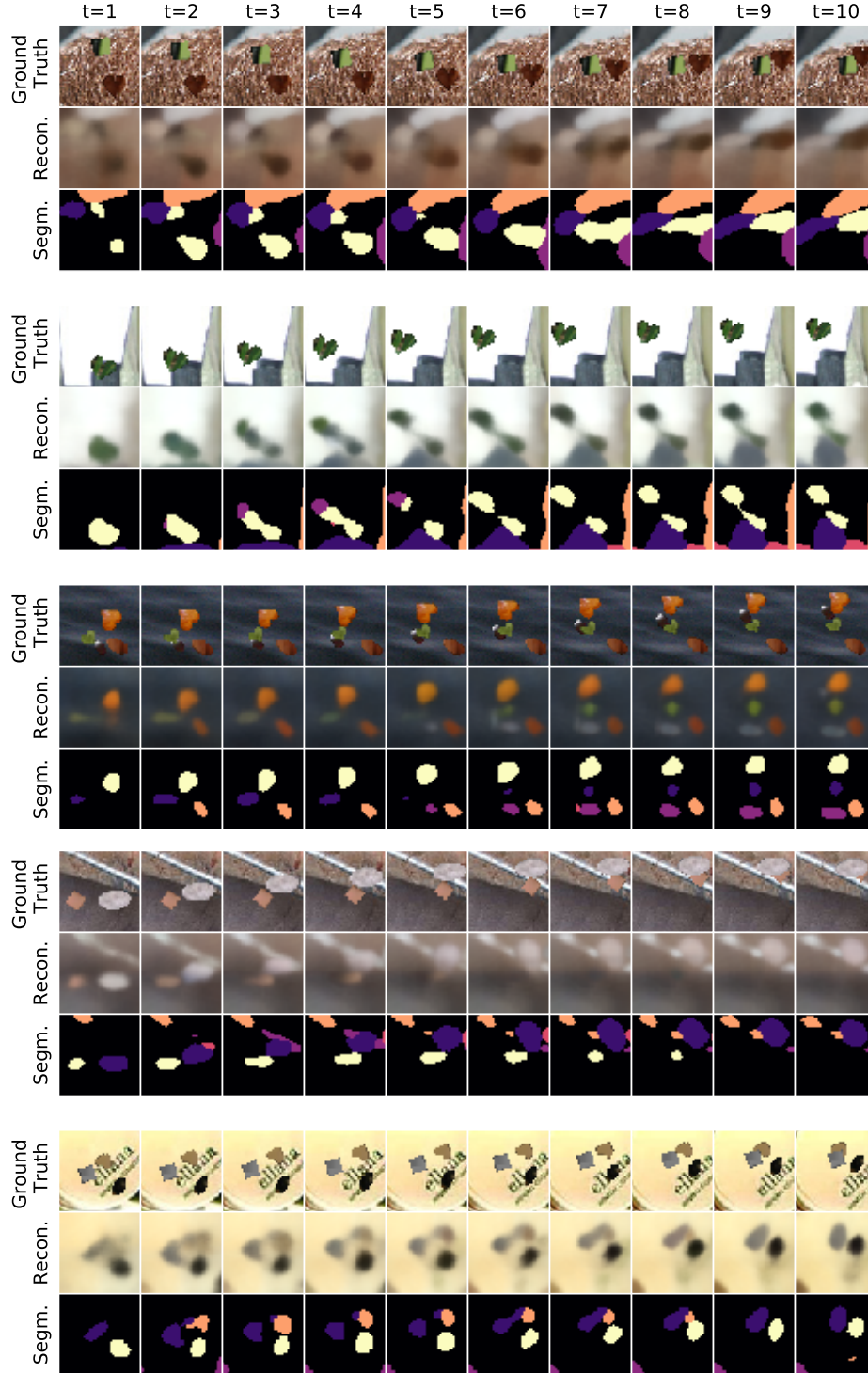
Figure F.8: Results of ViMON on texVMDS. Random example sequences of texVMDS test set shown with corresponding outputs of the model. Reconstruction shows sum of components from all slots, weighted by the reconstructed masks from the VAE. Binarized color-coded segmentation maps in third row signify slot-assignment.

Figure F.9: Results of TBA on VMDS. Random example sequences of VMDS test set shown with corresponding outputs of the model. Binarized color-c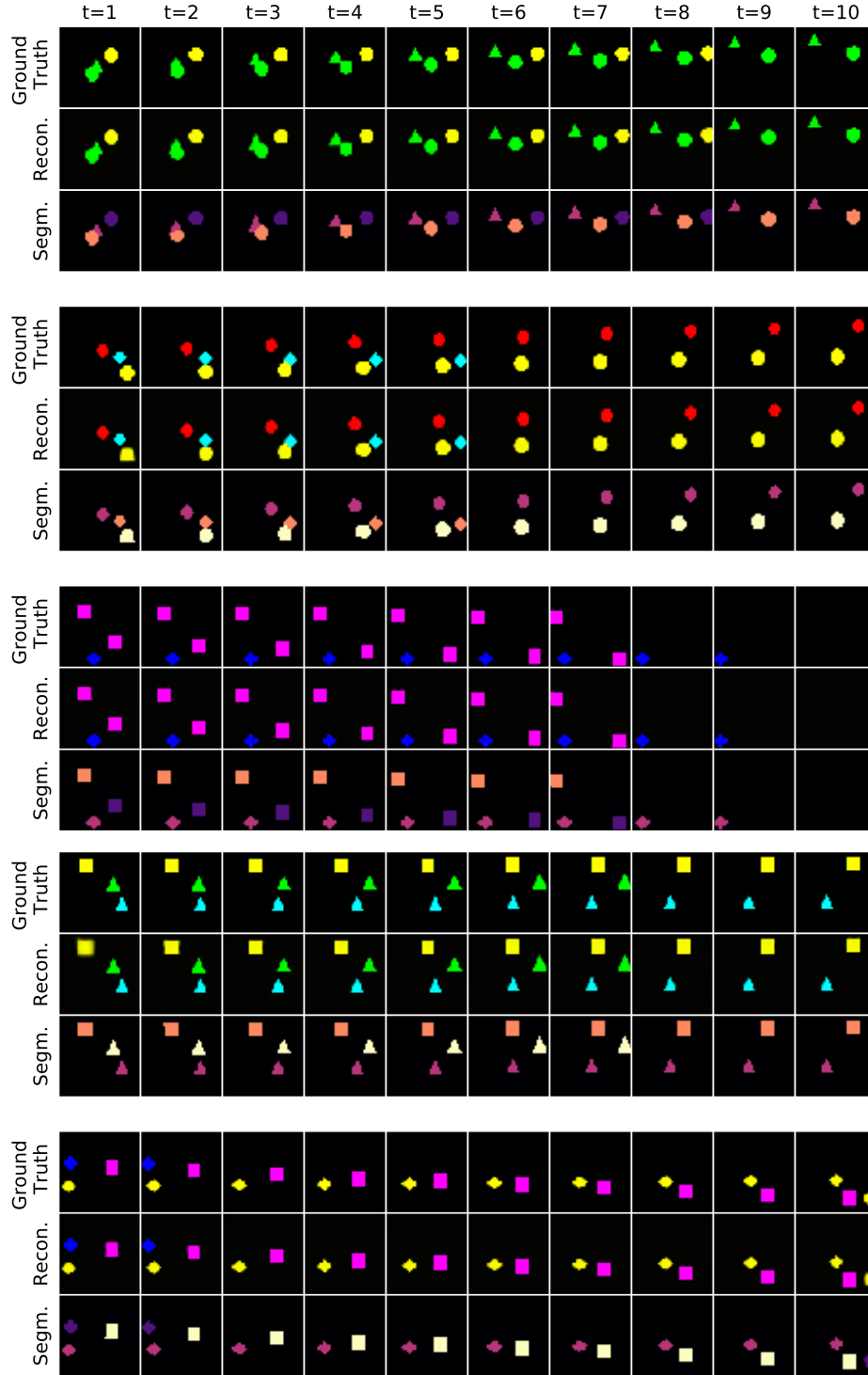oded segmentation maps in third row signify slot-assignment. Note that background subtraction is performed in the preprocessing of TBA, hence the black background in the reconstructions.

Figure F.10: Results of TBA on SpMOT. Random example sequences of SpMOT test set shown with corresponding outputs of the model. Binarized color-coded segmentation maps in third row signify slot-assignment.
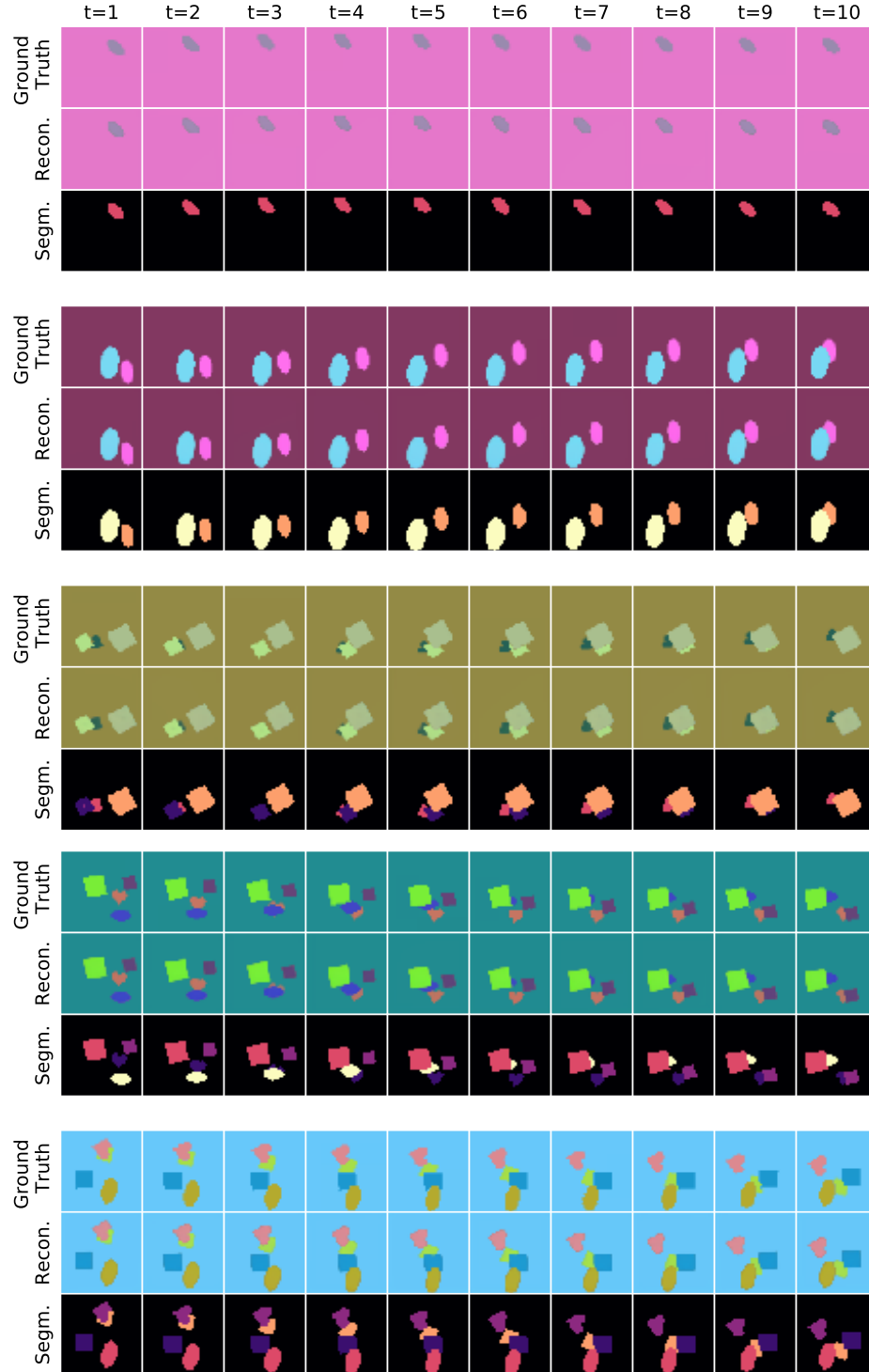
Figure F.11: Results of OP3 on VMDS. Random example sequences of VMDS test set shown with corresponding outputs of the model after final refinement step. Binarized color-coded segmentation maps in third row signify slot-assignment.
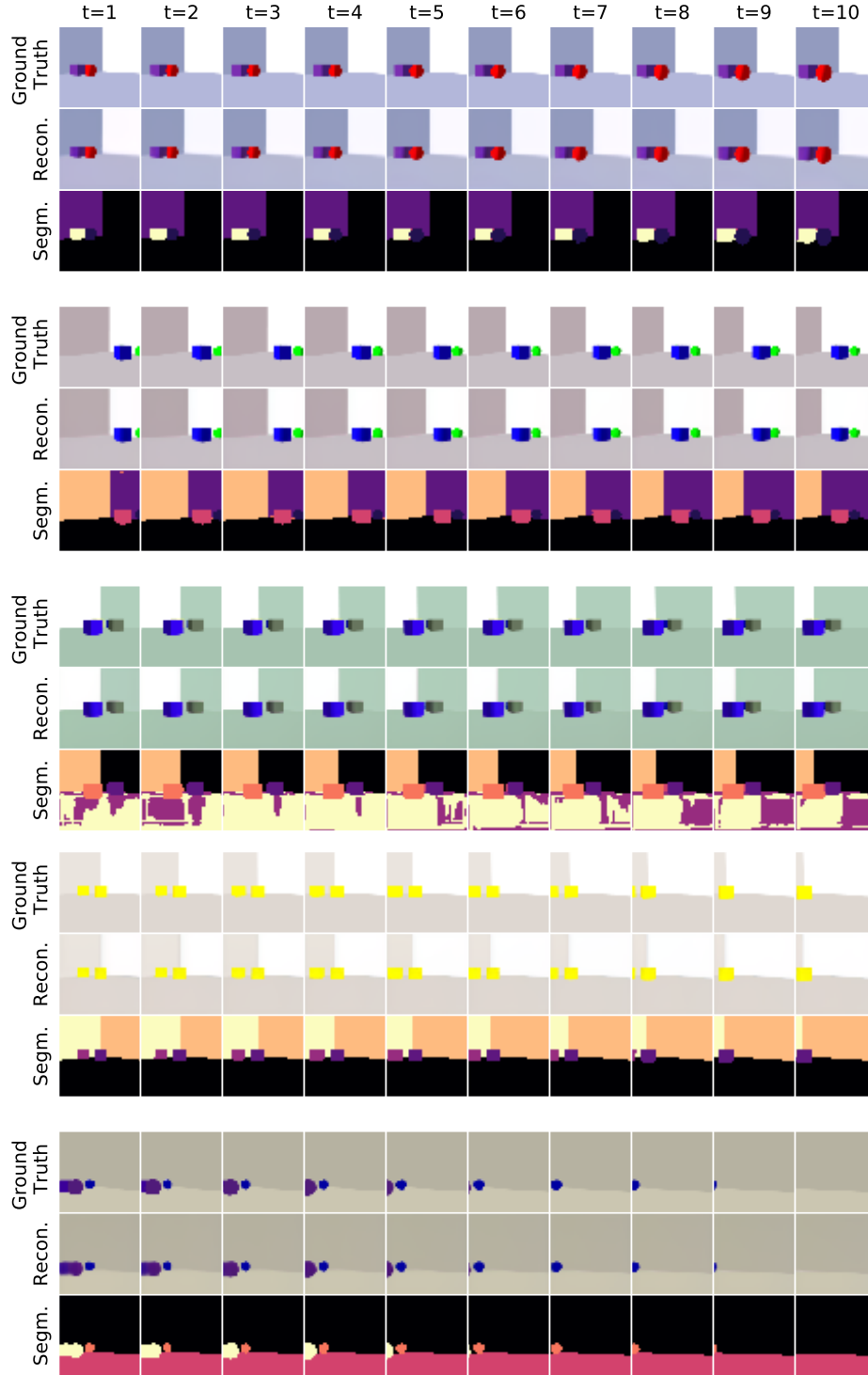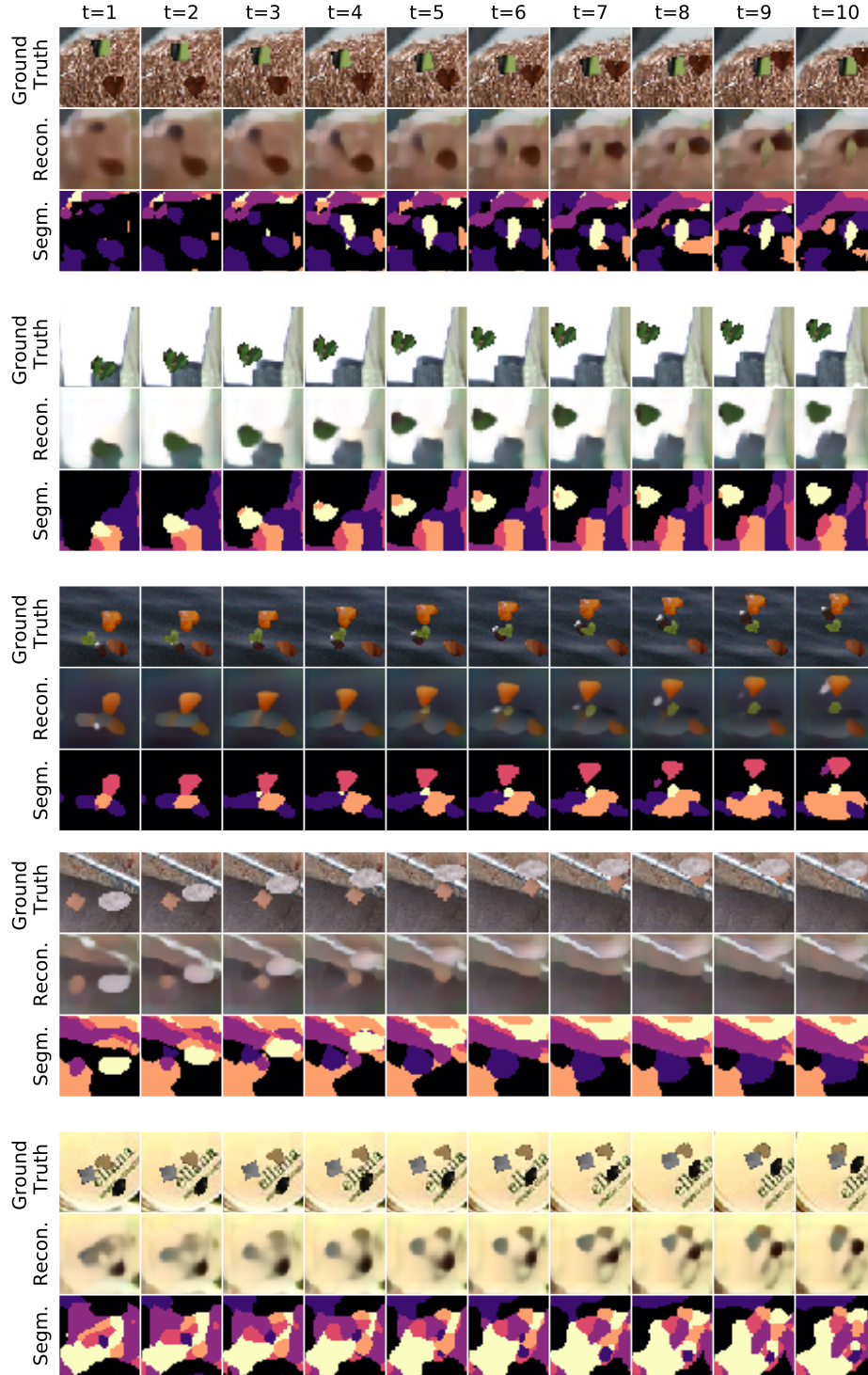
Figure F.12: Results of OP3 on SpMOT. Random example sequences of SpMOT test set shown with corresponding outputs of the model after final refinement step. Binarized color-coded segmentation maps in third row signify slot-assignment.

Figure F.13: Results of OP3 on VOR. Random example sequences of VOR test set shown with corresponding outputs of the model after final refinement step. Binarized color-coded segmentation maps in third row signify slot-assignment.
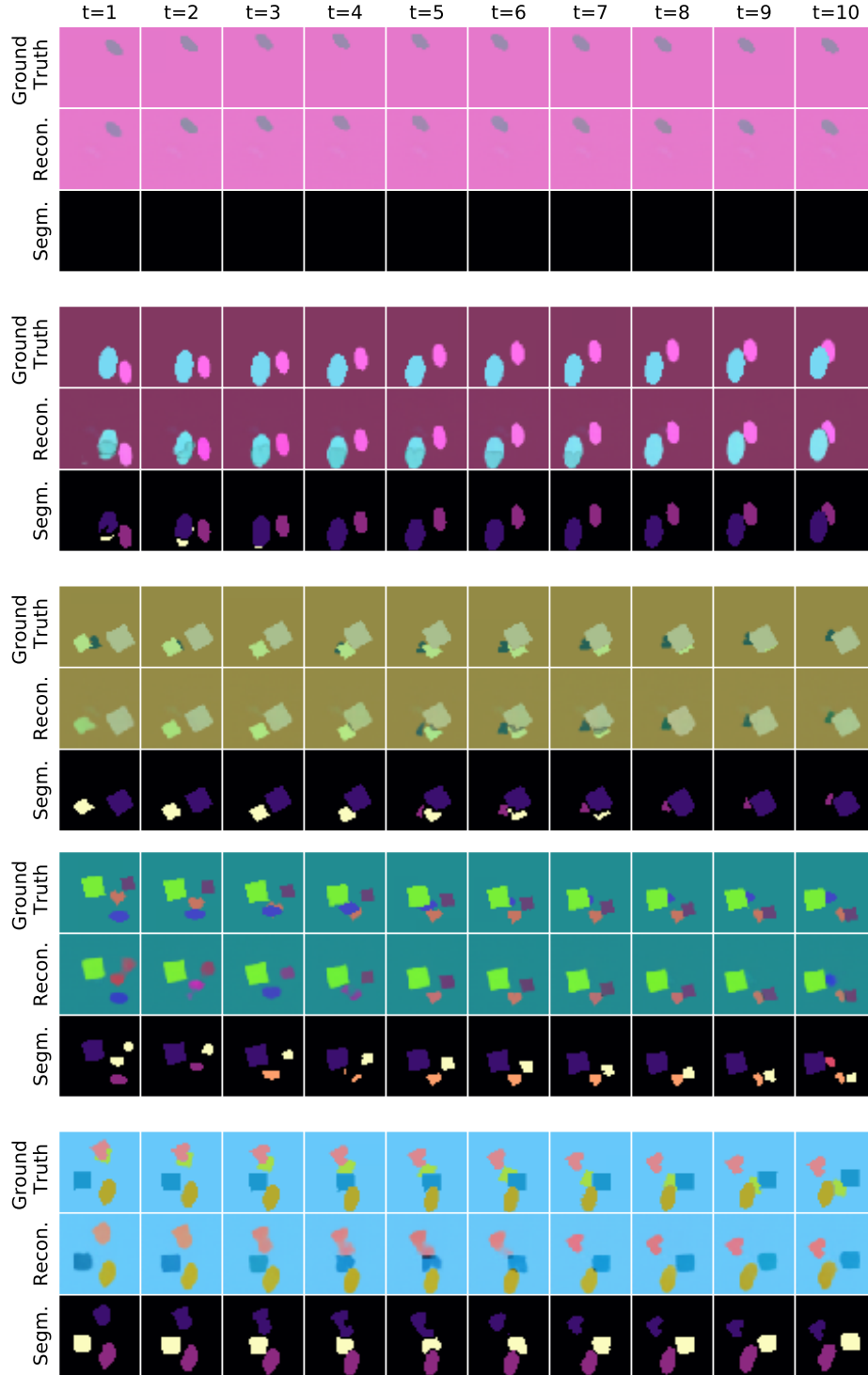
Figure F.14: Results of OP3 on texVMDS. Random example sequences of texVMDS test set shown with corresponding outputs of the model after final refinement step. Binarized color-coded segmentation maps in third row signify slot-assignment.

Figure F.15: Results of SCALOR on VMDS. Random example sequences of VMDS test set shown with corresponding outputs of the model. Binarized color-coded segmentation maps in third row signify slot-assignment.
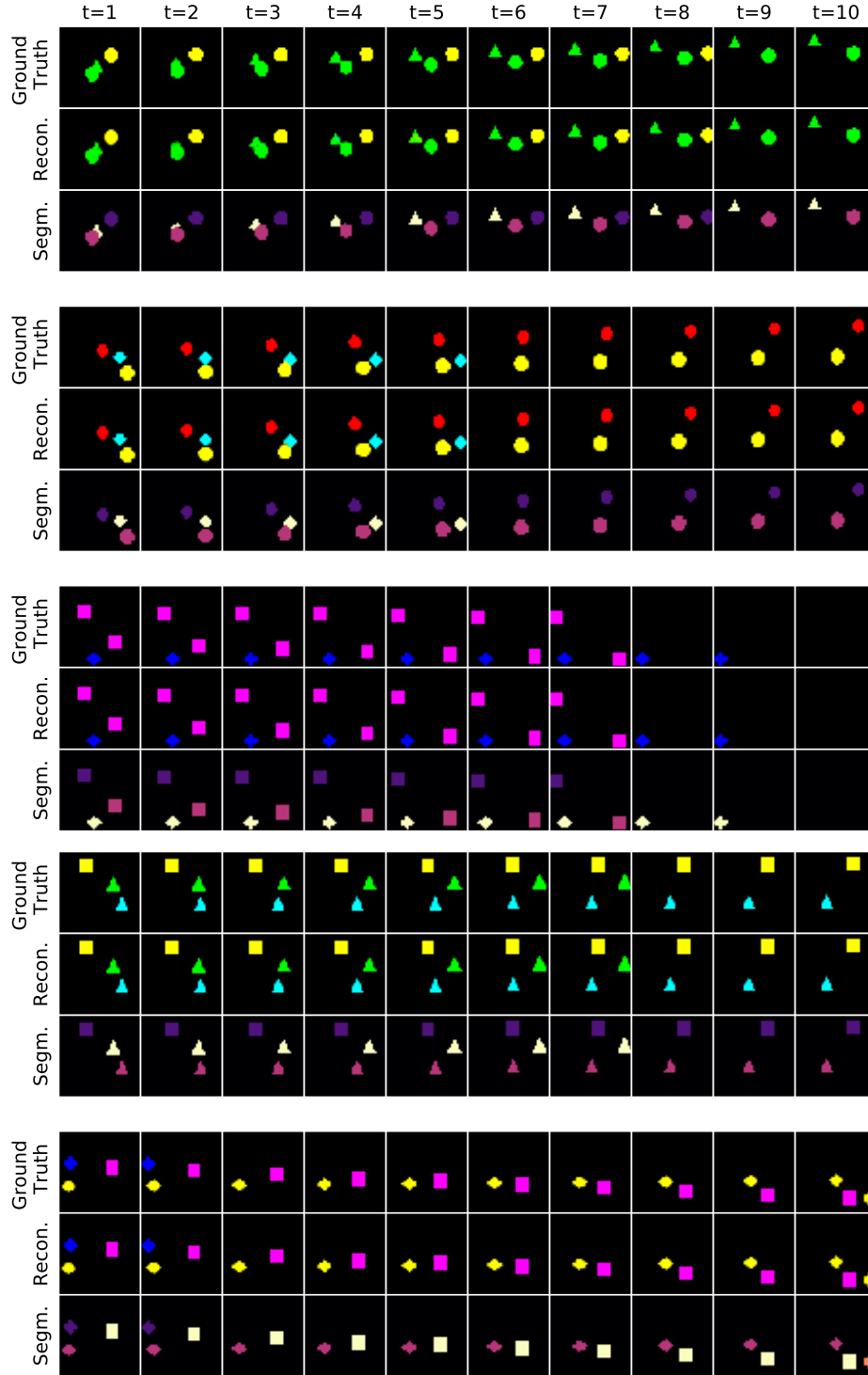
Figure F.16: Results of SCALOR on SpMOT. Random example sequences of SpMOT test set shown with corresponding outputs of the model. Binarized color-coded segmentation maps in third row signify slot-assignment.
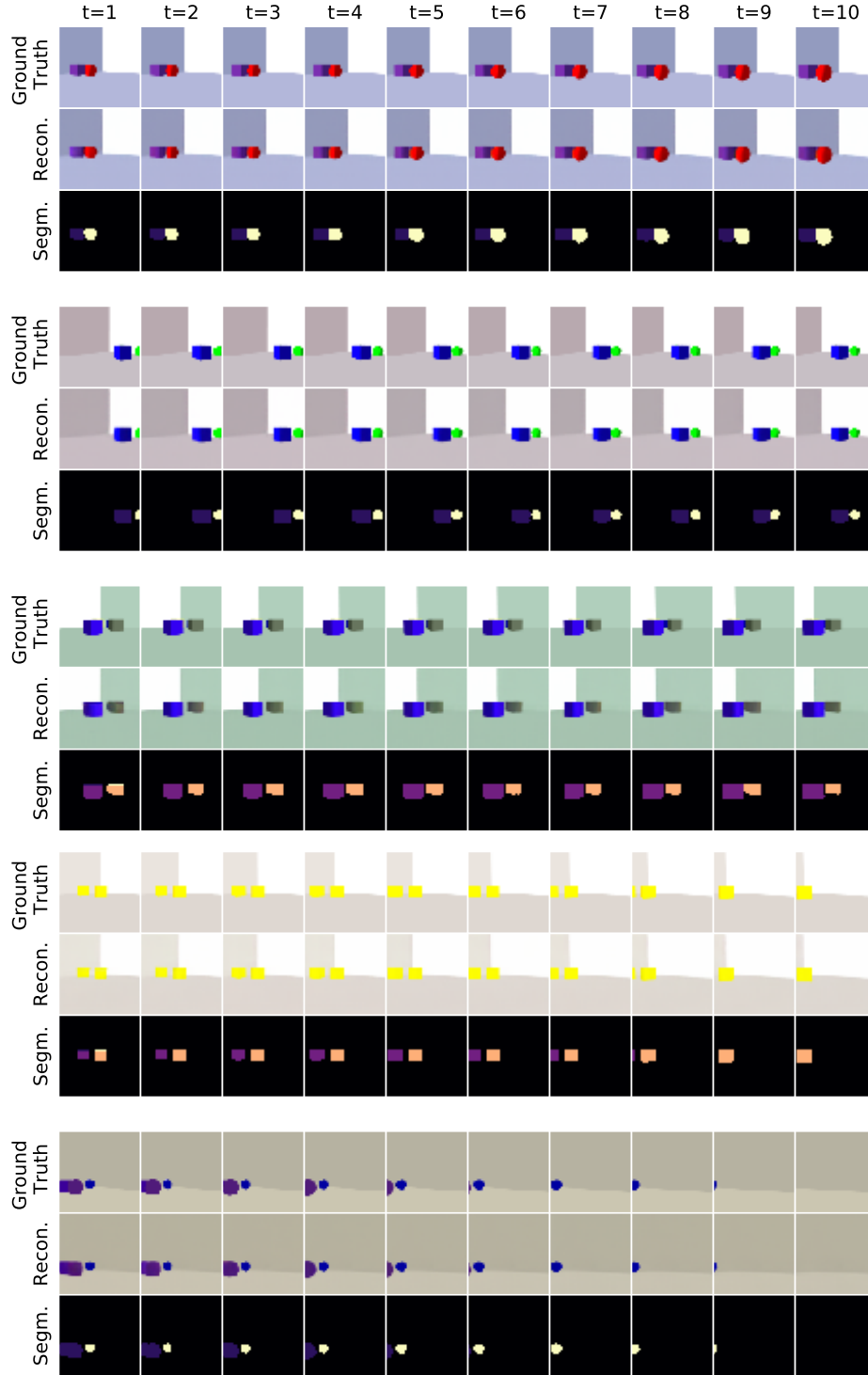
Figure F.17: Results of SCALOR on VOR. Random example sequences of VOR test set shown with corresponding outputs of the model. Binarized color-coded segmentation maps in third row signify slot-assignment.
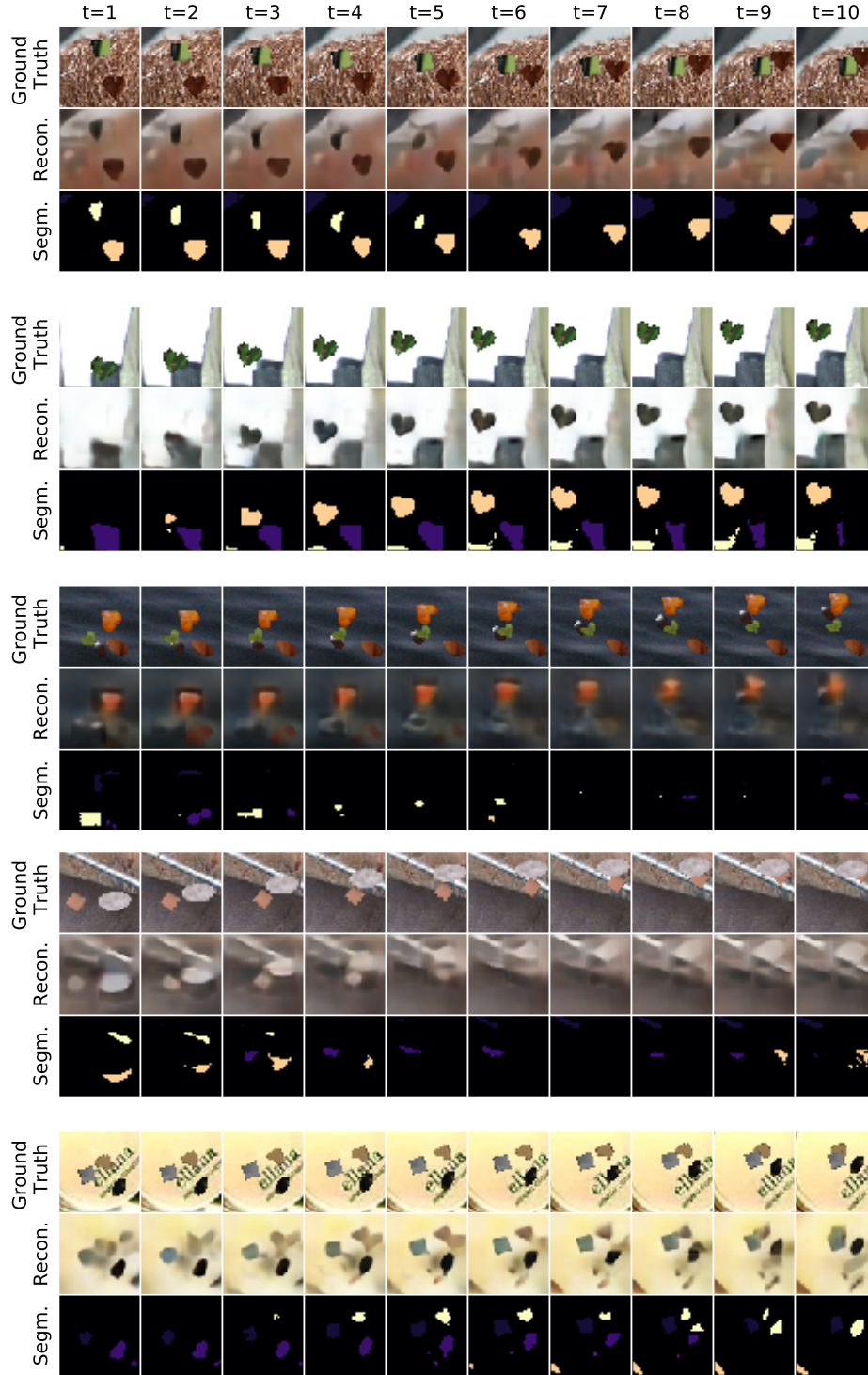
Figure F.18: Results of SCALOR on texVMDS. Random example sequences of texVMDS test set shown with corresponding outputs of the model. Binarized color-coded segmentation maps in third row signify slot-assignment.

References

Keni Bernardin and Rainer Stiefelhagen. Evaluating multiple object tracking performance: The clear mot metrics. *EURASIP Journal on Image and Video Processing*, 2008.

Domenico Daniele Bloisi and Luca Iocchi. Independent multimodal background subtraction. In *CompIMAGE*, 2012.

Christopher P. Burgess, Loïc Matthey, Nicholas Watters, Rishabh Kabra, Irina Higgins, Matthew Botvinick, and Alexander Lerchner. MONet: Unsupervised scene decomposition and representation. *arXiv.org*, 1901.11390, 2019.

Kyunghyun Cho, Bart van Merriënboer, Caglar Gulcehre, Dzmitry Bahdanau, Fethi Bougares, Holger Schwenk, and Yoshua Bengio. Learning phrase representations using RNN encoder–decoder for statistical machine translation. In *Proceedings of the 2014 Conference on Empirical Methods in Natural Language Processing (EMNLP)*, pages 1724–1734, 2014. doi: 10.3115/v1/D14-1179.

Eric Crawford and Joelle Pineau. Spatially invariant unsupervised object detection with convolutional neural networks. *Proc. of the Conf. on Artificial Intelligence (AAAI)*, 2019.

Antonia Creswell, Kyriacos Nikiforou, Oriol Vinyals, Andre Saraiva, Rishabh Kabra, Loic Matthey, Chris Burgess, Malcolm Reynolds, Richard Tanburn, Marta Garnelo, and Murray Shanahan. Alignnet: Unsupervised entity alignment. *arXiv.org*, 2007.08973, 2020.

Jia Deng, Wei Dong, Richard Socher, Li-Jia Li, Kai Li, and Li Fei-Fei. Imagenet: A large-scale hierarchical image database. In *Proc. IEEE Conf. on Computer Vision and Pattern Recognition (CVPR)*, 2009.

Sebastien Ehrhardt, Oliver Groth, Aron Monszpart, Martin Engelcke, Ingmar Posner, Niloy Mitra, and Andrea Vedaldi. Relate: Physically plausible multi-object scene synthesis using structured latent spaces. In *Advances in Neural Information Processing Systems (NeurIPS)*, volume 33, 2020.

Martin Engelcke, Adam R. Kosiorek, Oiwi Parker Jones, and Ingmar Posner. Genesis: Generative scene inference and sampling with object-centric latent representations. In *Proc. of the International Conf. on Learning Representations (ICLR)*, 2020.

S. M. Ali Eslami, Nicolas Heess, Theophane Weber, Yuval Tassa, David Szepesvari, Koray Kavukcuoglu, and Geoffrey E Hinton. Attend, infer, repeat: Fast scene understanding with generative models. In *Advances in Neural Information Processing Systems (NeurIPS)*, 2016.

Leon A. Gatys, Alexander S. Ecker, and Matthias Bethge. A neural algorithm of artistic style. *arXiv.org*, 1508.06576, 2015.

Klaus Greff, Antti Rasmus, Mathias Berglund, Tele Hao, Harri Valpola, and Jürgen Schmidhuber. Tagger: Deep unsupervised perceptual grouping. In *Advances in Neural Information Processing Systems (NeurIPS)*. 2016.

Klaus Greff, Sjoerd van Steenkiste, and Jürgen Schmidhuber. Neural expectation maximization. In *Advances in Neural Information Processing Systems (NeurIPS)*. 2017.

Klaus Greff, Raphaël Lopez Kaufman, Rishabh Kabra, Nick Watters, Christopher Burgess, Daniel Zoran, Loic Matthey, Matthew Botvinick, and Alexander Lerchner. Multi-object representation learning with iterative variational inference. In *Proc. of the International Conf. on Machine learning (ICML)*, 2019.

Klaus Greff, Sjoerd van Steenkiste, and Jürgen Schmidhuber. On the binding problem in artificial neural networks. *arXiv.org*, 2012.05208, 2020.

Zhen He, Jian Li, Daxue Liu, Hangen He, and David Barber. Tracking by animation: Unsupervised learning of multi-object attentive trackers. In *Proc. IEEE Conf. on Computer Vision and Pattern Recognition (CVPR)*, 2019.

Paul Henderson and Christoph H. Lampert. Unsupervised object-centric video generation and decomposition in 3D. In *Advances in Neural Information Processing Systems (NeurIPS) 33*, 2020.

Sepp Hochreiter and Jürgen Schmidhuber. Long short-term memory. *Neural Computation*, 9 (8):1735–1780, 1997. ISSN 0899-7667. doi: 10.1162/neco.1997.9.8.1735.

X. Hou, L. Shen, K. Sun, and G. Qiu. Deep feature consistent variational autoencoder. In *2017 IEEE Winter Conference on Applications of Computer Vision (WACV)*, pages 1133–1141, 2017. doi: 10.1109/WACV.2017.131.

Max Jaderberg, Karen Simonyan, Andrew Zisserman, and Koray Kavukcuoglu. Spatial transformer networks. In *Advances in Neural Information Processing Systems (NeurIPS)*. 2015.

Eric Jang, Shixiang Gu, and Ben Poole. Categorical reparameterization with gumbel-softmax. In *Proc. of the International Conf. on Learning Representations (ICLR)*, 2017.

Jindong Jiang and Sungjin Ahn. Generative neurosymbolic machines. In H. Larochelle, M. Ranzato, R. Hadsell, M. F. Balcan, and H. Lin, editors, *Advances in Neural Information Processing Systems (NeurIPS)*, 2020.

Jindong Jiang, Sepehr Janghorbani, Gerard De Melo, and Sungjin Ahn. Scalor: Generative world models with scalable object representations. In *Proc. of the International Conf. on Learning Representations (ICLR)*, 2020.

Scott P Johnson. Object perception. In *Oxford Research Encyclopedia of Psychology*. Oxford University Press, 2018.

Diederik P. Kingma and Jimmy Ba. Adam: A method for stochastic optimization. In *Proc. of the International Conf. on Learning Representations (ICLR)*, 2015.

Diederik P Kingma and Max Welling. Auto-encoding variational bayes. In *Proc. of the International Conf. on Learning Representations (ICLR)*, 2014.

Thomas Kipf, Elise van der Pol, and Max Welling. Contrastive learning of structured world models. In *Proc. of the International Conf. on Learning Representations (ICLR)*, 2020.

Adam Kosiorek, Hyunjik Kim, Yee Whye Teh, and Ingmar Posner. Sequential attend, infer, repeat: Generative modelling of moving objects. In *Advances in Neural Information Processing Systems (NeurIPS)*, 2018.

J. v. Kügelgen, I. Ustyuzhaninov, P. Gehler, M. Bethge, and B. Schölkopf. Towards causal generative scene models via competition of experts. In *ICLR 2020 Workshop "Causal Learning for Decision Making"*, 2020.

H. W. Kuhn. The hungarian method for the assignment problem. *Naval Research Logistics Quarterly*, 2(1-2):83–97, 1955.

Brenden M. Lake, Tomer D. Ullman, Joshua B. Tenenbaum, and Samuel J. Gershman. Building machines that learn and think like people. *Behavioral and Brain Sciences*, 40: e253, 2017. doi: 10.1017/S0140525X16001837.

Zhixuan Lin, Yi-Fu Wu, Skand Vishwanath Peri, Weihao Sun, Gautam Singh, Fei Deng, Jindong Jiang, and Sungjin Ahn. Space: Unsupervised object-oriented scene representation via spatial attention and decomposition. In *Proc. of the International Conf. on Learning Representations (ICLR)*, 2020.

Francesco Locatello, Dirk Weissenborn, Thomas Unterthiner, Aravindh Mahendran, Georg Heigold, Jakob Uszkoreit, Alexey Dosovitskiy, and Thomas Kipf. Object-centric learning with slot attention. In *Advances in Neural Information Processing Systems (NeurIPS)*, 2020.

Joe Marino, Yisong Yue, and Stephan Mandt. Iterative amortized inference. In *Proc. of the International Conf. on Machine learning (ICML)*, 2018.

David Marr. Vision: A computational investigation into the human representation and processing of visual information. *W. H. Freeman, San Francisco*, 1982.

Loic Matthey, Irina Higgins, Demis Hassabis, and Alexander Lerchner. dsprites: Disentanglement testing sprites dataset. https://github.com/deepmind/dsprites-dataset/, 2017.

A. Milan, L. Leal-Taixé, I. Reid, S. Roth, and K. Schindler. MOT16: A benchmark for multi-object tracking. *arXiv.org*, 1603.00831, 2016.

Volodymyr Mnih, Nicolas Heess, Alex Graves, and Koray Kavukcuoglu. Recurrent models of visual attention. In *Advances in Neural Information Processing Systems (NeurIPS)*, 2014.

Adam Paszke, Sam Gross, Francisco Massa, Adam Lerer, James Bradbury, Gregory Chanan, Trevor Killeen, Zeming Lin, Natalia Gimelshein, Luca Antiga, Alban Desmaison, Andreas Kopf, Edward Yang, Zachary DeVito, Martin Raison, Alykhan Tejani, Sasank Chilamkurthy, Benoit Steiner, Lu Fang, Junjie Bai, and Soumith Chintala. Pytorch: An imperative style, high-performance deep learning library. In *Advances in Neural Information Processing Systems (NeurIPS)*, 2019.

F. Pedregosa, G. Varoquaux, A. Gramfort, V. Michel, B. Thirion, O. Grisel, M. Blondel, P. Prettenhofer, R. Weiss, V. Dubourg, J. Vanderplas, A. Passos, D. Cournapeau, M. Brucher, M. Perrot, and E. Duchesnay. Scikit-learn: Machine learning in Python. *Journal of Machine Learning Research (JMLR)*, 12:2825–2830, 2011.

Olaf Ronneberger, Philipp Fischer, and Thomas Brox. U-net: Convolutional networks for biomedical image segmentation. In *Medical Image Computing and Computer-Assisted Intervention (MICCAI)*, 2015.

Elizabeth S. Spelke. Where perceiving ends and thinking begins: The apprehension of objects in infancy. *The Minnesota symposia on child psychology*, 20:197–234, 1988.

Elizabeth S. Spelke and Katherine D. Kinzler. Core knowledge. *Developmental Science*, 10 (1):89–96, 2007. doi: https://doi.org/10.1111/j.1467-7687.2007.00569.x.

Tomer D. Ullman, Elizabeth Spelke, Peter Battaglia, and Joshua B. Tenenbaum. Mind games: Game engines as an architecture for intuitive physics. *Trends in Cognitive Sciences*, 21(9):649–665, 2017. ISSN 1364-6613. doi: https://doi.org/10.1016/j.tics.2017.05.012.

Sjoerd van Steenkiste, Michael Chang, Klaus Greff, and Jürgen Schmidhuber. Relational neural expectation maximization: Unsupervised discovery of objects and their interactions. In *Proc. of the International Conf. on Learning Representations (ICLR)*, 2018.

Rishi Veerapaneni, John D. Co-Reyes, Michael Chang, Michael Janner, Chelsea Finn, Jiajun Wu, Joshua Tenenbaum, and Sergey Levine. Entity abstraction in visual model-based reinforcement learning. In *Proc. Conf. on Robot Learning (CoRL)*, 2020.

Paul Voigtlaender, Michael Krause, Aljosa Osep, Jonathon Luiten, Berin Balachandar Gnana Sekar, Andreas Geiger, and Bastian Leibe. Mots: Multi-object tracking and segmentation. In *Proc. IEEE Conf. on Computer Vision and Pattern Recognition (CVPR)*, 2019.

Nicholas Watters, Loic Matthey, Matko Bosnjak, Christopher P. Burgess, and Alexander Lerchner. COBRA: Data-efficient model-based RL through unsupervised object discovery and curiosity-driven exploration. *arXiv.org*, 1905.09275, 2019a.

Nicholas Watters, Loic Matthey, Christopher P. Burgess, and Alexander Lerchner. Spatial broadcast decoder: A simple architecture for learning disentangled representations in VAEs. *arXiv.org*, 1901.07017, 2019b.

Zhenjia Xu, Zhijian Liu, Chen Sun, Kevin Murphy, William T. Freeman, Joshua B. Tenenbaum, and Jiajun Wu. Unsupervised discovery of parts, structure, and dynamics. In *Proc. of the International Conf. on Learning Representations (ICLR)*, 2019.

Jinyang Yuan, Bin Li, and Xiangyang Xue. Generative modeling of infinite occluded objects for compositional scene representation. In *Proc. of the International Conf. on Machine learning (ICML)*, 2019.